The SPIDER CMB Polarimeter

Thesis by

Amy R. Trangsrud

In Partial Fulfillment of the Requirements

for the Degree of

Doctor of Philosophy

California Institute of Technology

Pasadena, California

2012

(Defended July 26, 2011)

Acknowledgements

My journey here began one September day, walking into Andrew Lange's office in the basement of West Bridge, excited and nervous. In a moment he saw me, took me in, welcomed me, and set me at ease. Then we were off like a whirlwind. We walked briskly over to the high bay, where BICEP was nearing deployment. Andrew sent me up on a ladder to take in the technology, while he told me about B-modes, SPIDER, and BICEP2, his eyes alight with excitement. He oozed curiosity, ingenuity, and enthusiasm. Back in Bridge, he toured me through the White Dewar lab, where Chao-Lin Kuo was beam mapping. I remember Andrew saying, this could be you in a couple years. Sure enough, it was.

Andrew was exceptional in his ability to advise, understand, and nurture his students. When I sat down with him, he would immediately focus in on my situation and perspective, and on how he could best aid me in moving forward. He saw things in context, and gave science a sense of humanity. Andrew understood that the relationship between a PhD student and an advisor is a special one; one that plants a seed that shapes the student over a lifetime. So it will be for me. I am grateful and honored that Andrew shared his spirit with me, and I will carry and treasure his mentorship and example. Thank you Andrew.

When we lost Andrew, our Obscos team grew even stronger as a family. Kathy Deniston, Sunil Golwala, and Jamie Bock, while handling their own grief, opened their wings like protective parents, and swept everyone under. They were heros in a dark time. Simply put, we would not have a group without Kathy. She and Barbara Wertz are simultaneously the glue that holds everything together and the grease that keeps everything moving. To this day, I am not sure how Kathy does it all.

Sunil selflessly and apparently without hesitation took me, and others, under his advisorship when we were orphaned midstride. He has been an important part of my education from the beginning of my work here. Sunil affected me most notably with his willingness to spontaneously sit down to teach us something, and with his ability to explain physical

concepts clearly and to derive relevant results on a moment's notice.

There is no one in this group with whom I have worked as closely and over as many years as Jamie. SPIDER is made compelling by its detector technology more than anything else. Jamie is the core of the detector development effort, and therefore at the root of everything that we do. After four years of Thursday detector meetings, I sincerely hope that a bit of Jamie's deep understanding and intuition have rubbed off on me. I appreciate all that I have learned from him not only about the devices themselves, but about the process of developing new technology, patiently, methodically, and creatively.

I have had a number of mentors over my years here, and I appreciate each and every one of them for mentoring me, and showing me their style of science. Matt Kenyon at JPL showed me how to fly by the seat of my pants and get a lot done. Bill Jones had a way of making any task feel fun and valuable. Chao-Lin Kuo showed me how to manage experiments from start to end, and operate my own cryogenic test bed. Jeff Filippini and Marc Runyan mentored me in receiver characterization, and provided opportunities for me to take important roles in our team. There are many others. I would like to thank all of my colleagues and collaborators here at Caltech/JPL, and around the world.

Caltech is a community, and my memories of this place will extend well beyond the walls of the astronomy building. While enrolled here I met the love of my life, was sexually harassed by a janitor, was awarded a fellowship, had a life-changing surgery, lost my advisor, and got married. My friends have been with me through it all, and made this journey possible. You all know who you are. Thank you!

There is no easy way to put into words the debt I owe to my Mom and Dad for their love, support, sacrifices, patience and just plain hard work in helping me to grow into the person that I am, and in filling my life with an incredible abundance of opportunities.

It takes a special person to love and marry an academic. Especially a mad scientist, and, worst of all, an experimentalist. Lorelei has stood by my side through all my work here. She has driven with me to campus late at night and on weekends for cryogen fills, and sent me off at the airport as I embarked on a month-long deployment to the South Pole. She has patiently supported me and been my cheerleader as, every six months or so, I have told her about some change in my deployment schedule or planned graduation timeline. Most of all, she has been my partner in life and love.

The SPIDER Collaboration

California Institute of Technology J. P. Filippini, S. Golwala, V. V. Hristov, P. V. Mason, T. A. Morford, M. C. Runyan, M. A. Schenker, A. R. Trangsrud, R. S. Tucker

Cardiff University P. A. R. Ade, C. Tucker

Case Western Reserve University R. Bihary, S. Bryan, T. E. Montroy, J. E. Ruhl

Imperial College C. N. Clark, C. R. Contaldi, D. T. O'Dea

JPL J. J. Bock, J. A. Bonetti, B. P. Crill, O. Doré, W. Holmes, A. D. Turner

Kavli Institute for Cosmology, University of Cambridge C. J. MacTavish

NIST G. Hilton, K. Irwin, C. Reintsema

Princeton University H. C. Chiang, A. A. Fraisse, J. E. Gudmundsson, W. C. Jones, A. S. Rahlin

Stanford University C. L. Kuo

University of Toronto S. J. Benton, M. Farhang, L. M. Fissel, N. N. Gandilo, C. B. Netterfield, J. D. Soler, J. A. Shariff, J. R. Bond

University of British Columbia M. Amiri, B. Burger, G. Davis, M. Halpern, M. Hasselfield, D. Wiebe

Abstract

SPIDER is a balloon-borne millimeter-wave telescope designed to study the polarization of the Cosmic Microwave Background (CMB). SPIDER will map 10% of the full sky with degree-scale beams to search for the distinctive inflationary gravitational wave signal on angular scales between 1° and 10°, thereby probing the energy scale of inflation. In its first flight, SPIDER will field 2,400 antenna-coupled bolometers split between two bands centered at 93 and 148 GHz. Slot antenna arrays, band-defining microstrip filters, and superconducting bolometers are all fabricated photolithographically on a shared silicon substrate. SPIDER's detectors are split amongst six monochromatic on-axis refractors in a shared helium-cooled cryostat. This thesis reviews the design of SPIDER and its antenna-coupled bolometers, and details the currently achieved performance of SPIDER's receivers.

Contents

Acknowledgements **iii**

The SPIDER Collaboration **v**

Abstract **vi**

1 Introduction **1**

1.1 The Beginning of Physical Cosmology 1

1.2 Discovery of the Cosmic Microwave Background 4

1.3 CMB Statistics 5

1.4 Inflation Theory 9

1.5 CMB Temperature Anisotropies 12

1.6 CMB Polarizing Mechanisms 13

1.7 Polarized Foregrounds 19

2 The SPIDER Balloon-Borne CMB Polarization Experiment **22**

2.1 Collaboration 23

2.2 Frequency Coverage 23

2.3 Sky Coverage 26

2.4 Ballooning 26

2.5 Cryogenics 30

2.6 Optics 33

2.7 Half-Wave Plates 37

2.8 Magnetic Shielding 39

2.9 Simulations 40

3 Detectors and Readout **42**

3.1 Bolometric Technology Development 42

3.2 SPIDER Detector Architecture 45

3.3 Fabrication Process 49

3.4 TES Bolometer Basics 52

3.5 Readout 58

4 Receiver Performance **61**

4.1 Beam Profiles 61

4.2 Frequency Band Definition 71

4.3 Polarization Efficiency 79

4.4 Efficiency of Optical Response 80

4.5 Internal Optical Loading of Devices 86

4.6 Bolometer Properties 90

4.7 Noise Performance 94

4.8 Temperature Stability 100

4.9 Magnetic Field Response 101

4.10 Summary and Recommendations for Future Work 102

A Definitions and Methods **107**

A.1 Optical Efficiency 107

A.2 Alternative Methods for Calculating Internal Loading 109

B Measured Detector Parameters **112**

Bibliography **124**

List of Figures

1.1 Example of a CMB temperature and polarization map (from B2K) 7
1.2 Illustration of E- and B-mode polarization patterns 8
1.3 Definition of coordinate system for Thomson scattering calculation 14
1.4 Measurements to date of EE and BB power spectra 21
2.1 SPIDER bands and atmospheric emission model 25
2.2 The SPIDER observing region 26
2.3 The SPIDER gondola (drawings and photos) 29
2.4 The SPIDER flight cryostat (photo and cross-sectional drawing) 31
2.5 An assembled focal plane unit and a ^{3}He adsorption fridge (photos) 32
2.6 Modular telescope insert bays in the flight cryostat (photos) 34
2.7 A telescope insert (photo and cross-sectional drawing) 34
2.8 A half-wave plate assembly (photos) 37
2.9 Diagram showing rotation of polarization by a half-wave plate 38
2.10 Sensitivity of SPIDER bands to polarized dust 41
3.1 A spider-web bolometer and a polarization sensitive bolometer (photos) . . . 43
3.2 New technologies have enabled a large increase in detector counts 44
3.3 A SPIDER detector plate and a single pixel with components labeled (photos) 45
3.4 A portion of a slot antenna array (SEM micrograph) 47
3.5 An LC microstrip filter (SEM micrograph) 47
3.6 Silicon nitride legs thermally isolate each bolometer island (optical micrograph) 48
3.7 A bolometer island with substructures labeled (optical micrograph) 48
3.8 I-V curve showing both the Ti TES and Al TES transitions 48
3.9 A T-junction in an antenna microstrip summing tree (SEM micrograph) . . . 51
3.10 Cross-sectional schematic of the layered construction of the dual-TES 51
3.11 TES thermal diagram and electrical circuit 54

3.12 I-V, R-V and P-V curves, and method to measure leg thermal conductance . 56
3.13 A comparison of TES and NTD Ge thermistor response functions 57
4.1 Far field beam slices (linear and log scale) 63
4.2 Far field beam differences for a single pixel A/B polarization pair 64
4.3 Near field beam maps showing the effects of beam steer 66
4.4 Antenna far field beam maps (no telescope) for an A/B polarization pair . . 69
4.5 Primary antenna sidelobes (terminated inside telescope) 70
4.6 Beam maps showing uniform vs Gaussian-tapered feed 71
4.7 Measured flightlike 148 GHz passband and old-style 145 GHz passband . . . 73
4.8 Histogram and map of measured band centers on a 148 GHz tile 74
4.9 Spectra and differenced spectra for 148 GHz A/B polarization pairs 75
4.10 Convolution of the atmospheric model with the measured 148 GHz passband 76
4.11 Spectral model for 93 GHz band 77
4.12 Convolution of the atmospheric model with the 93 GHz passband model . . . 78
4.13 Measurement of cross-polarization response 80
4.14 The cold load cryostat (photos) 81
4.15 Setup for White Dewar single pixel optical efficiency measurement (photos) . 82
4.16 Histogram of measured signal attenuation by microstrip summing tree 84
4.17 Basic method for measuring internal loading 87
4.18 Measured internal loading is strongly correlated with measured sky response 88
4.19 R-V curves illustrating the impact of shared TES bias 92
4.20 Example of measured noise power spectral density 95
4.21 Measured noise depends on TES bias point 96
4.22 Example of measured noise equivalent current, power, and temperature . . . 97
4.23 Rough estimator for noise penalty due to shared TES bias 98
4.24 Comparison of dark and active devices showing the addition of photon noise 99
A.1 Optical response measurements are used to normalize device spectra 108
A.2 Alternative method for improved measurement of internal loading 110
B.1 Convention for designating tile rows and columns, and polarizations A and B 112

List of Tables

2.1 Responsibilities of SPIDER collaborating institutions 23

2.2 Planned frequency distribution of focal plane units for first and second flights 24

4.1 Model of loss mechanisms for the 148 GHz band 83

4.2 Projected optical loading on a single-polarization 148 GHz device 89

4.3 Measured uniformity of fabricated device parameters 93

4.4 Summary of measured receiver performance for the 148 GHz band 103

Chapter 1

Introduction

Today we are able to make precise statements about the age, composition and evolution of the universe, though the field of physical cosmology was born only a century ago (§1.1). In 1965, the discovery of the Cosmic Microwave Background (CMB, §1.2), relic radiation from the early universe, identified a rich source of information that has enabled many advances in cosmology. The statistical properties of the CMB (§1.3) contain valuable clues about the makeup of the universe at the time of decoupling, only 400,000 years after the Big Bang. The standard model for the evolution of the universe includes a brief exponential inflation of space in the first fraction of a second after the Big Bang (§1.4). Measurements of the temperature anisotropies of the CMB support the inflationary paradigm and have tightly constrained many of the parameters of the standard model (§1.5). The CMB is polarized by several mechanisms (§1.6). Polarized galactic emission (§1.7) acts as a foreground to the CMB signal, distinguishable by its unique spectral signature. Gravitational waves predicted by inflationary theories generate a faint but distinctive CMB polarization pattern. A detection of this polarization signature would provide very strong evidence supporting the theory of inflation and probe the epoch of inflation itself.

1.1 The Beginning of Physical Cosmology

Throughout history people all over the world have asked questions and developed stories to frame their experiences. What is the universe made up of, and how did it come to be this way? For thousands of years, these questions were only answerable in the spheres of philosophy and religion.

Bringing Together Space and Time

Modern physical cosmology theory has its roots in Albert Einstein's general theory of relativity, first published in 1915. General relativity is a generalization of special relativity, folding the three dimensions of space and one dimension of time into a four-dimensional space-time. Gravity falls out of the theory as a natural geometrical consequence. Einstein's paradigm was elegant and testable, and carried cosmology into the realm of true science.

General relativity explained the discrepancy between previous calculations based on Newtonian gravity and the measured precession of the perihelion of Mercury. In 1919 Sir Arthur Eddington and his collaborators mapped stars positioned near the Sun during a total solar eclipse. General relativity predicts the bending of light due to the curvature of space time around massive objects (here, the Sun). The measured apparent locations of the stars were offset in accordance with the predictions of general relativity [41]. For the past century, general relatively has successfully stood up to increasingly precise measurements of its various predictions, including the gravitational redshift of light, gravitational lensing, and time dilation. For example, the Cassini project announced in 2003 that the frequency shift of radio signals sent between the spacecraft and Earth, due to the gravitational well of the Sun, agreed with the predictions of general relativity to 0.002% [15].

Seeing Beyond the Milky Way

In the early 1900s, women were not granted access to telescope time. Henrietta Leavitt [14], a graduate of the college that would become known as Radcliffe, was one of several bright women hired at Harvard as human "computers." These women were paid $10.50 per week to sort through photographic plates to count and catalog the brightness of stars. Leavitt studied Cepheid variable stars, young bright stars whose luminosity varies cyclically. She examined Cepheids in the Andromeda nebula (all at similar distance) and discovered a simple relationship between the stars' maximal brightnesses and periods [80]. Measuring the period of a Cepheid gives the luminosity of the star, which can be compared to the measured brightness to find the distance. Previously, astronomical distances had only been measured by biannual triangulation, which was limited by telescope angular resolution. Leavitt realized that Cepheids could be used as standard candles to measure much larger distances with better precision.

In the 1920s Edwin Hubble began using the Hooker telescope on Mount Wilson just north of Pasadena, California, then the biggest telescope in the world. Applying Leavitt's period-luminosity relationship to Cepheids that he observed in several spiral nebulae, he made the first demonstration of objects definitely outside of our galaxy [62]. His announcement to the American Astronomical Society on New Years Day in 1925 expanded the known universe beyond the Milky Way and ushered in a new era in cosmology.

In the early 1910s, Vesto Slipher examined the spectroscopic features of spiral galaxies [111]. He was surprised to find that the galaxies were moving at hundreds of kilometers per second relative to earth (about 25 times the average stellar velocity, he noted). Slipher's work demonstrated that spectroscopy was a valuable tool for measuring the large radial velocities of galaxies using the Doppler shift. Slipher reported the velocities of fifteen galaxies. All but three were receding.

Big Bang Controversy

In the early 1920s Alexander Friedmann showed that general relativity does not generically predict the static universe put forth by Einstein [46, 47]. In general, the curvature of the universe can be time dependent and the universe may expand or contract. Friedmann's equations and conclusions were independently derived by Georges Lemaître in the late 1920s [81, 82]. Lemaître described a homogenous universe of constant mass and increasing radius. This accounted for the observed preponderance of galaxies receding from our own.

In 1929, Hubble demonstrated a positive linear relation between the distance to nearby galaxies (measured using Cepheids) and their radial velocities (measured spectroscopically using redshift) [61]. The combination of this relation ("Hubble's law") with the Cosmological Principle (an assumption of homogeneity and isotropy on large scales) implies that the universe is expanding.

Assuming that the universe has been expanding monotonically and that it obeys energy conservation laws, it must have begun with a small hot singularity at the the beginning of time. In 1949 Fred Hoyle coined the phrase "Big Bang" in reference to this singularity [59]. Hoyle preferred a Steady State theory, which obeyed the Perfect Cosmological Principal (homogeneity and isotropy in both space *and* time). Steady State theorists believed that the universe had no beginning or end, and that a constant creation of matter and energy maintained the expanding universe in a steady state (not changing statistically over time).

The debate between Big Bang theory and Steady State theory was a central dialog in cosmology until the 1965 publication of the discovery of the Cosmic Microwave Background, relic radiation from the hot Big Bang.

1.2 Discovery of the Cosmic Microwave Background

In the moments after the Big Bang, the plasma that filled the universe was too hot for electrons and protons to bind together to form hydrogen. Free electrons were prevalent and frequently interacted with photons through Thomson scattering. The mean free path of photons was short enough that conditions could be approximated as those of thermodynamic equilibrium, so the radiation field had a blackbody spectrum [4]. The expansion of the universe has since continuously decreased both its temperature and its matter density. Approximately 400,000 years after the Big Bang, at redshift $z \approx 1100$, the matter and radiation temperature had cooled sufficiently to favor the formation of neutral hydrogen and helium atoms [99]. This era is (deceptively) named recombination. The density of free electrons quickly diminished. When the average time between photon scatterings became comparable to the age of the universe, the universe became suddenly very transparent to radiation. Radiation decoupled from matter. This primordal radiation, the Cosmic Microwave Background (CMB), has permeated space largely undisturbed since decoupling.

The CMB is now redshifted into the microwave band by the expansion of the universe. In 1948, Alpher and Herman predicted that the CMB would permeate the universe today with a blackbody spectrum at 5 K [5]. Unaware of this previous calculation, in 1964 at Princeton University Dicke and Peebles forecast a temperature of 10 K for the CMB, and their colleagues Roll and Wilkinson set out to find experimental evidence of its existence. Simultaneously at Bell Labs, Penzias and Wilson were studying atmospheric noise with a large horn reflector antenna used to communicate with the Telstar satellite. Measuring at a wavelength of 7.35 cm, they picked up 3.5 ± 1 K of excess radiation that was found to be isotropic, unpolarized, and free from seasonal variation within their limits. Unable to explain this signal, they thoroughly cleaned and tested their equipment. Penzias then came across the Peebles calculation and contacted Dicke. Penzias and Wilson had accidentally scooped the Princeton group of the experimental confirmation for their theoretical calculations, and they later received the Nobel Prize for their discovery. In 1965, Astro-

physical Journal Letters published, side-by-side, letters from the Princeton group [37] and the Bell Labs group [100]. The following year Roll and Wilkinson at Princeton, measuring at a wavelength of 3.2 cm, published flux results consistent with blackbody radiation at 3.0 ± 0.5 K [106].

The COBE satellite, launched in 1989, carried several experiments to study the CMB. The FIRAS experiment measured its spectrum over a broad frequency range. The data mapped out the curve of a black body with temperature 2.725 ± 0.002 K [92]. The COBE anisotropy experiment, called DMR, found the CMB to be greatly isotropic [113]. Temperature anisotropies are usually decomposed into spherical harmonics (§1.3). The dipole term is dominated by the Earth's motion relative to the Hubble Flow and is irrelevant to cosmological anisotropy considerations. The small size of the remaining observed temperature anisotropy ($\Delta T/T \approx 10^{-5}$) excluded models that claimed that the CMB had a galactic source or random distribution of sources. This was a solid confirmation of Big Bang theory to the exclusion of Steady State theories.

1.3 CMB Statistics

The statistical properties of the CMB are a fruitful testing ground for cosmological theories. I here review the standard mathematical framework for quantifying CMB temperature and polarization statistics. Throughout this section I follow Kamionkowski et al. [68].

The Stokes Parameters

Polarization is conventionally defined in terms of the Stokes parameters. A linearly (plane) polarized electromagnetic wave has an oscillating electric field at a fixed azimuthal angle to the direction of propagation. A wave with two perpendicular components of equal amplitude that are out of phase by 90° is called a circularly polarized wave. For a monochromatic wave propagating along the z-axis, linear polarization can be described by

$$\vec{E} = E_x \cos(\omega t - \theta_x)\hat{x} + E_y \cos(\omega t - \theta_y)\hat{y} \ . \tag{1.1}$$

Polarization is completely quantified using the Stokes parameters ($\langle\rangle$ denotes a time average):

$$I \equiv \langle |E_x|^2 + |E_y|^2 \rangle \ , \tag{1.2a}$$

$$Q \equiv \langle |E_x|^2 - |E_y|^2 \rangle \ , \tag{1.2b}$$

$$U \equiv 2\langle |E_x||E_y| \cos(\theta_x - \theta_y) \rangle \ , \text{ and} \tag{1.2c}$$

$$V \equiv 2\langle |E_x||E_y| \sin(\theta_x - \theta_y) \rangle \ . \tag{1.2d}$$

The Stokes parameters have units of power and are additive for an incoherent superposition of waves. The parameter I represents the intensity of the radiation and is positive definite. It is the most commonly observed parameter, and in this case is simply proportional to the temperature of the CMB. The other three parameters quantify the polarization state, with $Q = U = V = 0$ for unpolarized radiation. Stokes Q and U measure linear polarization along axes rotated 45° with respect to one another. The parameter V quantifies circular polarization, which is expected to be zero for the CMB because, by symmetry, Thomson scattering processes can never produce any net circular polarization.

The orthogonal modes of linear polarization given by Q and U are dependent on the defined orientations of the x- and y-axes. The orientations are defined by the International Astronomical Union (IAU) convention. Taking the definitions of Q and U from Equation 1.2 and rotating the x–y plane through an angle ϕ gives new values for Q and U:

$$Q' = Q\cos(2\phi) + U\sin(2\phi) \ , \text{ and} \tag{1.3a}$$

$$U' = -Q\sin(2\phi) + U\cos(2\phi) \ . \tag{1.3b}$$

It is easy to show that $Q'^2 + U'^2 = Q^2 + U^2$, so $Q^2 + U^2$ is invariant under axis rotation. We can define the amplitude and orientation of the polarization:

$$P \equiv \sqrt{Q^2 + U^2} \ , \text{ and} \tag{1.4a}$$

$$\alpha \equiv \frac{1}{2}\tan^{-1}\frac{U}{Q} \ . \tag{1.4b}$$

The angle α defines a constant orientation parallel to the electric field of the wave. The orientation α does not have a direction, but rather describes the plane in which the electric

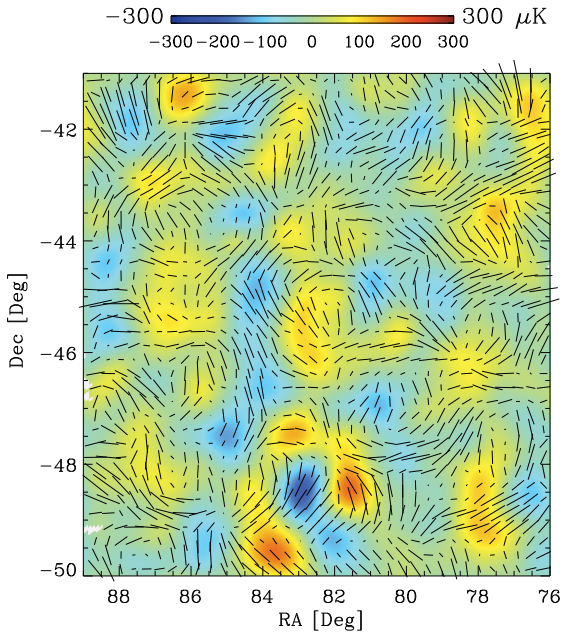

Figure 1.1: Example of a polarization and temperature map, from the B2K experiment [90].

field oscillates. Polarization maps are usually plotted as headless vectors with amplitude P and orientation angle α (see, for example, Figure 1.1).

The Harmonic Functions

The cosmological information encoded in the CMB is in the spatial correlations of the Stokes parameters. To quantify correlations in intensity at various angular scales, we decompose the temperature anisotropy scalar field into the spherical harmonics $Y_{lm}(\theta, \phi)$,

$$\frac{T(\theta,\phi)}{T_0} = 1 + \sum_{l=1}^{\infty} \sum_{m=-l}^{l} a_{lm}^T Y_{lm}(\theta,\phi). \tag{1.5}$$

Polarization is described by a 2×2 symmetric and trace-free tensor field. We construct it in spherical polar coordinates as

$$\mathcal{P}_{ab}(\theta,\phi) = \frac{1}{2} \begin{pmatrix} Q(\theta,\phi) & -U(\theta,\phi)\sin\theta \\ -U(\theta,\phi)\sin\theta & -Q(\theta,\phi)\sin^2\theta \end{pmatrix}. \tag{1.6}$$

The polarization tensor can be decomposed into an orthonormal basis of tensor harmonics,

$$\frac{\mathcal{P}_{ab}(\theta,\phi)}{T_0} = \sum_{l=2}^{\infty}\sum_{m=-l}^{l}\left[a^E_{lm}Y^E_{lm}(\theta,\phi) + a^B_{lm}Y^B_{lm}(\theta,\phi)\right], \tag{1.7}$$

where the coefficients are given by

$$a^E_{lm} = \frac{1}{T_0}\int\int \sin\phi d\theta d\phi\, \mathcal{P}_{ab}(\theta,\phi)\, Y^E_{lm}(\theta,\phi)^*, \text{ and} \tag{1.8a}$$

$$a^B_{lm} = \frac{1}{T_0}\int\int \sin\phi d\theta d\phi\, \mathcal{P}_{ab}(\theta,\phi)\, Y^B_{lm}(\theta,\phi)^*. \tag{1.8b}$$

The harmonics are

$$Y^E_{lm}(\theta,\phi) = \sqrt{\frac{2(l-2)!}{(l+2)!}}\begin{pmatrix} W_{lm}(\theta,\phi) & X_{lm}(\theta,\phi)\sin\theta \\ X_{lm}(\theta,\phi)\sin\theta & -W_{lm}(\theta,\phi)\sin^2\theta \end{pmatrix}, \text{ and} \tag{1.9a}$$

$$Y^B_{lm}(\theta,\phi) = \sqrt{\frac{2(l-2)!}{(l+2)!}}\begin{pmatrix} -X_{lm}(\theta,\phi) & W_{lm}(\theta,\phi)\sin\theta \\ W_{lm}(\theta,\phi)\sin\theta & X_{lm}(\theta,\phi)\sin^2\theta \end{pmatrix}, \tag{1.9b}$$

with

$$W_{lm}(\theta,\phi) = 2\left(\frac{\partial}{\partial\theta^2} - l(l-1)\right)Y_{lm}(\theta,\phi), \text{ and} \tag{1.10a}$$

$$X_{lm}(\theta,\phi) = \frac{2im}{\sin\theta}\left(\frac{\partial}{\partial\theta} - \cot\theta\right)Y_{lm}(\theta,\phi). \tag{1.10b}$$

The Y^E_{lm} and Y^B_{lm} tensor harmonics (Equations 1.9a,b) form a complete basis. Figure 1.2 shows examples of maps containing only Y^E_{lm} harmonics or only Y^B_{lm} harmonics. The Y^E_{lm} harmonics are called E-modes and the Y^B_{lm} harmonics are called B-modes, in analogy to curl-free electric (E) and divergence-free magnetic (B) fields.

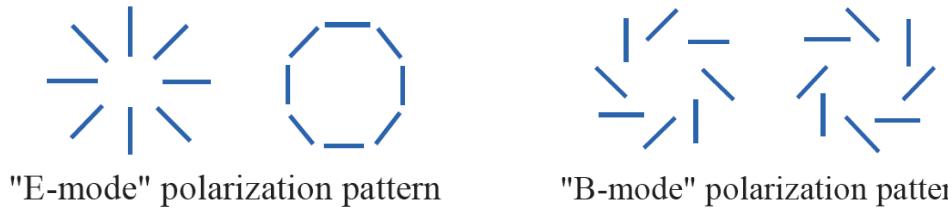

Figure 1.2: *Left*: Two examples of purely E-mode patterns. *Right*: Two examples of purely B-mode patterns.

Power Spectra

Assuming Gaussianity, the a^x_{lm} coefficients are independent normal random variables with zero mean and variance C^{xx}_l. The coefficients carry information only in their statistics, and we capture all of the relevant information in the power spectra (C^{xx}_l) and cross power spectra (C^{xy}_l) given by

$$\begin{aligned}
\text{Temperature :} \quad & \langle (a^T_{l'm'})^* (a^T_{lm}) \rangle &= \delta_{l',l}\delta_{m',m} C^{TT}_l, & \quad (1.11a)\\
\text{E-mode :} \quad & \langle (a^E_{l'm'})^* (a^E_{lm}) \rangle &= \delta_{l',l}\delta_{m',m} C^{EE}_l, & \quad (1.11b)\\
\text{B-mode :} \quad & \langle (a^B_{l'm'})^* (a^B_{lm}) \rangle &= \delta_{l',l}\delta_{m',m} C^{BB}_l, & \quad (1.11c)\\
\text{TE Cross:} \quad & \langle (a^T_{l'm'})^* (a^E_{lm}) \rangle &= \delta_{l',l}\delta_{m',m} C^{TE}_l, & \quad (1.11d)\\
\text{TB Cross:} \quad & \langle (a^T_{l'm'})^* (a^B_{lm}) \rangle &= \delta_{l',l}\delta_{m',m} C^{TB}_l, & \quad (1.11e)\\
\text{EB Cross:} \quad & \langle (a^E_{l'm'})^* (a^B_{lm}) \rangle &= \delta_{l',l}\delta_{m',m} C^{EB}_l, & \quad (1.11f)
\end{aligned}$$

where the angle brackets ($\langle\rangle$) denote an average over all realizations. Assuming isotropy, the power spectra are a function of l only (not of m).

The TT spectrum is the power in the temperature anisotropy, EE is the power in the E-mode polarization, TE is the correlation between temperature and E-mode polarization, and BB is the B-mode polarization. The remaining polarization spectrum combinations (TB, EB) have no expected cosmological signal.

1.4 Inflation Theory

Inflation theory came in to prominence in the early 1980s as an add-on to Big Bang theory. Alan Guth, the originator of inflation theory [54], wrote a very nice book [55] that includes an easy-to-read introduction to the theory entwined in a narrative describing its development. Detailed examination revealed that the details of Guth's original inflation model were problematic. In 1982 his model was replaced by a new inflation model due to Andrei Linde [86] and to Andreas Albrecht and Paul Steinhardt [3]. Linde wrote a technical book [87] systematically describing this theory and its place in cosmology and in particle physics. The open literature is rich with discussion of inflationary models, and inflation theory is included in all comprehensive modern cosmology textbooks (e.g., [122, 29]). Lid-

dle and Lyth have written a particularly helpful text [84]. Given the number of quality references available on inflation theory, I will only briefly summarize its key points here.

Inflation is commonly described as the slow roll of one or more scalar fields down a potential hill. The scalar field responsible for inflation is called the inflaton. Models with one scalar field are known as "single-field" and models that combine more than one scalar field are given the name "hybrid." During inflation, the energy density of the universe is dominated by the vacuum energy of the scalar field. This energy is associated with a negative pressure which, according to general relativity, produces a repulsive gravitational field that drives an exponential expansion of space. The particle horizon at any given time is the distance to the furthest point that light could have travelled from since the beginning of time. During inflation, space expands so quickly that regions of space that were once visible to each other are accelerated apart and out of each other's horizons.

The theoretically proposed inflationary epoch began around $t \approx 10^{-35}$ s and lasted only about 10^{-33} or 10^{-32} seconds before the scalar field settled into a stable potential well. The amount of inflation is typically quantified by the logarithmic growth of the scale factor, $N = \ln\left(a(t_{end})/a(t_{initial})\right)$. Resolving the horizon and flatness problems (described below) requires $N \gtrsim 60$, corresponding to a linear scaling factor of at least 10^{26} [20].

Motivations for Inflation Theory

Inflation is an essential element of the standard model of cosmology, and has developed and thrived over a couple of decades. In this section I justify our interest in pursuing experimental examination of inflation by explaining some of the motivations for the theory.

COBE revealed that the CMB is nearly perfectly isotropic over the whole sky. This isotropy on large angular scales poses a serious problem for cosmology. It implies that the radiation temperature was nearly uniform across the entire surface of last scattering. However, without inflation the horizon during the epoch of last scattering (at redshift $z_{ls} \simeq 1100$) subtends an angle of only about 1.6° on the sky today [122]. Why do we observe such strong homogeneity of causally disconnected regions? Inflation solves this problem, because it implies that the entire observable universe grew from a tiny volume of space that had sufficient time to thermalize before inflation.

Neglecting the cosmological constant because it has played a dominant role only in very

recent cosmological history, the Friedmann equations give

$$\left(\Omega^{-1}-1\right)\rho a^2 = \frac{-3kc^2}{8\pi G} \qquad \text{(a constant)}, \tag{1.12}$$

where Ω is the (time-dependent) ratio of the mean density to the critical density (ρ/ρ_c), a is the time-dependent expansion scale factor, and k is -1, 0, or $+1$ depending on the shape of the universe (closed, flat, or open). Following an otherwise standard model but excluding inflation, we can easily extrapolate the evolution of ρ and a through the radiation-dominated ($\rho \propto a^{-4}$) and matter-dominated ($\rho \propto a^{-3}$) periods back to early times. Doing so, we infer that ρa^2 would have decreased by about 10^{60} since the Planck era ($t_P \simeq G\hbar/c^5 \simeq 10^{-43}$ s) [29]. Therefore, in this inflationless model, $(\Omega(t_P)-1) \approx 10^{-60}(\Omega_0 - 1)$. Current constraints show that $|\Omega_0 - 1| \lesssim 0.01$ [73], implying that

$$|\Omega(t_P)-1| \lesssim 10^{-62} \qquad \text{(very small!)}. \tag{1.13}$$

This is considered a "fine tuning" problem. Without inflation there is no physical reason why the primordial density of the observable universe should have been so carefully tuned to the critical density or, equivalently, why the kinetic term of the expansion of the universe should be so carefully balanced with the gravitational term.

An epoch of inflation in the early universe alleviates this problem. During inflation, the scale factor a grows exponentially. Thus, regardless of any primordial deviation from the critical density, the length scales of the resulting curvature are much larger than the size of the observable universe. The observable universe should therefore appear to be almost exactly flat, as it does.

Typical Grand Unified Theories (GUTs) imply the existence of magnetic monopoles which formed at the symmetry breaking that occurred when the primordial universe cooled below the characteristic GUT energy scale. These heavy and stable monopoles are believed to have existed in great abundance. Without inflation, one would expect the current magnetic monopole relic abundance to be on the order of or greater than that of baryons [29]. This density has been very strongly excluded by experiment. In fact, at present there is no reproducible evidence for the existence of monopoles [23]. Inflationary cosmologies explain this apparent discrepancy because inflation, which occurred after the formation of

monopoles, would have very substantially diluted their concentration. This dilution effect also explains the lack of observational evidence for other predicted relics of a hot Big Bang, like gravitinos.

The greatest triumph of inflationary models is that they provide a causal source for the inhomogeneity of the universe and make distinct predictions about the formation of structure. Quantum fluctuations about the vacuum state produced small perturbations away from homogeneity in the early universe. Treating these fluctuations as small linear perturbations, 0th-order homogeneity implies that they can be simply broken down in to Fourier modes with no spatial dependence and no coupling between modes. The Fourier coefficients have a Gaussian probability distribution with zero average but nonzero variance in each mode [21]. Normally quantum fluctuations do not manifest macroscopically. However, during inflation space expanded so quickly that fluctuations were stretched to scales larger than the horizon scale and quantum fluctuations grew to become macroscopic real density perturbations. After inflation, the expansion of the universe slowed. As it did, modes began to reenter the horizon and to set the initial conditions for the formation of the large-scale structure that we see today in the universe.

The power spectrum of quantum fluctuations was scale invariant (exhibiting equal fluctuation power on all length scales). Classical exponential expansion during inflation preserves scale invariance. However, the transition out of the inflationary epoch would have caused the scalar spectral index (n_s) to deviate from unity (invariance). For slow roll models of inflation, the deviation would be small. This interesting prediction has been supported by WMAP which, combined with other cosmological data, measures $n_s = 0.968 \pm 0.012$ [73].

1.5 CMB Temperature Anisotropies

As density perturbations reentered the horizon after inflation, they began to undergo acoustic oscillations driven by competition between gravity and photon pressure. Oscillations occurred on all length scales within the horizon. Fourier modes with wavelengths exceeding the horizon scale did not oscillate because they were not causally connected.

When radiation decoupled from matter 400,000 years later, the radiation (now the CMB) carried away a snapshot of the density perturbations at the moment of decoupling. There is a great deal of cosmological information in the statistics of these perturbations. In fact,

isotropy and homogeneity assumptions imply that all of the cosmological information in the CMB is contained in the power spectra (defined in §1.3).

The temperature anisotropy power spectrum (C_l^{TT}) exhibits a series of peaks at the physical length scales associated with acoustic modes that were at amplitude maxima at the time of decoupling. The strongest peak in the power spectrum corresponds to the acoustic mode that had evolved through one quarter of an oscillation period into a state of maximal compression. This peak is found on degree scales, approximately the angular size of the horizon at decoupling. The next peak corresponds to the mode that had undergone three quarters of an oscillation. Between the peaks, troughs in the power spectrum are associated with acoustic modes at their velocity maxima.

In the late 1990s, TOCO [94] isolated the peak of the primary CMB anisotropy. At the turn of the century the first flight of the BOOMERANG balloon-borne telescope measured the first two peaks of the CMB temperature anisotropy power spectrum [78]. Quickly after, MAXIMA [104] mapped the first three peaks. The measured angular size of the primary anisotropy was consistent with that expected for cold dark matter models in a flat (Euclidean) universe [34].

Since the discovery of the CMB, many experiments have been fielded to tap the wealth of cosmological information it contains. Physical cosmologists are now able to evaluate theoretical models, constrain parameters, and make precise statements about the composition and history of the universe. Evidence from a variety of experiments supports a standard model of the universe called the ΛCDM model. The standard model is described in textbooks and throughout the open literature, so I will not summarize it here. The reader will note that experimental evidence is already sufficient to precisely constrain many of the parameters of the standard model to at least two significant digits (see, for example, [73]).

1.6 CMB Polarizing Mechanisms

Experiments are becoming increasingly sensitive to the polarization of the CMB, which contains unique cosmological information but is more than an order of magnitude weaker than the temperature anisotropy. The CMB is polarized by several mechanisms, which I summarize in this section. For further discussion I recommend the excellent review by Hu and White [60].

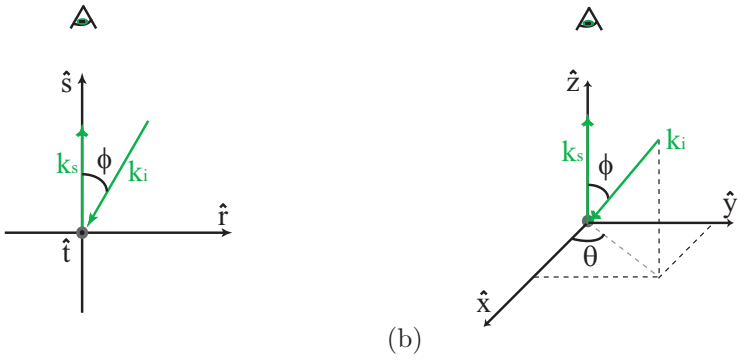

(a) (b)

Figure 1.3: *Left*: The scattering plane is a natural reference frame for a single scattering event. *Right*: A fixed reference frame. Radiation is incident on the scatterer from all directions (ϕ, θ).

Thomson Scattering of Quadrupole Moments

The CMB is polarized because Thomson scattering has a polarization dependent cross section. At a scattering site the wave vectors of the incident radiation ($\vec{k_i}$) and scattered radiation ($\vec{k_s}$) establish a natural frame of reference. In Figure 1.3a I define the scattering axis $\hat{s} \parallel \vec{k_s}$, the tangential axis $\hat{t} \perp \vec{k_i}, \vec{k_s}$, and the radial axis $\hat{r} \perp \hat{s}, \hat{t}$. The unpolarized incident beam can be modeled as the independent superposition of two linearly polarized beams of equal intensity. One is polarized along the tangential axis and the other in the plane of scattering.

$$\vec{E}_{i,1} \parallel \hat{t} \tag{1.14a}$$

$$\vec{E}_{i,2} \parallel \hat{r}\cos\phi + \hat{s}\sin\phi \tag{1.14b}$$

Each polarized incident beam forces the particle to oscillate and emit scattered radiation ($\vec{E}_{s,1}$ and $\vec{E}_{s,2}$). Applying the dipole approximation,

$$\vec{E}_{s,1} \propto \hat{s} \times \left(\hat{s} \times \left(\vec{E}_{i,1}\right)\right) \propto \hat{t}, \tag{1.15a}$$

$$\vec{E}_{s,2} \propto \hat{s} \times \left(\hat{s} \times \left(\vec{E}_{i,2}\right)\right) \propto \hat{r}\cos\phi. \tag{1.15b}$$

One scattered beam is linearly polarized in $\hat{t}$ and the other in $\hat{s}$. The power in each scattered beam is proportional to E^2, so

$$\left(\frac{dP}{d\Omega}\right)_r = \cos^2\phi \left(\frac{dP}{d\Omega}\right)_t . \tag{1.16}$$

Though the incident beam was completely unpolarized, the scattered beam is polarized along the tangential axis $\hat{t}$ with a polarization fraction

$$\Pi_t = \frac{1-\cos^2\phi}{1+\cos^2\phi}. \tag{1.17}$$

Let us now consider the more general case, where unpolarized radiation impinges on the scatter site from all directions with intensity $I(\phi,\theta)$, where ϕ and θ are defined by Figure 1.3b. In this new coordinate system,

$$\vec{E}_{i,1} \quad \| \quad \hat{x}\sin\theta + \hat{y}\cos\theta, \tag{1.18a}$$

$$\vec{E}_{i,2} \quad \| \quad \hat{x}\cos\theta\cos\phi + \hat{y}\sin\theta\cos\phi + \hat{z}\sin\phi, \tag{1.18b}$$

scatter in to

$$\vec{E}_{s,1} \quad \propto \quad \hat{z}\times\left(\hat{z}\times\left(\vec{E}_{i,1}\right)\right) \propto \hat{x}\sin\theta + \hat{y}\cos\theta, \tag{1.19a}$$

$$\vec{E}_{s,2} \quad \propto \quad \hat{z}\times\left(\hat{z}\times\left(\vec{E}_{i,2}\right)\right) \propto \hat{x}\cos\theta\cos\phi + \hat{y}\sin\theta\cos\phi. \tag{1.19b}$$

Adding the power ($P \propto E^2$) of these two beams and separating them into components polarized in $\hat{x}$ and $\hat{y}$ gives

$$\left(\frac{dP}{d\Omega}\right)_x \quad \propto \quad \int_0^{2\pi} d\theta \int_0^{\pi} \sin\phi \; d\phi \; I(\phi,\theta)\left(\sin^2\theta + \cos^2\theta\cos^2\phi\right), \tag{1.20a}$$

$$\left(\frac{dP}{d\Omega}\right)_y \quad \propto \quad \int_0^{2\pi} d\theta \int_0^{\pi} \sin\phi \; d\phi \; I(\phi,\theta)\left(\cos^2\theta + \sin^2\theta\cos^2\phi\right). \tag{1.20b}$$

The polarization fraction along the x-axis is

$$\Pi_x = \frac{\left(\frac{dP}{d\Omega}\right)_x - \left(\frac{dP}{d\Omega}\right)_y}{\left(\frac{dP}{d\Omega}\right)_x + \left(\frac{dP}{d\Omega}\right)_y} = \frac{\int_0^{2\pi} d\theta \int_0^{\pi} \sin\phi \; d\phi \; I(\phi,\theta)\left(\sin^2\theta - \cos^2\theta\right)\sin^2\phi}{\int_0^{2\pi} d\theta \int_0^{\pi} \sin\phi \; d\phi \; I(\phi,\theta)\left(1+\cos^2\phi\right)}. \tag{1.21}$$

As we expect given symmetry, $\Pi_x = 0$ for $I(\phi,\theta) = I(\phi)$.

Examining the spherical harmonics,

$$\begin{aligned} \text{When } \; I(\phi,\theta) &= I_0 Y_l^m(\phi,\theta), \\ \Pi_x &= 0 \quad \forall\ l \text{ except } l=2. \end{aligned} \tag{1.22}$$

Scalar (Y_2^0), vector ($Y_2^{\pm 1}$) and tensor ($Y_2^{\pm 2}$) quadrupoles polarize scattered radiation. Inflation models predict that both scalar and tensor perturbations were present when CMB photons last scattered at decoupling.

Scalar (Density) Perturbations at Decoupling

The density perturbations present in the early universe oscillated acoustically (§1.5). Bulk flows blueshifted radiation in the reference frame of scatterers. Blueshifting generated Y_2^0 (scalar) quadrupolar moments in incident power at scattering sites, slightly polarizing the scattered radiation. The expansion of the universe damps vorticity, so bulk flows occurred radially in and out of underdense and overdense regions. The axial symmetry of Y_2^0 harmonics implies that scattering of these modes produced a purely E-mode pattern with no B-modes. This mechanism is responsible for the dominant CMB polarization signal on angular scales smaller than 10° (with rms ~ 10 μK).

Because this polarizing mechanism is associated with the velocity component of the oscillations, the polarization power spectrum is 90° out of phase with the temperature power spectrum. Measurements of this signal provide an independent test of the standard model, break existing degeneracies and strengthen constraints on model parameters. In 2002 the Degree Angular Scale Interferometer (DASI) made the first detection of the polarization of the CMB [74]. The EE polarization power spectrum, measured in the range $300 \leq l \leq 450$, was consistent with theoretical predictions. BICEP [27] and QUAD [53] now provide the strongest measurements at degree and subdegree scales respectively (Figure 1.4).

Tensor (Gravitational Wave) Perturbations at Decoupling

Tensor perturbations generated by inflation are called inflationary gravitational waves. They are created at some level in all inflationary models. Just like scalar (density) perturbations, tensor perturbations on progressively larger physical length scales reenter the horizon as it expands after inflation. Once they do they begin to redshift and decay. Therefore, the

effect of inflationary gravitational waves on the CMB should be strongest on angular scales larger than the horizon size at the time of decoupling ($\sim 1^\circ$).

Gravitational waves created tensor quadrupole moments ($Y_2^{\pm 2}$) in the frame of scatterers at the time of decoupling by alternately stretching and compressing the wavelengths of photons propagating orthogonally to each other. Thomson scattering of this quadrupole generates both E- and B-mode polarization (in equal amount). Because scalar perturbations do not produce B-modes, B-mode polarization at large angular scales on the sky constitutes a unique signature of gravitational waves generated during inflation [67].

The relative amplitude of the gravitational wave signal is quantified by the tensor-to-scalar ratio r, which is given by [83]

$$r_l = \frac{C_{l(\mathrm{grav})}}{C_{l(\mathrm{density})}}, \tag{1.23}$$

where the $C_{l(\mathrm{grav})}$'s correspond to the gravitational wave polarization signal and the $C_{l(\mathrm{density})}$'s correspond to the CMB polarization generated by the dominant mechanism. The dependence of r_l on l is expected to be fairly weak, and a single value r is frequently defined using the ratio at the quadrupole ($l = 2$).

The tensor-to-scalar ratio r and the scalar spectral index n_s are directly related to parameters that describe the inflationary scalar potential [72]. A measurement of r would therefore not only confirm inflation theory, but would act to distinguish between different inflationary models and to probe the physics of the inflationary epoch [11].

As of this writing, the B-mode signal has not been detected. Currently, Keisler et al. [71] sets the best published constraint on r ($r < 0.17$ at 95% confidence). This comes from the combination of SPT and WMAP data with distance measurements from baryon acoustic oscillations and current constraints on the Hubble constant. This constraint comes mostly from measurements of the tensor contribution to CMB temperature anisotropies at large scales. BICEP places the strongest published constraint based on measurement of CMB polarization (Figure 1.4). They find $r < 0.73$ at 95% confidence [27].

Our current measurements of cosmological parameters provide some constraints on inflationary theories, but theories can still be constructed that produce a broad range of r values including values that are too small to ever be detectable. However, the simplest inflation models at GUT-scale energies forecast a tensor-to-scalar ratio that is large enough to be

detected with the next generation of CMB polarization experiments ($r > 0.01$, equivalent to 10s or 100s of nanoKelvin rms) [20].

Rescattering at Reionization

After recombination, hydrogen in the universe was largely neutral and thus transparent to radiation. Stars had not yet formed. For hundreds of millions of years radiation was neither emitted nor scattered at significant levels except at characteristic hydrogen absorption energies. This period is known as the cosmic "Dark Ages."

An expanding universe full of neutral hydrogen presents an opaque barrier to ultraviolet photons emitted with energies above 10.2 eV, the rest frame Lyman-α energy. Over time photons that start out with energies above 10.2 eV are redshifted down and then promptly absorbed. Even a very small residual of neutral hydrogen presents a formidable absorption barrier. The absence of the resulting Gunn-Peterson absorption trough in quasar spectra at redshift $z < 6$ is strong evidence that intergalactic hydrogen went through a period of reionization and is now almost entirely ionized. In 2001, two separate detections were made of $z > 6$ quasars demonstrating a Gunn-Peterson trough [38, 12]. This places the tail end of the reionization process around $z = 6$.

The Dark Ages were ended by the formation of luminous compact objects capable of emitting enough energy to ionize hydrogen on large scales. It is still uncertain what kinds of objects were the dominant source of this power. Leading theories favor Population III stars (never observed) as the primary catalysts for reionization [6, 8]. The details of this important transitional epoch are still poorly understood.

Since the universe reionized, some fraction of the CMB radiation has scattered off of the (now) free electrons. This rescattering produces several measurable effects. The most dramatic of these is a distinctive peak in the polarization power spectrum at angular scales larger than 10° generated by the Thomson scattering of the intrinsic local CMB temperature quadrupole incident on scattering sites at the time of reionization [69]. The amplitude of this peak is proportional to the square of τ, the optical depth to reionization. In a model with no reionization, the correlated CMB polarization signal at large angles would be negligible. WMAP has detected the reionization feature at 5.5σ with $\tau = 0.088 \pm 0.015$ [79]. In instantaneous reionization models this implies $z_{reion} = 11.0 \pm 1.4$. Interestingly, this rules out a simple sudden reionization at $z_{reion} \approx 6$, and suggests an extended period of partial

ionization. PLANCK's deep full sky polarization measurements will greatly improve our understanding of this important epoch.

Gravitational Lensing

Large concentrations of mass curve space time and act as lenses bending the paths of photons. Gravitational lensing of CMB E-mode polarization distorts the polarization pattern and produces a small signal on the sky that includes B-modes as well as E-modes [125]. This is expected to be the dominant source of B-mode signal at small angular scales, peaking around 10'. Experiments that probe deeply with high resolution (like SPTPOL [93]) will be best equipped to characterize the lensing B-mode signal. The power spectrum of the B-mode lensing spectrum depends on the matter power spectrum. Measurements of the lensing signal will be used to probe the matter distribution, the sum of the neutrino masses and the dark energy equation of state [36, 112].

1.7 Polarized Foregrounds

Polarized galactic foreground emission dominates over the CMB B-mode signal on average over the full sky [40, 119]. At microwave frequencies synchrotron radiation, dust emission and free-free emission (bremsstrahlung) are the relevant diffuse foregrounds [40]. Dust is dominant above around 90 GHz and synchrotron dominates at lower frequencies. Free-free emission is subdominant to dust and synchrotron at all frequencies. The Earth's atmosphere is expected to exhibit negligible linear polarized emission from a balloon-based observing platform [57].

Dust in the interstellar medium of our galaxy emits blackbody radiation modified by a frequency-dependent emissivity. Dust grains (carbonaceous material and silicate minerals) are not spherical and preferentially align themselves with the galactic magnetic field. This alignment causes their emission to be polarized [44, 39]. Polarized dust emission was first measured by ARCHEOPS [13], which found a polarization fraction of 4%–5% across much of the galaxy with some regions exhibiting polarization fractions as high as 10%–20%. Polarized dust has not been sensitively mapped across the full sky and the parameters of polarized dust emission are not yet well constrained, especially away from the galactic plane. PLANCK will produce sensitive full sky maps of dust emission. FDS Model 8 [43]

assumes two dust components and fits four parameters. It is used in simulations by most CMB experimental groups, including SPIDER.

Electrons moving through the galaxy are accelerated in a circular motion perpendicular to the galactic magnetic field. As they spiral in a helical motion along field lines they emit synchrotron radiation [109]. The spectrum of synchrotron emission can be approximated by a power law with a negative exponent, $I_\nu \propto \nu^{-s}$. Averaging over the elliptically polarized emission from individual electrons, bulk synchrotron emission can be highly linearly polarized in the direction orthogonal to the magnetic field. WMAP has produced robust full sky maps of synchrotron emission on angular scales of $>1^\circ$ [49, 58, 97].

When electrons scatter off of each other and ionized nuclei in the interstellar medium they emit free-free radiation [109]. The spectrum of free-free radiation follows a well-defined power law and correlates with H-α emission. Because electron scattering directions are random, free-free emission is intrinsically unpolarized. However, radiation emitted through free-free emission may then become polarized (at a level of no more than 10%) through Thomson scattering with electrons on the edges of Galactic H II regions [70].

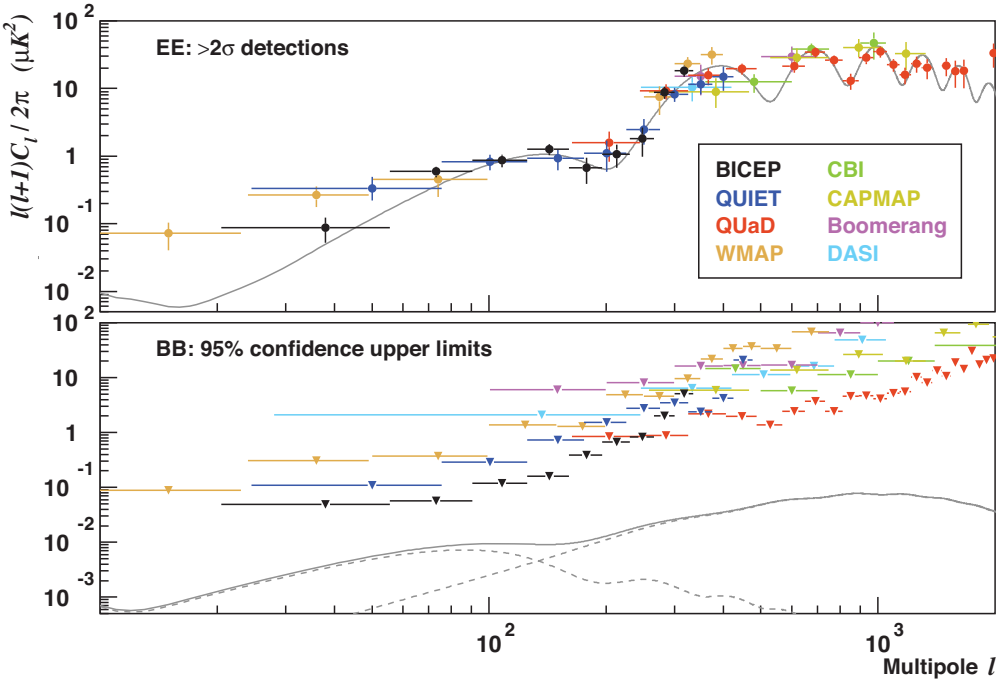

Figure 1.4: Currently published EE and BB power spectra measurements. Theoretical spectra from the standard model (ΛCDM) are shown for comparison. BB polarization has not been measured; upper limits are shown. The theoretical BB power spectrum (solid line) is the sum of the inflationary and gravitational lensing components (dashed lines). The lensing component dominates at small angular scales (large l). The amplitude of the theoretical inflationary BB component is not known. It is plotted here for a tensor-to-scalar ratio $r = 0.1$. Figure credit: H. C. Chiang.

Chapter 2

The SPIDER Balloon-Borne CMB Polarization Experiment

The SPIDER CMB polarization experiment [32, 42, 45] is specifically designed to search for the CMB inflationary gravitational wave B-mode signal. Because this signal is expected to be faint in comparison with polarized galactic foregrounds, SPIDER will observe the microwave sky in three frequency bands to discriminate between the CMB and galactic foregrounds based on their distinct spectral signatures (§2.2). SPIDER will target a field not heavily contaminated by galactic dust, mapping a large region in the southern sky (§2.3). Observing 9.5% of the full sky with $\sim 1^\circ$ beams maximizes SPIDER's sensitivity to angular scales between 1° and 10°. These moderate angular scales correspond to the multipoles $10 < l < 100$ where the inflationary B-mode signal peaks. To minimize response to atmospheric fluctuations and reduce photon noise and loading, SPIDER will observe from a long duration balloon in the relatively stable low background environment above the troposphere (§2.4).

To mitigate risk the designs of SPIDER's optical, cryogenic, magnetic shielding, and attitude systems (§2.4–§2.6) favor simplicity and the use of proven technologies where possible. The attitude control system is based on the configuration flown successfully on BOOMERANG and more recently on BLAST and BLAST-POL. SPIDER's compact telecentric optics are based on the successful optical design of BICEP and BICEP2. Importantly, a cold half-wave plate system (§2.7) has been developed and added just skyward of the objective lens to control systematic beam effects. Extensive magnetic shielding (§2.8) was also added to address systematic effects arising from the coupling of the SQUID multiplexing system to Earth's magnetic field. Systematic effects are modeled and quantified using a simulation pipeline (§2.9).

Institution	Institution Lead	Principal Responsibilities
Princeton	William Jones*	Cryogenics and system integration
Caltech and JPL	James Bock	Receiver fabrication and testing
U. Toronto	C. Barth Netterfield	Gondola and flight systems
Case Western	John Ruhl	Stepped cryogenic half-wave plates
NIST	Kent Irwin	SQUID multiplexing readout system
U. British Columbia	Mark Halpern	Warm readout electronics
Cambridge	Carrie MacTavish	Simulations
Cardiff	Peter Ade	Filters

Table 2.1: SPIDER collaborating institutions. William (Bill) Jones is the Principal Investigator. Andrew Lange was the proposing Principal Investigator, and led the team until his death in 2010.

2.1 Collaboration

The SPIDER collaboration is composed of expert institutions in each of the major component subsystems (Table 2.1). Many of the senior members were leading participants in the very successful BOOMERANG collaboration [89, 90, 31]. Locally, Caltech is responsible for receiver design, detector characterization, optics, and magnetic shielding. NASA JPL fabricates the antenna-coupled TES detectors and integrates them into focal planes. My primary responsibilities have been in detector development with Jamie Bock and the JPL detector fabrication team, and in the characterization of SPIDER's overall receiver performance with other Caltech collaborators.

2.2 Frequency Coverage

On large angular scales the B-mode CMB polarization signal is faint in comparison with the polarized galactic foregrounds due to synchrotron and thermal dust emission [40, 119]. Confusion with polarized astronomical foregrounds sets the ultimate limit on measurements of CMB polarization on large scales. Accurate modeling and mapping of foreground signals is therefore crucial to isolating the CMB polarization signal. Because synchrotron emission, dust emission, and the CMB each have unique spectral signatures, mapping the microwave sky at multiple frequencies enables foreground mapping and subtraction.

Synchrotron emission is dominant below around 90 GHz and increases at lower frequencies. WMAP employs multiple bands below 100 GHz and has very effectively mapped synchrotron emission across the full sky [49]. Data from experiments like QUIET [103] and

Flight	Focal Plane Frequency Distribution
SPIDER 1, December 2012	3 × 93 GHz; 3 × 148 GHz
SPIDER 2, December 2014	2 × 93 GHz; 2 × 148 GHz; 2 × 280 GHz

Table 2.2: Planned frequency distribution of focal plane units and timeline for SPIDER's first and second flights. SPIDER is a modular instrument with bays for six independent monochromatic telescopes.

PLANCK LFI will map synchrotron emission with increasing sensitivity in coming years.

Polarized thermal dust emission becomes dominant above around 90 GHz and increases with frequency. However, its properties are not well constrained by the published literature, especially off of the galactic plane. PLANCK HFI has been observing for more than a year with bands at 100, 143, 217, 353, 545, and 857 GHz [77]. PLANCK's recent release of full sky images of the galaxy in all six HFI bands emphasizes the ability of this data set to characterize the spectral energy density of the dust emission intensity [101]. In 2012 PLANCK will release calibrated time-ordered data, full sky maps at each frequency, full sky component maps (CMB and galactic foreground emission), and a final compact source catalog.

SPIDER will map the off-galaxy southern sky with bands centered at 93, 148, and ∼280 GHz, each with a ∼25% bandwidth. The planned frequency distribution of focal plane units for each flight is tabulated in Table 2.2. In its first flight, SPIDER will map the sky in the prime 93 and 148 GHz bands where the CMB signal is the strongest. Based on our foreground model, we expect to begin to detect polarized dust emission in the 148 GHz band in the first flight. The ∼280 GHz band (not yet designed or fabricated) will be added in the second flight to provide greater leverage for discriminating, mapping and subtracting polarized interstellar dust emission. This band will also complement the PLANCK data set by filling in the gap in its frequency coverage.

SPIDER's bands are selected to fall within natural gaps in atmospheric and galactic line emission. Atmospheric emission is plotted in Figure 2.1. Also plotted are the locations of galactic CO emission lines.

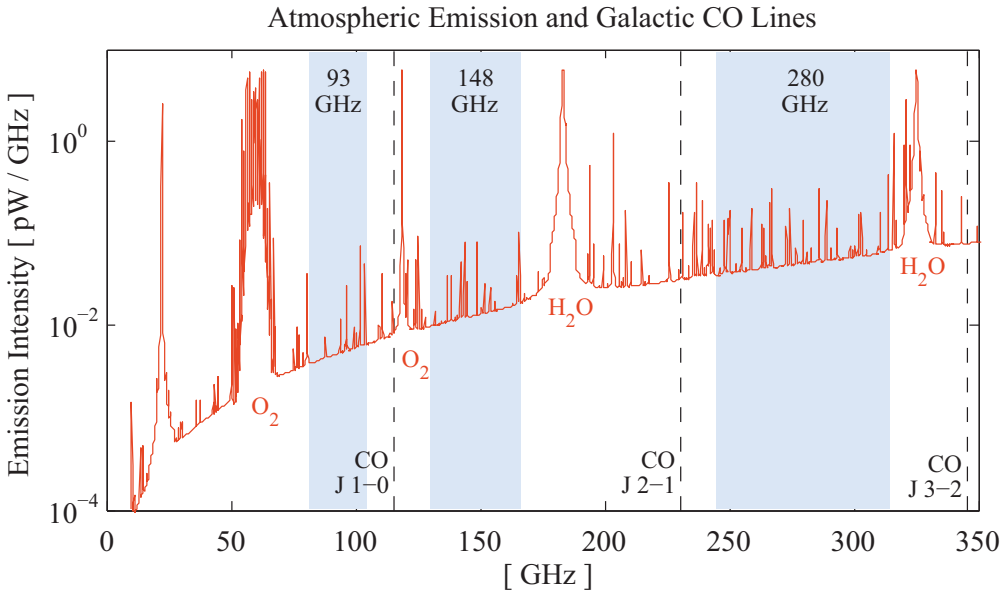

Figure 2.1: SPIDER will observe in bands centered at 93, 148, and ∼280 GHz to minimize response to atmospheric emission lines and to galactic CO emission lines.
Red: The power density [pW/GHz] of atmospheric emission based on a model for mid-latitude emission at 30 km altitude [98]. *Black dashed*: The frequencies associated with rotational transitions of galactic $^{12}C^{16}O$ [30]. CO emission intensity should vary significantly across the sky, and is expected to decrease at higher galactic latitudes.

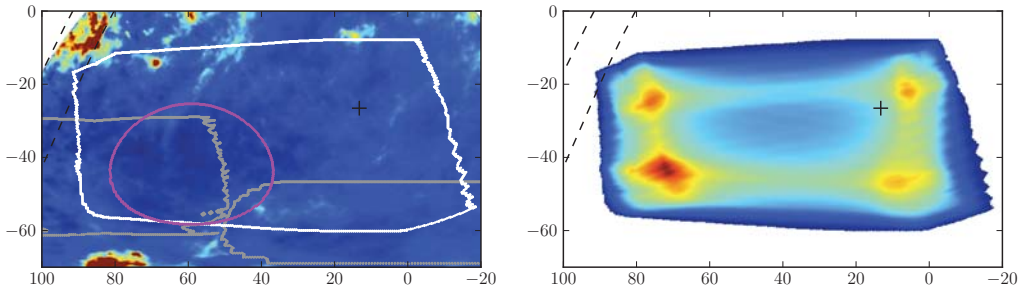

Figure 2.2: *Left*: Polarized dust amplitude at 150 GHz, according to the model in [95] (0–5 μK_{CMB}, linear scale). The SPIDER observing region (outlined in white) covers most of the southern sky not heavily contaminated by dust. The southern Galactic pole (black +) is overplotted, along with the 10- and 20-degree galactic latitude lines (dashed). Also shown are the BICEP and BOOMERANG fields (gray outlines), and the region of minimum foreground contamination in the SPIDER field (purple outline). *Right*: Distribution of integration time (linear scale), averaged over all detectors in a single 148 GHz focal plane for the observing strategy discussed in §2.4. This observing profile covers 10% of the sky, of which 85% is observed with near-isotropic coverage in crossing angles. Figure from [45].

2.3 Sky Coverage

SPIDER will map most of the southern sky not heavily contaminated by galactic dust, for a total of 10% of the full sky (Figure 2.2). With subdegree beam sizes (30' at 148 GHz), SPIDER is most sensitive to correlations on angular scales between 1° and 10°. These scales correspond to spherical harmonics with multipole moments $10 < l < 100$.

SPIDER's sky coverage is more expansive than that of experiments such as SPTPOL, which will target larger multipoles with its smaller beams and provide strong sensitivity to the gravitational lensing signal. PLANCK will map the full sky and therefore achieve sensitivity to the lowest monopoles ($2 < l < 10$). PLANCK is in a unique position to measure the reionization peak in the polarization power spectra at $l < 10$. In fact, all of PLANCK's sensitivity to the inflationary B-mode signal is in the reionization peak at very large angular scales. The SPIDER and PLANCK data sets will provide very complementary probes of the inflationary gravitational wave signal.

2.4 Ballooning

Dielectrics polarize in a static electromagnetic field. In an oscillating electromagnetic field, polar molecules are torqued in oscillation, generating power that is dissipated as heat. Out-

side of the scientific community microwaves are best known for their use in heating food because the dielectric H_2O, common in foods, interacts efficiently with microwaves. Water vapor in the Earth's atmosphere emits a significant amount of energy in a continuum across the microwave bands of interest to CMB science. This atmospheric emission contributes both photon noise and loading. Because water vapor density is inhomogenous and temporally variable, it is particularly difficult to effectively subtract from measurements made over large angular scales. Atmospheric noise is also especially onerous in higher frequency bands (above 150 GHz), as the CMB intensity is dropping off with frequency while the atmospheric noise is increasing (Figure 2.1).

Most ($\sim$99%) of the water vapor in the Earth's atmosphere is in the troposphere, the lowest portion of the Earth's atmosphere. SPIDER will observe from above the troposphere at an altitude of $\sim$32 km on long duration balloon flights provided by NASA's Columbia Scientific Balloon Facility (CSBF). The balloon platform provides a relatively stable low background environment for observing. Each balloon flight will launch from McMurdo, Antarctica and will circle the continent for about 20 days guided by the polar vortex winds. At the completion of the flight, SPIDER will separate from the balloon and free fall toward the Earth. A parachute will open to slow the descent of the payload, which will then be recovered from the Antarctic ice fields and recommissioned for the next flight.

Ballooning puts a number of constraints on any experiment. These include power constraints, lack of physical access to the instrument during operation, limited in-flight communication bandwidth, and mass constraints. The specific technical requirements of ballooning and satellite missions are similar, making SPIDER is a particularly good pathfinder for the proposed Experimental Probe of Inflationary Cosmology (EPIC) orbital mission [16]. SPIDER will pioneer multiple technologies for the EPIC satellite, just as its predecessor BOOMERANG pioneered technologies for PLANCK.

SPIDER will be powered by solar arrays coupled with batteries. All instrument functions are designed to be commandable from the ground. In flight, SPIDER's communications bandwidth will be sufficient only to check flight systems and thermometry and to send operating commands. A very small fraction of the science data will be transmitted for verification purposes, so mission success requires recovery of the flight computers. Mass is perhaps the most challenging constraint set by the ballooning platform. SPIDER must keep the entire science payload under about 5,000 lb. Systems have been designed to minimize

weight and, where possible, materials have been chosen accordingly.

The University of Toronto is responsible for the SPIDER gondola, which is the mechanical structure that couples the SPIDER instrument to the balloon and scans the telescope. Traditionally gondolas for balloon-borne experiments are constructed from welded aluminum. For weight reduction, the SPIDER gondola frame is constructed from carbon fiber reinforced polymer tubes with aluminum joints. Both finite element analysis (FEA) and physical pull tests on individual components have demonstrated compliance with requirements for strength and stiffness. Stiffness requirements are driven by the need to maintain pointing accuracy as the system center of mass shifts due to cryogen boil off and ballast drops. The system is designed with adequate strength to accommodate a parachute deployment acceleration of up to 10 g. An impact attenuation system supplied by CSBF and attached to the bottom of the gondola controls the large forces on landing. The base of this system is large to reduce the probability of rolling. To protect the cryostat in the event of a rollover, the front of the gondola frame extends forward to a rollover bar.

SPIDER will utilize a reaction wheel to perform back and forth continuous antisun scans in azimuth with steps in elevation. An active pivot between the balloon flight train and the gondola compensates for balloon rotation. The motorized reaction wheel can spin the gondola with a $0.8^\circ/s^2$ maximum acceleration and $6.0^\circ/s$ maximum speed. The elevation drive is driven by two linear actuators and allows adjustment from 22° to 52°. The baseline scan strategy calls for elevation steps of 1° every hour, from 28° to 40° and then back again. The instrument completes an entire scan cycle in one day. The amplitude and center of each azimuth scan is selected at each elevation to remain in the low foreground off-galaxy southern sky and to avoid approaching within 90° of the sun.

SPIDER's pointing system is based on proven technologies and techniques. It includes two CCD star cameras, 3-axis gyroscopes, a differential GPS, sun-sensing photodiodes, and a 3-axis magnetometer. The gondola attitude is determined using absolute pointing measurements provided by star cameras. The two cameras are mounted on a platform that is rotated opposite the gondola, holding them relatively fixed on the sky. The relative orientations of the platform and cryostat are recorded using a precision optical encoder. In between star camera measurements, attitude is reconstructed based on integration of the 3-axis fiber optic rate gyroscopes. The star camera, gyroscope, GPS, and magnetometer systems have been tested in flight on BLAST-POL [117]. Based on this experience we

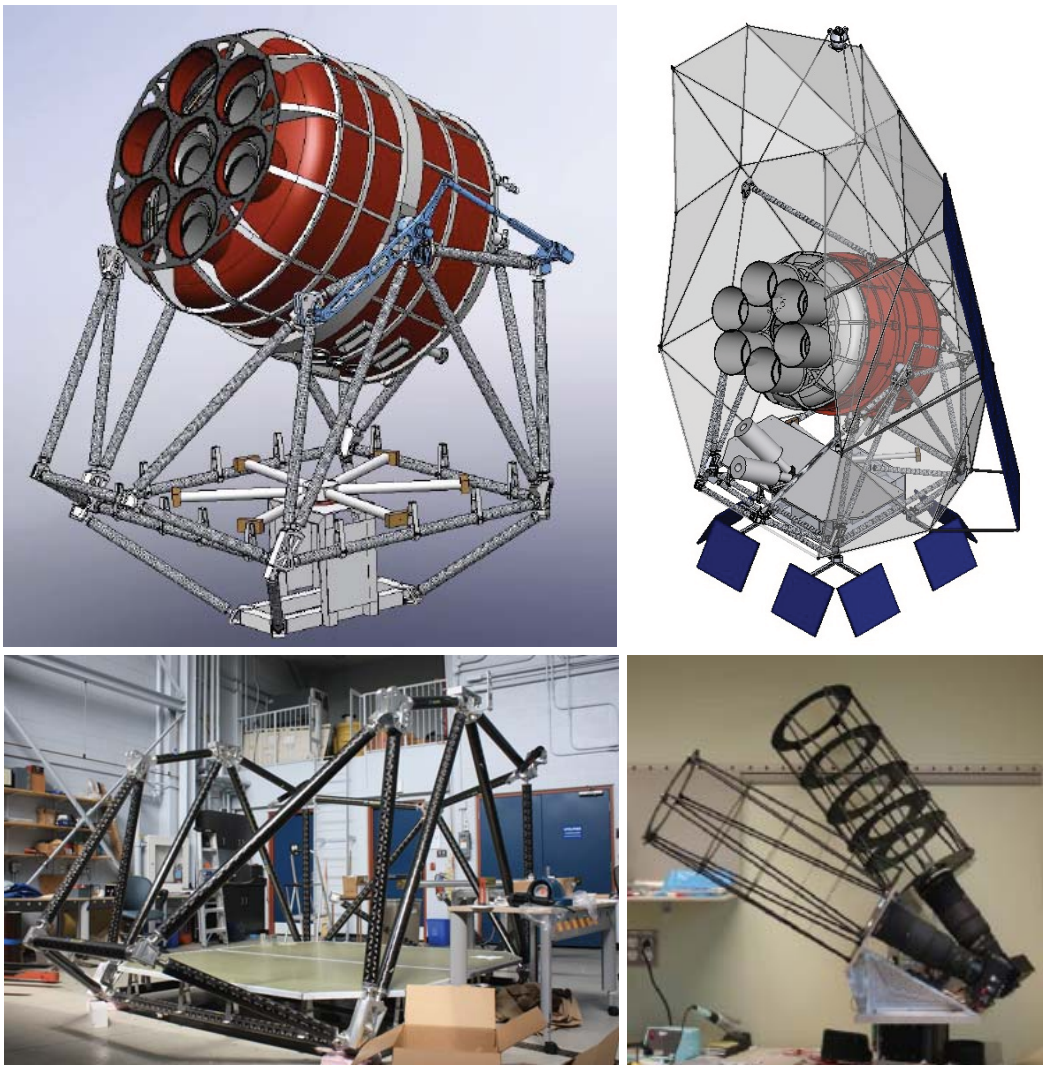

Figure 2.3: The SPIDER gondola. *Top left*: The carbon fiber support structure (grey) includes a rollover bar (bottom left of image). The elevation drive (highlighted in blue) is powered by two linear actuators. Rotation is controlled by a reaction wheel below the cryostat. The reaction wheel motor and the Support Instrumentation Package (SIP) provided by the balloon facility are mounted below the wheel. *Top right*: Three roughly equally tensioned suspension cables attach the pivot (at top) to joints in the gondola frame. A spreader bar between the two front cables reduces compression forces. The star cameras are mounted on the floor below the cryostat. The sun shield (drawn transparent) wraps around the back of the gondola. A large solar array is mounted on the side and smaller arrays around the bottom. Drawings credit: J. Soler. *Bottom left*: Assembled carbon fiber reinforced polymer tubes with aluminum joints and Hexcel floor. The frame meets strength requirements with a mass of just 330 lb. *Bottom right*: Assembled star camera.

expect an rms uncertainty of 1' in SPIDER pointing reconstruction. Regular observations of bright compact sources during flight will be used to monitor beam centroid offsets.

2.5 Cryogenics

The team at Princeton University is responsible for the design and characterization of the SPIDER flight cryostat, which was custom built by Redstone Aerospace[1]. The thermal architecture of the cryostat is shown in Figure 2.4 and described in detail in Gudmundsson et al. [52]. With a 1,284 L main helium tank maintained at ∼1 atm, the unit is designed to provide at least a 25-day hold time. Helium gas boil off from the main tank is coupled through heat exchangers to inner and outer vapor-cooled shields (VCS1 and VCS2) that thermally shield the 4 K stage. The enthalpy of the gas provides sufficient cooling to these stages to obviate the use of liquid nitrogen, simplifying design and reducing mass. The long narrow winding vent tube is susceptible to nitrogen ice plugs, so care is taken to maintain a positive outflow of gas during cryogen fills and operation. The helium bath and vapor-cooled shields are encased in a cylindrical vacuum vessel 2.05 m tall and 2.43 m in diameter. The dry weight of the cryostat (no LHe or telescope inserts) is about 850 kg.

Inside the inner radiation shield (VCS1) a small 16 L superfluid helium tank is capillary fed by the main helium tank. This tank will be vacuum pumped to a few hundred pascal prior to launch and then capped off. At float a valve will open to vent the tank to ambient atmospheric pressure (∼100 pascal), which will maintain the helium in its superfluid state at a temperature of about 1.6 K. This cooling point is used to cycle the ^{3}He adsorption refrigerators that cool each focal plane.

The cryostat was designed to sustain nonparasitic heat loads of 12 mW, 550 mW, 4 W, and 9 W to the superfluid tank, main tank, VCS1 and VCS2, respectively. As of this writing, the cryostat has been built and is undergoing testing at Princeton. The cool down process takes about a week from 300 K to 300 mK and the cryostat currently achieves a hold time of about 20 days under flightlike loading.

The sub-Kelvin focal plane architecture is described in detail in Runyan et al. [107]. An assembled focal plane assembly is pictured in Figure 2.5. SPIDER's focal plane architecture (the "RevX" design) differs from the ("RevE") architecture employed by KECK (our sister

[1] http://www.redstoneaerospace.com/

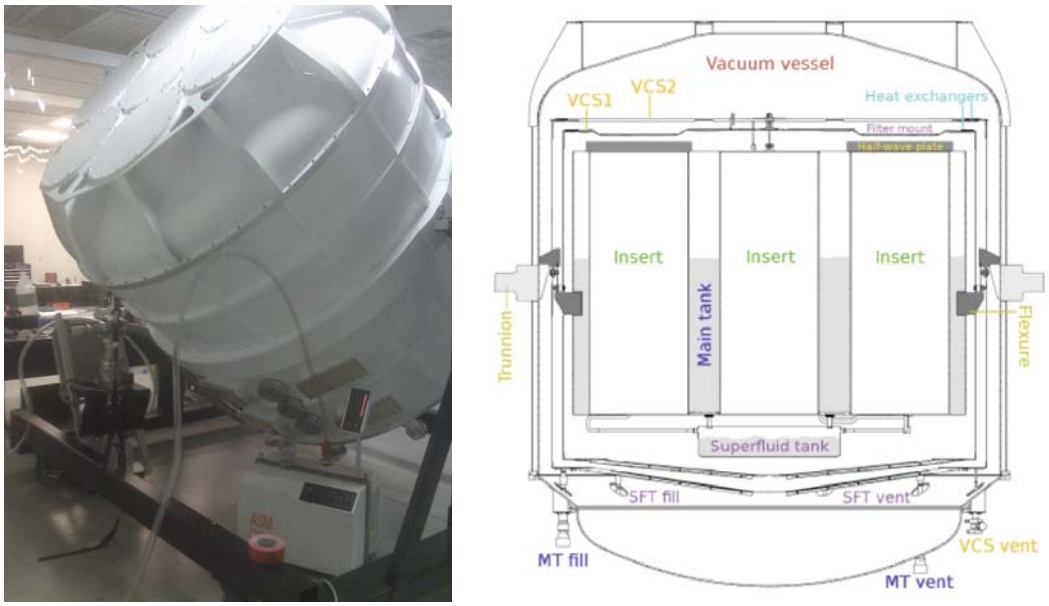

Figure 2.4: *Left*: The SPIDER flight cryostat. *Right*: Cross-sectional drawing showing the main liquid helium tank, superfluid helium tank, vapor-cooled shields (VCS1 and VCS2), and the vacuum vessel. Trunnions on the vacuum vessel walls attach to the gondola elevation drive. Flexures support the vapor-cooled shields. The main tank vent lines pass through heat exchangers at VCS1 and VCS2 before exhausting to atmosphere. The large cryostat will accommodate six modular telescope inserts. Cooling for adsorption fridges is provided by the 1.6 K superfluid helium tank which is pumped by ambient atmospheric pressure at float ($\sim$100 pascal) and is capillary fed by the main tank.

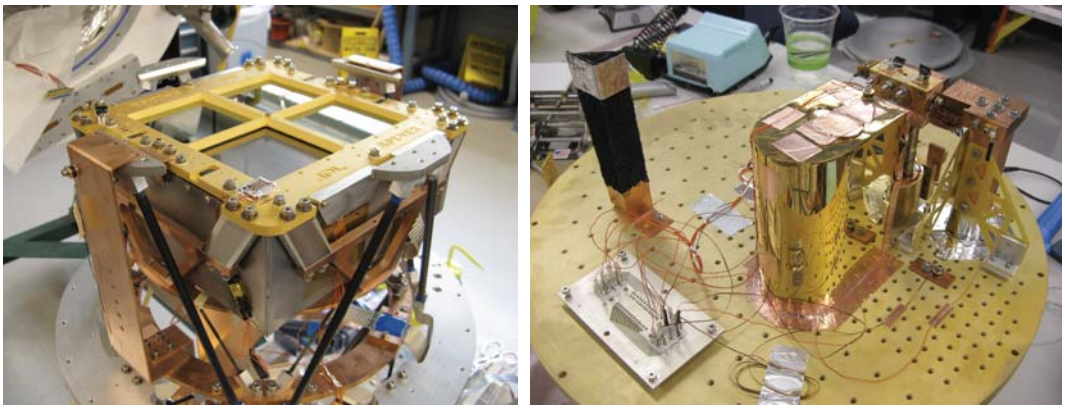

Figure 2.5: *Left*: An assembled focal plane unit with the A4K outer shield ("spittoon") removed. The spittoon is mechanically supported by black carbon fiber rods from the aluminum 4 K plate and cooled by copper straps bolted to the 1.6 K ring. The sub-Kelvin stage is mechanically supported off of this 1.6 K ring, and cooled by the ^{3}He fridge. The gold plated copper detector plate, with a Cernox thermometer and heater, is coupled to this cold stage by (diagonal) stainless steel struts which act as a passive thermal filter. The square niobium box which encases the SQUID multiplexing system is visible just behind these struts. *Right*: ^{3}He adsorption refrigerator mounted on a gold-plated aluminum plate (4 K). A copper thermal bus bar feeds through the plate (right side of image) to couple the fridge condensation point to the superfluid helium bath (1.6 K).

experiment on the ground) due to more stringent magnetic shielding requirements (discussed in §2.8). Marc Runyan performed much of the focal plane redesign, which has substantially reduced magnetic pickup in the SQUID system (see §4.9).

A gold-plated aluminum cold plate at the base of each telescope insert mounts to the main liquid helium tank. The optics truss structure and a simple closed-cycle ^{3}He adsorption refrigerator are mounted on this plate. A 1.6 K gold-plated copper bar from the superfluid helium tank is fed through a hole in the base plate to provide cooling to the fridge condensation point as well as to a magnetic shield and to the blackened cold sleeve which lines the optics tube. The 10 stp-liter ^{3}He fridges (one pictured in Figure 2.5) are produced by Simon Chase Research. They can provide a steady base temperature of around 300 mK to the detector plate with a hold time of three days. In flight they will be recycled every 72 hr.

To cycle a fridge in the test cryostat, we heat the pump to 30 K after confirming that the heat switch is below 10 K and that the condensation point is below 2 K. Once the the fridge temperature reaches 30 K, we set the heater power to 30 mW and allow ^{3}He gas to

condense in to the still for 30 min. We then turn off the pump heater and apply 0.7 mW to the heat switch to cool the pump.

The fridge cools the focal plane through eight stainless steel blocks that are gold plated on either end to minimize thermal impedance. We have measured a total thermal impedance from fridge to focal plane of 2.3 mK/W. Stainless steel has a large heat capacity, so the blocks act to filter out any high-frequency thermal fluctuations on the fridge side of the thermal link. The 3 dB point of the thermal transfer function has been measured at 2 mHz.

Four detector tiles are secured against the square detector plate with beryllium copper clips and are held in alignment by pins and slots. Over a hundred gold wire bonds per tile make a thermal connection between the gold-plated copper plate and large gold bond pads near the edge of the detector tile (Figure 3.3). Becky Tucker has measured an overall plate-to-tile thermal conductance of 245 μW/K at 300 mK (limited by Kapitza resistance). An NTD Ge thermistor is mounted on each tile for temperature monitoring.

A niobium back short is positioned a quarter-wave distance behind the detectors to define a boundary condition that forces constructive interference at the antenna. All stages of the SQUID multiplexing system are behind the back short encased in several layers of magnetic shielding. Superconducting electrical connections between the TES detector tiles and the SQUID system are achieved through the use of flexible aluminum circuits and aluminum wire bonds.

2.6 Optics

SPIDER is an array of six individual monochromatic telescopes encased in a single cryostat housing (see Figure 2.6). Modularity simplifies half-wave plate design and antireflection coating of optical components because each individual telescope tube operates in a single frequency band. Pairs of telescopes observing in each band are oriented such that their polarization sensitivity differs by 45°. This enables simultaneous measurement of the Stokes parameters Q and U.

Targeting large angular scales allows SPIDER to use compact 2-lens telecentric refractor optics. A 24 cm aperture is sufficient to provide subdegree resolution in SPIDER's frequency bands. The projected full width half maxima (FWHM) of SPIDER's far field beams are 49' at 93 GHz, 30' at 148 GHz, and 17' at 280 GHz. Small apertures simplify baffling and allow

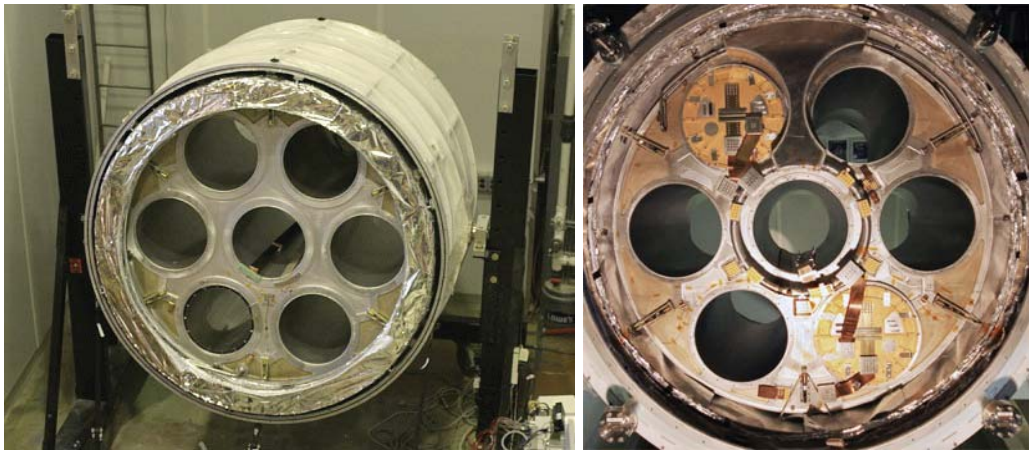

Figure 2.6: The SPIDER flight cryostat can accommodate up to seven modular telescope inserts. However, we only plan to instrument the outer six insert bays. The inner bay may be used for thermal busses and a carbon getter to improve the quality of the vacuum. Telescope inserts (Figure 2.7) slide in to the bottom of the cryostat and bolt at the base, as shown in the image at right.

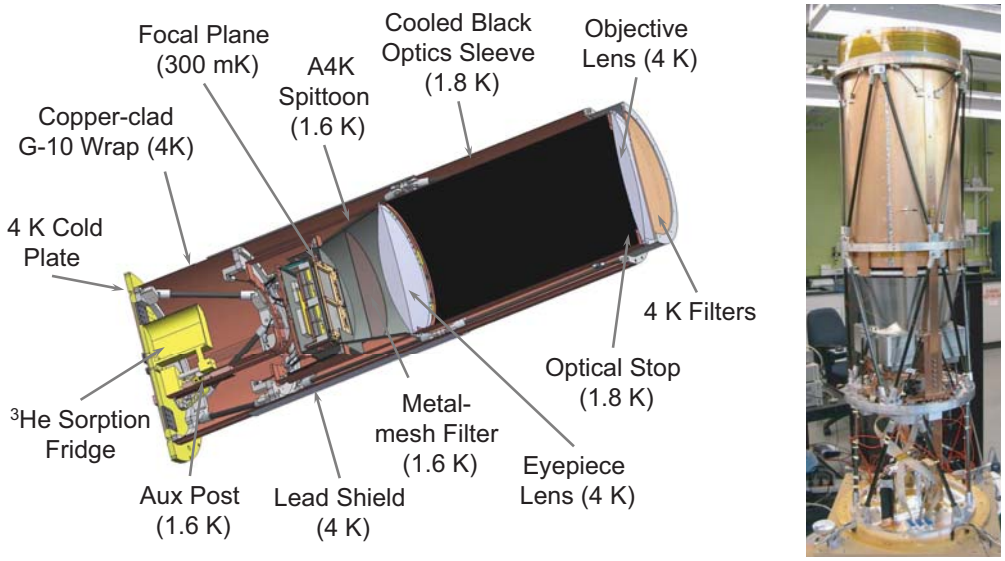

Figure 2.7: *Left*: Cross-sectional drawing of a telescope insert. Drawing credit: M. Runyan. *Right*: Photo of one of SPIDER's six telescope inserts with the lead shield and G-10 wrap removed. The A4K spittoon (not shown in Figure 2.5) is visible here shielding the focal plane unit. Just above, the eyepiece lens is mounted on copper flexures. The copper sleeve lining the inside of the optics tube above the eyepiece is blackened on the inside and cooled to 1.8 K by a copper strap. Lightweight carbon fiber trusses and aluminum rings provide the mechanical structure of the telescope tube, and are bolted to the 4 K gold plated aluminum base plate. The entire telescope insert slides in to the bottom of the cryostat, and the base plate is bolted to the helium-cooled 4 K stage.

preflight characterization in the far field of the optics because $D^2/\lambda \approx 30$ m.

A cross section of the optics tube is shown in Figure 2.7, and SPIDER's optics are described in Runyan et al. [107]. A blackened sleeve lines the inside of the telescope tube between the eyepiece and objective lenses. The blackened Lyot stop caps the top of this sleeve just below the objective lens, preventing beam spillover on to warmer surfaces skyward of the objective. The antenna beam is approximately a *sinc* function, and the telescope aperture nearly coincides with the null between the main beam and the four primary side lobes. Primary and secondary side lobes are all terminated inside the telescope on the blackened stop and sleeve. Because 25% of the antenna beam power is in these side lobes, we achieve a substantial reduction in in-band loading (§4.5) by cooling the sleeve and stop to 1.8 K using the superfluid helium tank. The lenses and wave plate are cooled to 4 K using the main helium tank. Decreasing loading reduces photon noise in the detectors, allowing SPIDER to better take advantage of the favorably low atmospheric loading conditions at float.

SPIDER's optical design is based on the BICEP design [124] and its lenses are identical to those of BICEP2. The lens optimization process is discussed in Aikin et al. [2]. The plate scale is 0.98°/cm at the focal plane and the corner-to-corner field of view of each insert is 20°. High-density polyethylene slabs used for SPIDER's lenses are annealed to relieve stress before they are rough cut, before final machining, and again as part of the antireflection coating process. CMM surface metrology confirms that the correct figure has been achieved. During cooling to 4 K the HDPE lenses contract by 2% while the aluminum rings that support them contract by only 0.4%. For this reason, the lenses are held in place by equally spaced 1/32" thick copper flexures which absorb the differential contraction, keep the lenses centered, and provide a cooling path to the 4 K helium bath.

SPIDER utilizes a variety of filters to reduce the heat load on the helium bath while maximizing in-band transmission. The filtering system includes hot-pressed metal-mesh filters [1], infrared "shaders" [120], and a lossy nylon filter. Just skyward of the detector plate, a metal-mesh filter (7 cm^{-1} cutoff for the 148 GHz band) forms a light tight seal with the A4K magnetic shield ("spittoon"). This filter removes above-band radiation which might otherwise couple to the antennas or to the TES island itself. Specifically, it rejects a "blue leak" that we have discovered which contains $\sim 85\%$ of its power below 450 GHz with $\sim$50% in frequencies between 220 and 270 GHz.

The rest of SPIDER's filter stack packs tightly in to the space between the objective lens and the vacuum closeout window. A 3/32" thick nylon filter and a hot-pressed filter (10 cm^{-1} cutoff for the 148 GHz band) are mounted on the telescope insert structure just skyward of the objective lens at 4 K. The half-wave plate (§2.7) is next in the optical train, secured to the cryostat itself at 4 K. A hot-pressed filter (12 cm^{-1} cutoff for the 148 GHz band) and three IR shaders intercept radiation at the first vapor-cooled shield (VCS1). The VCS1 stage equilibrates just above 10 K in the SPIDER test cryostat and around 30 K in the SPIDER flight cryostat. Four IR shaders mount to the ∼90 K VCS2 stage.

The vacuum enclosure is sealed by a thin window above each telescope insert. The current plan is to use 0.001" thick teflon for these windows, but this may be changed as it has been suggested that teflon can introduce undesirable beam effects. The thin windows are protected from atmospheric pressure while on the ground by much thicker windows, which retract when the instrument reaches float altitude.

Reflections can introduce ghost beams. A reflective niobium back short is located a quarter-wave distance behind the detector plate to set up constructive interference in the plane of the antennas. The lenses, nylon filter, hot-pressed filters, half-wave plate, and silicon detector wafers are all coated with quarter-wave antireflection coatings ([51], §4.4). NSG-N quartz antireflection tiles are sandwiched between the sky side of the silicon detector tiles and the detector plate. For the lenses and nylon filters we use Porex[2] porous Mupor membranes because they are pliable and available with indices and thicknesses well matched to our lenses and filters. We select PM23DR for the HDPE lenses and PM23JR for the nylon filters. Adhering the Porex coatings is most difficult on the curved lens surfaces. A silicon vacuum bag presses the coatings firmly and evenly against the lens (or filter) as it rests on a matching concave (or flat) aluminum plate. A thin, low-density polyethelene (LDPE) sheet is then melted (10 hr at 124°C) at the interface between them. This lamination process has been successfully demonstrated, with wrinkle-free coatings showing no signs of delamination after $\gtrsim$10 thermal cycles. The nylon and teflon surfaces are abraded with Scotchbrite and then thoroughly cleaned prior to bonding. When coating lenses, the LDPE film must be prestretched to match the curvature of the lens to avoid wrinkling. Porex materials easily pick up static charge, dust, and oils, and should be handled using gloves.

[2] http://www.porex.com/

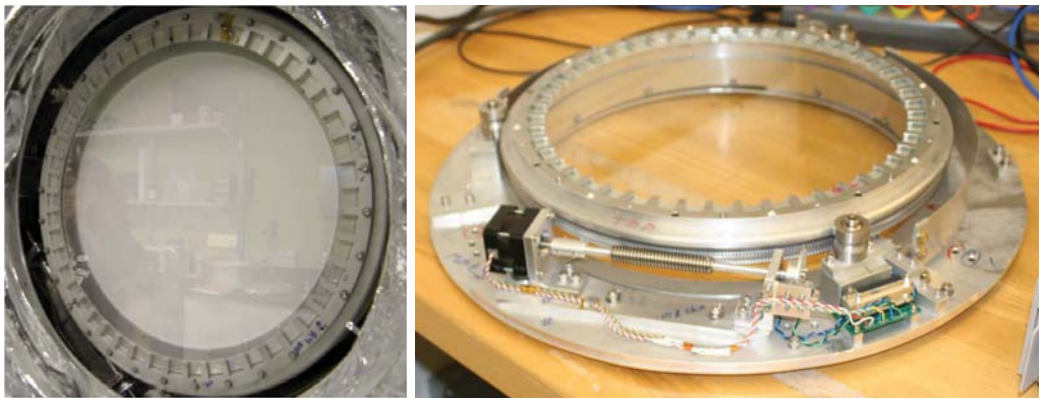

Figure 2.8: *Left*: A sapphire half-wave plate mounted in the optical receiver test bed at Caltech. *Right*: The rotor is coupled to a stepper motor by a worm gear.

2.7 Half-Wave Plates

To modulate polarization sensitivity in flight, SPIDER utilizes cold (4 K) stepped sapphire half-wave plate (HWP) assemblies developed at Case Western Reserve University and described in Bryan et al. [25]. Each telescope insert employs a single HWP located just skyward of the objective lens (see Figure 2.8). In flight the plates will all be rotated by 22.5° daily. This rotates the polarization sensitivity of the focal planes and allows each pixel to measure both Stokes parameters Q and U. Following each HWP rotation, the instrument will scan compact sources for about 30 minutes to check pointing offsets and beam profiles. The HWP rotates the polarization sensitivity of the telescope without rotating the beam, mitigating systematic effects due to small beam asymmetries and enabling reconstruction of small polarization signals with high fidelity. A SPIDER-style wave plate is currently successfully operating in the KECK array at the South Pole.

Sapphire is anisotropic and birefringent, with a single axis of anisotropy. Incoming radiation can be decomposed into two polarization components: along the axis of anisotropy (extraordinary ray) and perpendicular to the axis of anisotropy (ordinary ray). Inside the sapphire the refractive index for the extraordinary ray (n_e) differs from the index for the ordinary ray (n_o), so the rays propagate at different speeds. Following [51], for a wave with free space wavelength λ_0 passing through a sapphire plate of thickness d, the relative phase

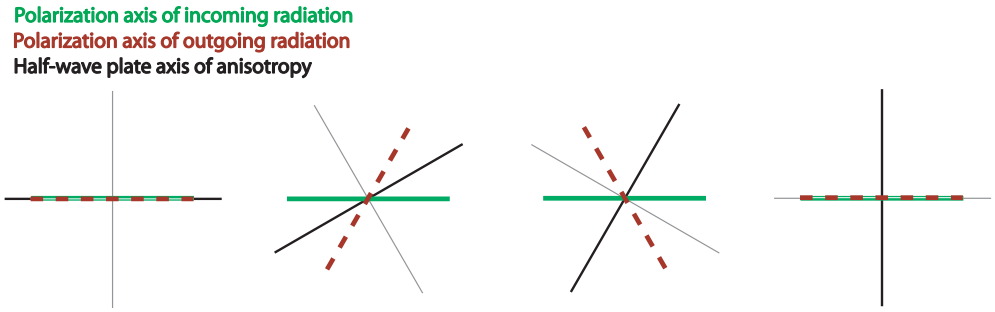

Figure 2.9: A half-wave plate rotates the polarization axis of radiation passing through it. The amount of rotation is a periodic function of the angular orientation of the half-wave plate with respect to the polarization axis of the incoming radiation (with period $\pi/2$).

offset introduced between the two polarizations is given by

$$\delta\phi = \frac{2\pi d(n_e - n_o)}{\lambda_0}. \tag{2.1}$$

Neglecting loss, a wave entering the sapphire with

$$\tilde{\mathbf{E}}_{in} = \tilde{E}_0(\hat{e}_0 \cos\alpha + \hat{e}_e \sin\alpha) \tag{2.2}$$

will exit the sapphire with

$$\tilde{\mathbf{E}}_{out} = \tilde{E}_0 e^{i\phi}(\hat{e}_0 \cos\alpha + \hat{e}_e \sin\alpha e^{i\delta\phi}). \tag{2.3}$$

By definition, the thickness of a half-wave plate is chosen such that $\delta\phi = \pi$, so

$$\tilde{\mathbf{E}}_{out} = \tilde{E}_0 e^{i\phi}(\hat{e}_0 \cos\alpha - \hat{e}_e \sin\alpha). \tag{2.4}$$

The polarization of the outgoing wave has been rotated by an angle 2α (see Figure 2.9).

Having covered the basic optical function of the half-wave plate, we must now address the real physical system. Examining Equation 2.1 we see that for any thickness d, the sapphire acts as an ideal half-wave plate ($\delta\phi = \pi$) for only a singular value of frequency λ_0. Real passbands are finite, so sapphire thicknesses are optimized for the center frequencies of each band.

Sean Bryan at Case Western University has done the majority of the work to develop and

characterize the wave plate system. His measurements of the spectral indices of sapphire plates and a discussion of systematics are reported in [25]. In [26], a detailed optical model using the Mueller matrix formalism is presented.

Sapphire is a relatively high index material ($n > 3$), so antireflection (AR) coating is crucial. For this purpose, we use quarter-wave thickness Herasil fused quartz. Thickness is specified based on the band center. A quarter-wave in fused quartz at 148 GHz is only 0.28 mm, so the AR coatings are very mechanically fragile.

The rotor and three spinner bearings are driven by a worm gear coupled to a stepper motor. A heat strap provides thermal conductivity between the base plate and rotor. The target specification for wave plate position measurement is 0.1°. The holes of the worm gear shaft encoder are 2.35' apart. There are tick marks every 0.5° on the rotor, with a unique tick mark pattern every 22.5° for absolute position. All encoders are read out using LED/photodiode pairs.

2.8 Magnetic Shielding

SPIDER has much stricter magnetic shielding requirements than sister ground experiment KECK because SPIDER targets larger angular scales on the sky. Further, the motion of SPIDER's observing platform reduces our ability to model and accurately separate pickup associated with Earth's magnetic field. TES devices are susceptible due to the dependence of transition temperature on magnetic field strength. According to BCS theory [7], the transition temperature of a bulk Type I superconductor depends on magnetic field as

$$\Delta T_c(H) \approx T_{c,o}\left(1 - \sqrt{\frac{H}{H_0}}\right). \tag{2.5}$$

Therefore, a change in magnetic field ΔH looks the same as a change in CMB temperature ΔK_{CMB} where

$$\frac{\Delta K_{CMB}}{\Delta H} \approx -\frac{1}{2} H_0^{-1} \alpha P_{sat} \left(\frac{dP}{dT_{RJ}}\right)^{-1} \left(\frac{dT_{CMB}}{dT_{CMB,RJ}}\right). \tag{2.6}$$

For $H_0 \approx$ 50–100 gauss [85], $\alpha \approx$ 100–1000, $P_{sat} \approx$ 1–2 pW, $dP/dT_{RJ} \approx 0.15$ pW/K$_{RJ}$ and $dT_{CMB}/dT_{CMB,RJ} \approx$1.7, I find an anticipated $\Delta K_{CMB}/\Delta H$ on the order of tens or at most hundreds of μK$_{CMB}$/nT. Due to magnetic shielding around the focal plane, we have not

yet seen evidence of magnetic pickup in the TES (see §4.9). Instead, the sensitive SQUID system dominates the measured magnetic field response.

The SQUID multiplexing system transmits information through magnetic induction and is thus inherently responsive to magnetic fields. NIST has fabricated the SQUID inductive loops in a counterwound cloverleaf pattern as 2nd-degree gradiometers [115], but variations in magnetic flux still produce a shift in the V-ϕ curve. NIST has also minimized the effective loop area of the superconducting loops which sum the the signals from all of the first stage SQUIDs to pass to the second stage SQUIDs. However, this loop may still exhibit magnetic coupling.

In early SPIDER testing we found that existing shielding was not sufficient to adequately shield the SQUID system from Earth's magnetic field. SPIDER's magnetic field rejection strategy has since been completely redesigned. Marc Runyan led this effort, and SPIDER's magnetic shielding system is described in detail in Runyan et al. [107]. Each optics tube is lined with a high permeability shield along the full length of the helium tank. Outside of this we wrap a superconducting lead sleeve which is 20" long and roughly centered on the focal plane. The niobium backplane of the detector tile and the nioubium back short located $\lambda/4$ behind the detectors expel magnetic field through the Meissner effect. The SQUID multiplexing system is located behind the back short within many layers of superconducting boxes and high-permeability boxes. I describe our measurements of magnetic response in §4.9.

2.9 Simulations

We use a simulation pipeline with heritage from the BOOMERANG03 experiment [90] to select SPIDER's observation strategy, to quantify the impact of instrument systematics, and to evaluate SPIDER's sensitivity to its target science goals. The simulation effort is lead by Carrie MacTavish.

To optimize its sensitivity to B-modes, the SPIDER instrument must carefully control any systematic effects that might introduce false B-mode signal. In 2008, MacTavish et al. [88] introduced the simulation pipeline and established baseline specifications for various instrument parameters, including detector noise characteristics, pointing jitter, payload pendulations, polarization angle offsets, beam systematics, and receiver gain drifts. In

2011, O'Dea et al. [95] quantified the systematic effects associated with several measured instrument characteristics, including the impact of the frequency-dependent response of the half-wave plates, the response of the SQUID system to Earth's magnetic field, and beam mismatches and asymmetries. A model of diffuse polarized foreground emission was also developed to guide observation strategy.

Both MacTavish et al. and O'Dea et al. were written when the baseline flight plan was a launch from Alice Springs, Australia, with SPIDER mapping more than half of the sky by continuously spinning at 36°/s. As I have described in this chapter, this is no longer SPIDER's flight plan. The collaboration has recently begun a very active simulation effort (concurrent to this writing) to perform thorough simulations that are representative of SPIDER's intended flight plan and measured performance. Fraisse et al. [45] presents some preliminary results from this effort.

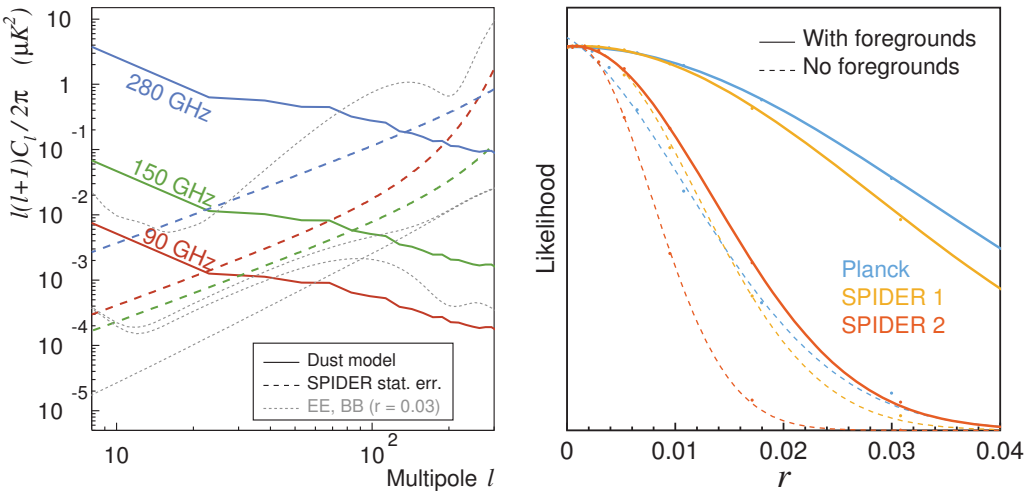

Figure 2.10: Figures from [45]. *Left*: The power spectra of the polarized dust foreground model described in [95] in SPIDER's observing region. Also shown are SPIDER's projected statistical errors (assuming optimistic sensitivity targets ∼20% better than those currently achieved) as well as the E- and B-mode polarization signals assuming a tensor-to-scalar ratio of r=0.03. The inflationary gravitational wave B-mode and gravitational lensing B-mode signals are shown separately, and then added together to give the full B-mode signal. *Right*: Marginalized r likelihood curves for SPIDER and PLANCK HFI, with and without foregrounds. The addition of the 280 GHz band in the second flight provides significant leverage for foreground subtraction.

Chapter 3

Detectors and Readout

Bolometers and HEMT amplifiers have long played central roles in instrumentation for CMB science. SPIDER benefits from decades of bolometer technology development (§3.1). The most important innovations bringing SPIDER's B-mode science goals within reach are new detector and readout technologies that have enabled a dramatic increase in pixel counts. Detector tiles combine polarized beam-forming elements (slot antenna arrays), band-defining (LC microstrip) filters, and bolometers on a single substrate (§3.2). All of these components are fabricated for hundreds of devices at a time in an entirely photolithographic process (§3.3). Voltage-biasing superconducting bolometers in the steep transition between their superconducting and normal states establishes an electrothermal feedback mechanism that greatly increases their speed (§3.4). This enables time-domain multiplexed readout using cryogenic SQUID amplifiers coupled with multichannel warm electronics (§3.5).

3.1 Bolometric Technology Development

A stratospheric balloon experiment in the early 1970s made the first astronomical use of a ^{3}He cooled bolometer, and showed that the spectrum of the CMB was approximately that of a 3 K black body [123]. That mission, and other balloon and rocket experiments, pioneered bolometer technology for use on a space telescope [105]. In 1990 the four bolometers of COBE's FIRAS instrument, operating at 1.5 K with electrical NEP of order 4 fW/$\sqrt{\text{Hz}}$, measured the blackbody spectrum of the CMB and changed cosmology forever [92].

The results of the COBE experiment inspired an effort to characterize the degree-scale anisotropies of the CMB, which required a new generation of detector technology. This challenge was met with the development of neutron transmutation doped (NTD) germanium

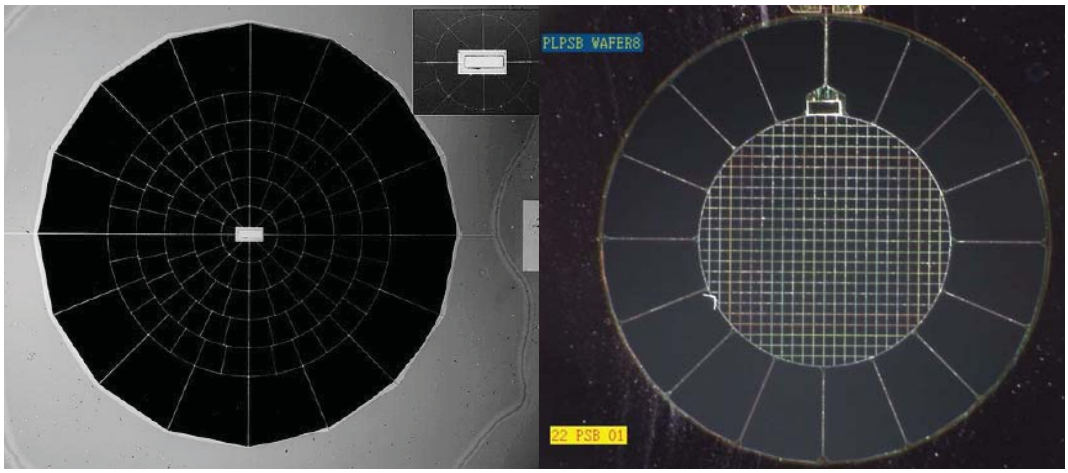

Figure 3.1: Thermally isolated metalized Si_3N_4 absorbers coupled to Ge NTD thermistors. *Left*: "Spider-web" bolometer flown on BOOMERANG [31]. The absorber is 4 mm in diameter. Inset shows NTD. *Right*: Polarization sensitive bolometer (PSB) [66] flown on B2K [90].

semiconductor thermistors [56]. These thermistors, typically operated below 1 K, were coupled to cooled junction field effect transistor (JFET) preamplifiers. The germanium NTD doping process produces a homogenous distribution of donors and acceptors. The availability of various isotopes of germanium allowed for the independent control of acceptor and donor concentrations. This facilitated the production of devices with better uniformity and a stronger dependence of resistivity on temperature, increasing the sensitivity of the thermistors. The simplicity and uniformity of devices enabled the development of arrays with pixel counts approaching a hundred. The move from single detectors to arrays allowed receivers to begin to distinguish between astronomical sources and sky noise.

This advance in thermistor technology was met with an equally important advance in absorber technology. New mesh "spider-web" absorbers were made from a micromachined silicon nitride (Si_3N_4) membrane. The new geometry minimized absorber volume and heat capacity, which sped up detectors while reducing their cosmic ray cross section. A metallization on the mesh coupled directly to electromagnetic radiation, and the temperature of the mesh was read out by a NTD Ge thermistor bump bonded onto the absorber. Arrays of NTD thermistors on spider-web absorbers enabled a whole generation of experiments, including MAXIMA, BOOMERANG, ARCHEOPS, QUAD, ACBAR, BOLOCAM, and PLANCK HFI. These experiments have made, and continue to make, cutting-edge measure-

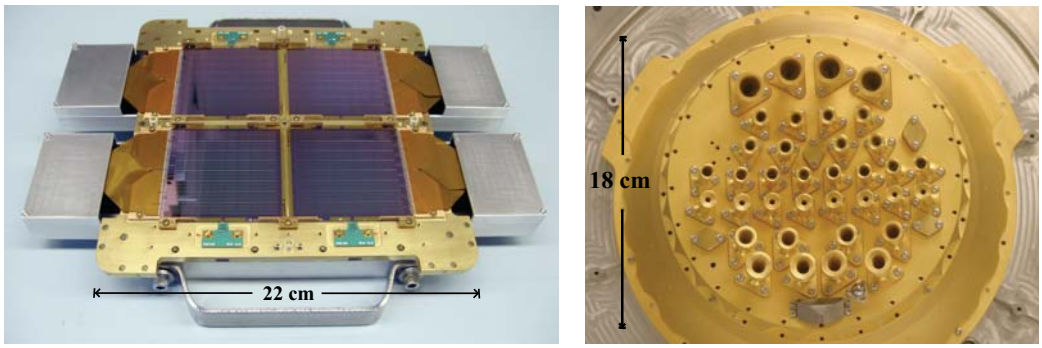

Figure 3.2: New technologies have enabled a large increase in focal plane packing density. *Left*: One of SPIDER's six detector plates. This unit is populated by 512 bolometers. The handles and the four Al boxes which protect the flexible circuit lines are removed prior to integration in the telescope. *Right*: Feed horns on the front end of the PLANCK HFI focal plane, which accommodates 52 bolometers.

ments of the intensity of the CMB over a wide range of frequencies and angular scales.

Precise measurements of the polarization properties of the CMB required another generation of innovation. At the turn of the century, polarization sensitive bolometers (PSBs) were developed by a collaboration between NASA's Jet Propulsion Laboratory and Caltech [66]. Replacing the symmetrical spider-web mesh absorber with a one dimensional grid absorber enables linearly polarized bolometric detection. Dual polarization PSBs consist of two absorber grids which are orthogonal, cocentered, and closely separated. The two grids, coupled to separate NTD Ge thermistors, are responsive to orthogonal polarization states. Polarization sensitive NTD bolometers have been used on experiments like B2K, BICEP, and now PLANCK HFI.

For these experiments, corrugated feed horns were fabricated individually for each detector, mounted on a focal plane, and cooled to sub-Kelvin temperatures. Mass, volume, thermal, and fabrication constraints prohibit the use of this kind of large feed horn technology in newer experiments which increase pixel counts by more than an order of magnitude. Therefore, some large format experiments, like SPT, EBEX, and APEX, use monolithic arrays of small smooth conical feed horns to couple radiation to absorbers. SPIDER, and its sister ground based experiments BICEP2 [96, 22] and KECK [110], take an entirely different approach, absorbing radiation in photolithographed slot antenna arrays coupled directly to bolometers on the same Si wafer (see [50, 76, 75]). A third approach, developed by a team led by Adrian Lee, couples antennas to the sky through small hyperhemispherical Si lenses.

These three approaches are detailed in [17] in the context of technology development for a space mission.

3.2 SPIDER Detector Architecture

SPIDER's beam-forming antennas, band-defining filters, and bolometers are all fabricated together on a silicon wafer in an entirely photolithographic process. The design and early development of the detector technology is described in detail by Kuo et al. [75, 76].

Each SPIDER focal plane is made up of four detector tiles (Figures 3.2 and 3.3). Within the tiles, pixels are organized on a grid with $\sim 2F\lambda$ spacing. The 7.3 cm square tile size permits $8 \times 8 = 64$ pixels per 148 GHz tile and $6 \times 6 = 36$ pixels per 93 GHz tile. Two bolometers read out orthogonal polarizations for each pixel. A 148 GHz focal plane therefore contains $4 \times 64 \times 2 = 256$ bolometers.

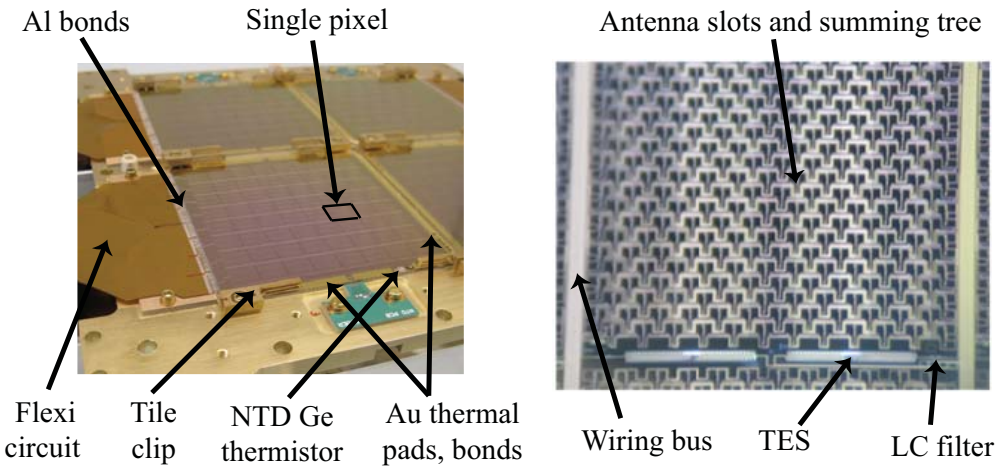

Figure 3.3: *Left*: Detector tiles are secured against a detector plate by tile clips and kept in alignment by pins and slots. A niobium wiring bus carries bolometer signals to bond pads along a single tile edge. Aluminum wire bonds bridge to aluminum "flexi circuits" which provide a superconducting connection to the SQUID readout system located within a magnetically shielded enclosure behind the detector plate. Large gold pads near the edges of the tiles are heat sunk to the gold-plated copper detector plate by gold wire bonds. A NTD Ge thermistor records the temperature of each tile. *Right*: A single pixel. Two interleaved slot antenna arrays cover most of the surface area of the pixel. They couple to orthogonal polarizations of incoming radiation. The signal from each antenna array passes through a LC band-defining filter before thermally coupling to a TES bolometer.

Bolometers themselves are largely incoherent; they must be coupled to incoming radiation by a beam-forming element. In SPIDER, this function is performed by dual-polarization slot antenna arrays (details, Figure 3.4). Every pixel contains one phased array of slot dipole antennas for each of the two measured orthogonal polarizations. The two polarized antenna arrays are interleaved and perfectly cocentered. Rotating one of the slot arrays 90° about the center of the antenna exactly reproduces the slot array for the other polarization.

The measured fractional bandwidth of the antenna is $\gtrsim$30%. Between the antenna and the bolometer, an in-line 3rd-order Chebyshev microstrip filter (Figure 3.5) crops the fractional bandwidth to 25%. These LC filters are constructed from coplanar waveguide (CPW) inductors and stub capacitors. The capacitance of the stubs depends on the thickness of the interlayer dielectric (SiO_2 layer between the stubs and the niobium ground plane). Significant changes to a band center require scaling the antenna. Smaller changes can be made by substituting an alternate filter design or by modifying the thickness of the sputtered interlayer dielectric to alter the capacitance of the filter and shift the band.

The bolometer island is suspended on silicon nitride (Si_3N_4) legs. Because the niobium ground plane is cut out around the island when it is isolated, the island is not shielded from direct coupling with incident radiation. The long meandered design of the silicon nitride legs (Figure 3.6) provides a small thermal conductance within a narrow geometry, minimizing the gap between the ground plane and the long edge of the island.

After passing through the band-pass filter, the trunk of the niobium microstrip summing tree from the antenna bridges on to the island where it terminates on an open-ended resistive gold meander which efficiently dissipates the electrical power on to the island as heat (Figure 3.7). The dissipated heat is measured by a thin film of titanium, a thermistor called a Transition Edge Sensor (TES). By voltage biasing the TES, the island is maintained at a temperature in the transition between the superconducting and normal states of the titanium where it is highly sensitive to small temperature variations. The basics of bolometer operation, and of TES bolometers in particular, are reviewed in §3.4.

In designing our bolometers, we prefer to optimize their performance for the anticipated in-flight loading conditions. However, a superconducting bolometer that is optimized for flight loading conditions will saturate under room temperature loading. This would frustrate spectroscopy and beam mapping measurements. To circumvent this problem, we use a dual-TES architecture. Titanium and aluminum TES' are wired in series on the same island.

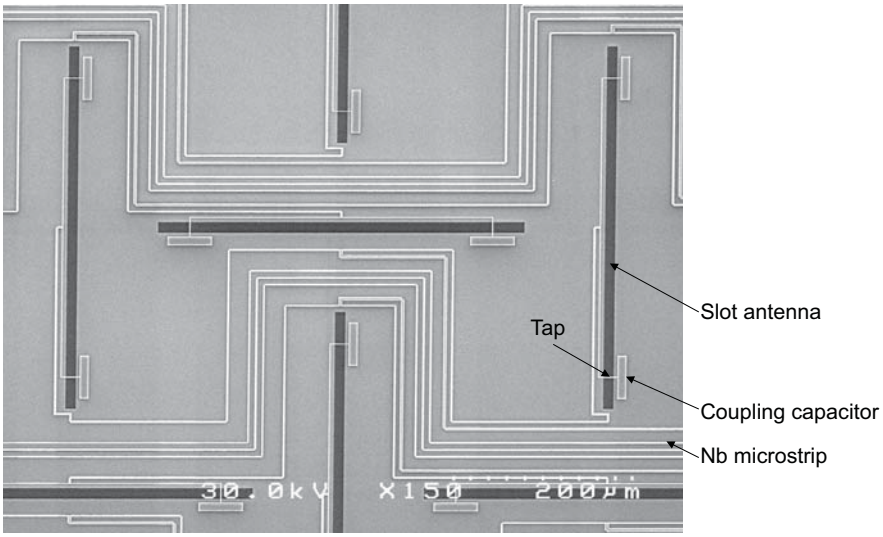

Figure 3.4: SEM micrograph of a portion of a slot antenna array. Radiation excites electric fields across slots cut out of the niobium ground plane. Taps running over top of these slots couple to radiation polarized orthogonally to the long edge of the slot. Two interleaved perpendicular sets of slots comprise independent arrays. For each array, the tapped signal from all of the slots is added together by a niobium microstrip summing tree to form a single compound antenna. The summing tree is a network of tapered microstrip lines which meet at T-junctions to combine the signals from the taps at equal phase and amplitude. Future implementations of the summing tree may taper the amplitude of the excitation of slots to reduce sidelobe response. To match the (primarily real) impedance of the microstrip summing tree, a coupling capacitor at each tap compensates for the reactance induced by tapping the slots off center. The array is backside illuminated through the silicon substrate, so the summing network and other RF components are shielded from incident radiation by the backplane. The coherent interference of signals from the array of slots forms a beam with a width of approximately λ/d where λ is the wavelength in vacuum and d is the size of the antenna array. Our slot antenna arrays are square, with $d \approx 7.2$ mm for 148 GHz devices.

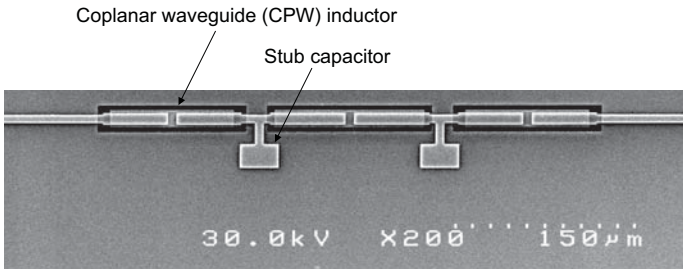

Figure 3.5: The detector passband is defined by a photolithographed 3$^{\text{rd}}$ order Chebyshev LC filter, imaged here by a scanning electron microscope.

Figure 3.6: Long meandered silicon nitride legs suspend but thermally isolate the bolometer island. Thin rails along the outside of the meander make the structure more robust.

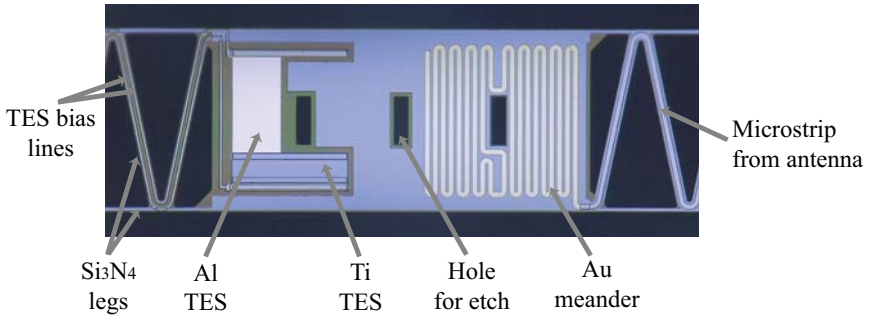

Figure 3.7: Optical micrograph of a bolometer island. Titanium and aluminum TES' on the island are wired in series. The niobium TES bias lines and antenna line run along the low conductivity silicon nitride legs that thermally isolate the island. The island is 375 μm×150 μm. Holes improve the efficiency of the XeF_2 etch which isolates the island during fabrication.

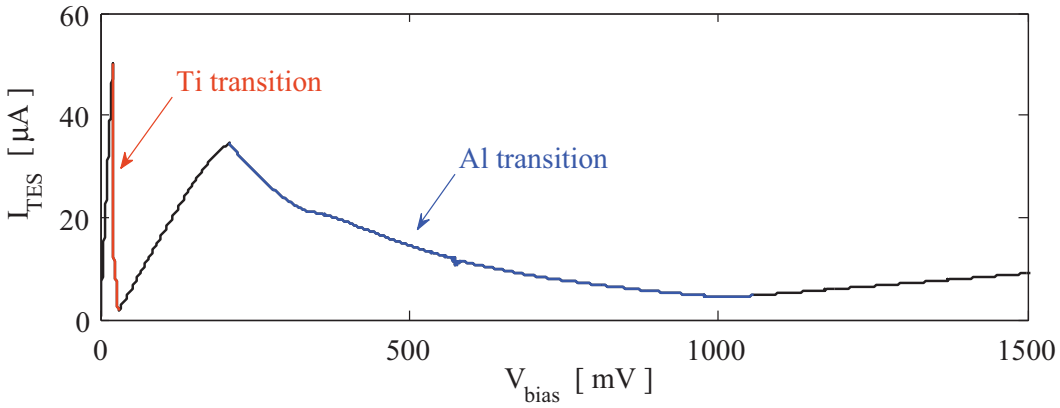

Figure 3.8: I-V curve showing both the Ti TES and Al TES transitions. The TES bias circuit is described in §3.4.

Aluminum has a much higher transition temperature (1.2 K in bulk or about 1.3–1.4 K for our films), so it is reliably deep within its superconducting region under flight conditions, and thus does not impact science mode operation. Under room temperature loading the Ti TES is normal. However, a bias current can be selected to put the aluminum TES on its transition, enabling effective bolometer operation. The Al TES' are designed to have normal resistances more than ten times larger than the those of the Ti TES' so that the parasitic resistance from the normal state Ti will not grossly impair their operation. The measured properties of the aluminum TES in engineering grade tiles are tabulated in Appendix B.1.

3.3 Fabrication Process

SPIDER's antenna coupled TES bolometers are fabricated in the Microdevices Laboratory (MDL) at NASA's Jet Propulsion Laboratory (JPL) by Anthony (Tony) D. Turner and Joseph (Tony) A. Bonetti. The fabrication process for each tile takes 7–8 working days and is described in Bonetti et al. [18, 19]. A Canon FPA-3000 EX3 stepper mask aligner simplifies lithography by quickly patterning features that repeat across the tile. There are 128 TES bolometers on each 148 GHz tile. Each step of the fabrication process is completed for all devices on the tile before proceeding to the next fabrication step.

Fabrication begins with the growth of a 1 micron thick layer of silicon nitride (Si_3N_4) on a 4 inch diameter silicon substrate. Wafers for SPIDER are purchased with the nitride layer already grown. The legs which thermally isolate the TES island are patterned from this nitride.

Aluminum is deposited by electron beam evaporation and patterned by liftoff to form the Al TES. After cleaning the wafer, an insulating silicon dioxide (SiO_2) layer is deposited by RF sputtering to protect the aluminum. To provide electrical access to the aluminum, small holes (vias) are etched into the SiO_2 using inductively coupled plasma reactive ion etching (ICP) with a CHF_3/O_2 plasma.

After stripping the remaining photoresist and cleaning the wafer, the sample is lightly ion milled to clean the Al surface. Then, without breaking vacuum, titanium is deposited using a 6-inch diameter RF sputtering gun. Testing has shown that this gun size is necessary to ensure the requisite thickness uniformity (and with it T_c and R_n uniformity). Prior to 2007, Ti was sputtered using a smaller gun. Then, Ti thickness varied by approximately

30% from the center to the edge of the wafer, resulting in comparable variation in R_n, and about 2% variation in T_c. With the 6 inch gun we achieve thickness and R_n variation of about 10%, and T_c variation of about 0.5%–1% (see §4.6). The titanium TES is patterned using an ICP etch with CCl_2F_2(Freon-12)/O_2. The wafer is immediately cleaned to wash away any chlorine residue. At this point the dual TES is complete. A second layer of SiO_2 is added as a precaution to protect the TES'.

After ion milling to clean the Al at the base of the vias, the niobium ground plane and vias are deposited by RF sputtering and patterned by liftoff. Liftoff is not generally used for such large patterning, but plasma etch processes were found to produce unacceptable variation in titanium TES parameters (especially R_n uniformity).

The SiO_2 interlayer dielectric (ILD) separates the ground plane from the wiring layer. It is deposited by biased RF sputtering in two layers with a polishing and ultrasound cleaning step in between, because an unacceptable number of pinhole shorts were found to occur when the SiO_2 was deposited in a single layer. The thickness of the first layer is measured using a Nanospec spectroscopic reflectometer, with the second deposition time calibrated accordingly. This improves the accuracy and reproducibility of ILD thickness, which determines the capacitance of the band-defining LC filters and thereby the frequency band edges of the antenna.

To make electrical contact to the dual TES, vias are etched through the ILD using CHF_3/O_2. The gold dissipative termination resistor is then deposited by electron beam evaporation and patterned by liftoff. Finally, after ion milling to clean electrical contacts, niobium is deposited by RF sputtering and patterned by liftoff to form the coupling capacitors of the antenna, the summing microstrip, the LC filter, the connections to the TES, and the DC wiring bus. The thinest microstrips are 1 μm wide (Figure 3.9). At this point the antenna-coupled TES is electrically complete, and all that remains is to thermally isolate the bolometer (see Figure 3.10).

The bolometer is thermally isolated from the bulk substrate in three steps. First, the silicon dioxide and silicon nitride around the TES are removed with an ICP etch using CHF_3 plasma, leaving only the thin legs that will physically support the island and wiring connections. At this point, gold is deposited by electron beam evaporation and patterned by liftoff in to several bars around the outside edge of the tile. The silicon nitride is etched out of these areas prior to the ILD deposition, so that the gold makes direct contact with

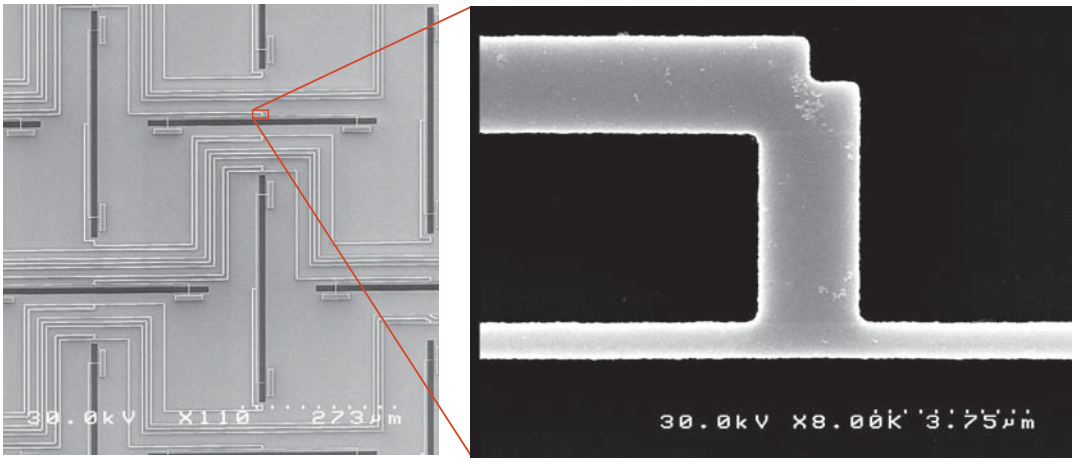

Figure 3.9: *Left*: A portion of an antenna and niobium microstrip summing tree. *Right*: A branching of the microstrip summing tree. The narrowest sections of microstrip summing tree are 1 µm in width (shown here at bottom). Scanning electron microstrip images.

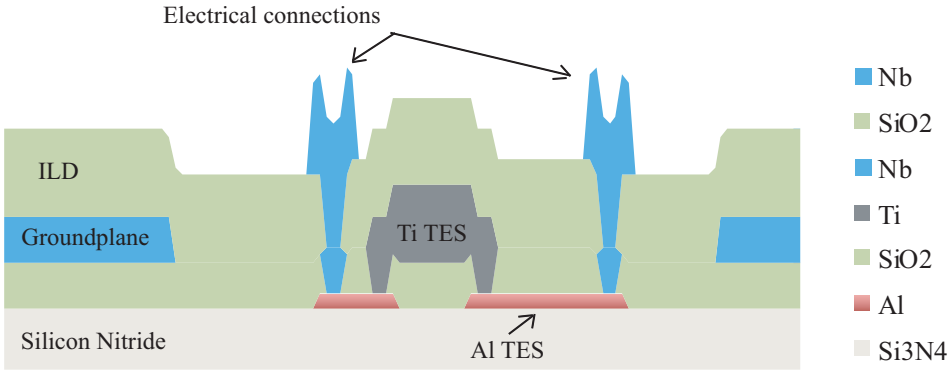

Figure 3.10: Schematic of a localized cross section showing the layered construction of the Al and Ti dual-TES with the SiO_2 protection layer, niobium groundplane, SiO_2 interlayer dielectric (ILD), and niobium wiring connections. The device shown here has not yet been released (thermally isolated).

the bare silicon. The completed tile will be heat sunk to the focal plane unit through gold wire bonds from this gold "picture frame."

The second step in releasing the bolometer islands is an etch with a deep trench etcher using a thick layer of patterned photoresist. This etch makes deep holes around the bolometer island and also cuts the wafer into a 7.3 cm square. The deep trench etcher etches deep, narrow vertical holes, so the wafer is then exposed to XeF_2 gas to undercut and complete the release (thermal isolation) of the island. Extra holes in the interior of the island aid the undercutting (see Figure 3.7). Removing the photoresist and cleaning then complete the tile fabrication. Extensive electrical checks are performed at JPL to locate wiring bus and antenna shorts to the ground plane. Any device with a TES bias line short to ground is not electrically connected when the tile is mounted on the focal plane.

3.4 TES Bolometer Basics

Thermal Circuit

A bolometer consists fundamentally of a radiation absorber and a temperature-sensitive resistor (thermistor) on a structure weakly thermally coupled by supporting legs to a heat sink of constant temperature. Small changes in the incident radiation heat and cool the island, and these change in heating power are measured by the thermistor. This simple thermal system is illustrated in Figure 3.11a. The system is in equilibrium when the sum of the absorbed optical power (Q) and the Joule power dissipated by the resistor (P_{Joule}) is equal to the heat transfer to the heat sink (P_{legs}),

$$Q + P_{Joule} = P_{legs} \qquad \text{[equilibrium condition]} \; . \tag{3.1}$$

The cooling power of the legs is modeled as a power law function of the island temperature (T_{TES}) and the heat sink substrate temperature (T_{sub}),

$$P_{legs} = K \left(T_{TES}^{n} - T_{sub}^{n} \right) . \tag{3.2}$$

We use the alternate parameterization

$$P_{legs} = \frac{GT_0}{\beta+1}\left[\left(\frac{T_{TES}}{T_0}\right)^{\beta+1} - \left(\frac{T_{sub}}{T_0}\right)^{\beta+1}\right], \tag{3.3}$$

where the value of G depends on T_0, which is a free parameter chosen to reflect the temperature scales of interest. This is a convenient because the derivatives take the simple forms

$$\frac{dP_{legs}}{dT_{sub}} = G\left(\frac{T_{sub}}{T_0}\right)^{\beta} \quad \text{and} \quad \frac{dP_{legs}}{dT_{TES}} = G\left(\frac{T_{TES}}{T_0}\right)^{\beta}. \tag{3.4}$$

It is often convenient to choose $T_0 = T_c$, where T_c is the transition temperature of the superconductor. In this context the exact definition of T_c is unimportant because the transition occurs over a very narrow temperature range. With this selection, when the TES is in its transition ($T_{TES} \simeq T_c$) we have

$$\frac{dP_{legs}}{dT_{TES}} = G_c, \tag{3.5}$$

and

$$P_{legs} = \frac{G_c T_c}{\beta+1}\left[1 - \left(\frac{T_{sub}}{T_c}\right)^{\beta+1}\right]. \tag{3.6}$$

When specifically studying the properties of fabricated legs, it is convenient to quote a value of G that is independent of T_c (a property of the TES, not the legs). For historical reasons we often choose $T_0 = 450$ mK, so

$$P_{legs} = \frac{(G_{450})(450\text{ mK})}{\beta+1}\left[\left(\frac{T_{TES}}{450\text{ mK}}\right)^{\beta+1} - \left(\frac{T_{sub}}{450\text{ mK}}\right)^{\beta+1}\right]. \tag{3.7}$$

The variable G_{450} characterizes the magnitude of the thermal conductance while β describes the strength of the power law. Both parameters depend on the geometry and material makeup of the structures that comprise the supporting legs.

SPIDER's antenna-coupled bolometers are not designed to absorb radiation directly on the bolometer island. Instead, radiation is absorbed by a coherent slot antenna array and then that power (Q) is dissipated by a resistor on the island. This distinction does not notably effect the operation of the bolometer. The slot antenna array is described in more detail in §3.2.

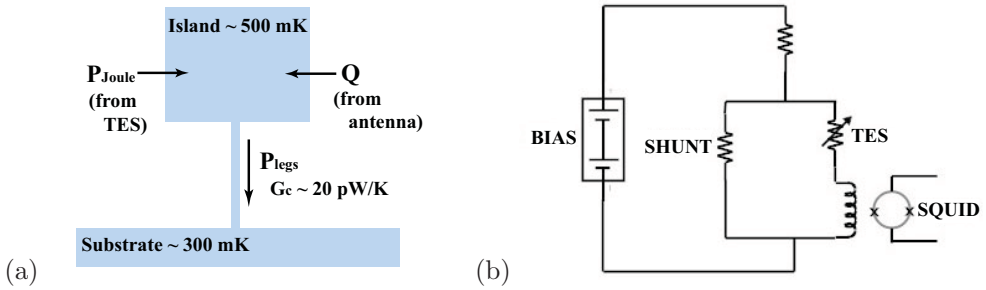

Figure 3.11: (a) The TES thermal circuit. Antenna power and Joule power from the TES heat the bolometer island which is weakly thermally coupled to a cold substrate. (b) The TES electrical circuit. A small shunt resistor (3 mΩ) is placed in parallel with the TES (variable, ∼20–30 mΩ) to establish a voltage bias. The TES branch is inductively coupled to the SQUID readout.

SPIDER uses Transition Edge Sensors (TES') as thermistors. The Joule power dissipated on the bolometer island by the TES is given by

$$P_{Joule} = I_{TES}^2 R_{TES} = \frac{V_{TES}^2}{R_{TES}}. \tag{3.8}$$

Inductive coupling of the TES branch to a current sensing SQUID permits the measurement of I_{TES} from which we can calculate R_{TES} and P_{Joule}, as explained in the following section.

Electrical Circuit

The bolometer electrical circuit is shown in Figure 3.11b. The bias voltage V_{bias} is the only dynamically adjustable user input. In normal operation, this bias voltage is fixed to a value chosen such that the heat dissipation P_{Joule} drives the TES bolometer into its transition. The resistances of the series resistor (hundreds of ohms) and parallel shunt resistor (3 mΩ) are known. The normal state resistance of the TES is about ten times that of the shunt resistor. For optimal stability and performance, bias voltages are selected such that the resistance of the TES is $\gtrsim$60% of its normal state resistance. Therefore in standard operation, most of the bias current flows through the shunt resistor branch of the circuit, establishing a fixed voltage bias across the TES.

The only property of the circuit that is dynamically measured is the current through the TES branch of the circuit. This is measured by inductive coupling to a multiplexed Superconducting Quantum Interference Device (SQUID) system, described in §3.5. The

measured current is used to calculate the resistance of the TES, given by

$$R_{TES} = R_{shunt}\left(\frac{V_{bias}}{R_{series}I_{TES}} - 1\right), \tag{3.9}$$

as well as the voltage across the TES, given by

$$V_{TES} = R_{shunt}\left(\frac{V_{bias}}{R_{series}} - I_{TES}\right). \tag{3.10}$$

Let us examine the properties of a TES transition. First we apply a large V_{bias} sufficient to saturate the TES in its normal state. If the device is superconducting, there will be no Joule power dissipation, and it will remain in the superconducting state. We pulse the heaters on the detector tiles for 1 s to drive the devices normal. After the tile temperatures settle, we record data while incrementally decreasing the bias through the transition to the superconducting state (using the *ramp_tes_bias* command while in *data_mode* 10). In examining this data, we frequently plot the I-V curve. An example is shown in the top left of Figure 3.12. The superconducting, transition, and normal regions are clearly visible. To see what V_{bias} values will put the TES into its transition, we plot R_{TES} (top right of figure).

To relate back to the power equations which govern the thermal evolution of the system, we calculate the power dissipated by the TES, P_{Joule}. Plotting this power against R_{TES} (lower left of figure), we see that P_{Joule} plateaus while the TES is on transition. This is no surprise given the equilibrium thermal condition (Equation 3.1), as we are not changing the optical load Q, and the cooling provided by the legs is nearly constant because T_{TES} changes very little as the TES passes through its transition. The power level of this plateau is the saturation power (P_{sat}). This is the amount of Joule power that must be dissipated by the TES itself to keep the TES in its transition. The addition of power (e.g., optical power) in excess of P_{sat} would drive the device off of the superconducting transition and in to the normal state. Measuring P_{sat} at a variety of different substrate temperatures T_{sub} with constant optical power Q enables fitting for the conductance properties of the Si_3N_4 legs, parameterized by G_{450} and β (Equation 3.7). For a dark measurement ($Q = 0$), the $P_{Joule} = 0$ corresponds to the TES transition temperature T_c.

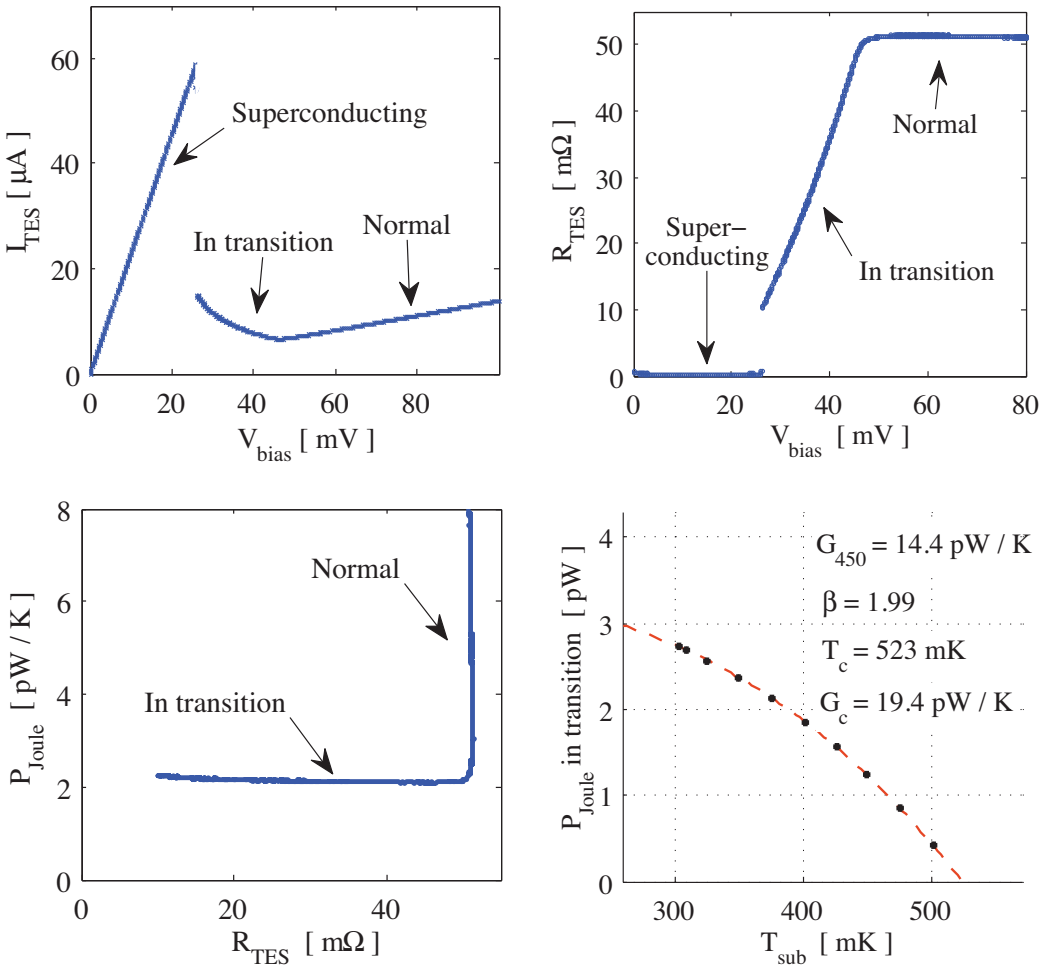

Figure 3.12: *Top left*: An example of a measured I-V curve. When the TES passes through the low end of its transition, it becomes unstable and the SQUID system loses lock, introducing an arbitrary offset in the data. We correct for this by forcing the projection of the normal branch to intersect the origin. *Top right*: The calculated R-V curve, which is useful in selecting a bias voltage. *Bottom left*: The Joule power dissipated by the TES as a function of TES resistance. The Joule power is nearly constant while the TES is on transition assuming the optical power Q is stable. *Bottom right*: The TES Joule power on transition of our example device at ten different substrate temperatures with $Q = 0$. Curve fitting gives G, β, and T_c.

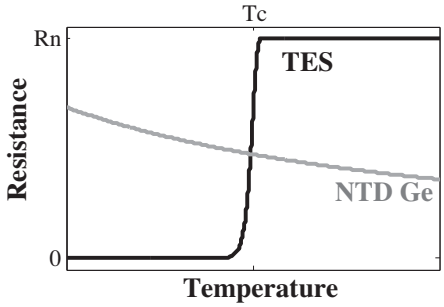

Figure 3.13: Comparison of TES (superconductor) and NTD Ge (semiconductor) thermistor response functions.

Electrothermal Feedback

Earlier generations of bolometers utilized neutron transmutation doped (NTD) germanium semiconductor thermistors. Transition edge sensor (TES) bolometers replace these semiconductor thermistors with superconductor thermistors. As shown in Figure 3.13, TES thermistors have a much steeper response function but a smaller operational range than NTD thermistors. Clearly, superconducting thermistors only exhibit significant response to temperature changes in the narrow transition between their superconducting ($R_{TES} = 0$) and normal ($R_{TES} = R_n$) states. SPIDER's bolometers are maintained at a temperature within their transition by voltage biasing to take advantage of negative electrothermal feedback. This application of feedback was proposed by Kent Irwin [63], and this section follows Irwin and Hilton's seminal review paper [64].

The resistance of a TES is sensitive to temperature (T_{TES}) and current (I_{TES}).

$$\alpha_I(R_{TES}) = \frac{T_{TES}}{R_{TES}} \left.\frac{\partial R_{TES}}{\partial T_{TES}}\right|_{I_{TES}} \tag{3.11}$$

$$\beta_I(R_{TES}) = \frac{I_{TES}}{R_{TES}} \left.\frac{\partial R_{TES}}{\partial I_{TES}}\right|_{T_{TES}} \tag{3.12}$$

When a small change in optical loading δQ perturbs the temperature of the TES ($T_{TES} = T_c + \delta T$), a change in resistance is produced ($R_{TES} = R_0 + \delta R$). Using linear approximations,

$$\begin{aligned} C\frac{d(\delta T)}{dt} &= P_{Joule} - P_{legs} + Q \\ &= (P_{Joule,0} - P_{legs,0} + Q_0) + \left(\frac{dP_{Joule}}{dR_{TES}}\right)\delta R - \left(\frac{dP_{legs}}{dT_{TES}}\right)\delta T + \delta Q \\ &= 0 + \left(\frac{dP_{Joule}}{dR_{TES}}\right)\left(\frac{\alpha_I R_0}{T_c}\delta T\right) - G_c\delta T + \delta Q \\ &= -\left[-\frac{\alpha_I R_0}{T_c}\left(\frac{dP_{Joule}}{dR_{TES}}\right) + G_c\right]\delta T + \delta Q. \end{aligned} \tag{3.13}$$

For superconducting thermistors α_I is positive. The derivative dP_{Joule}/dR_{TES} is negative in a voltage-biased configuration (constant V_{TES}) and positive in a current-biased configuration (constant I_{TES}). We select a voltage bias configuration (Figure 3.11b, and discussed in the previous section) to achieve negative electrothermal feedback, so

$$C\frac{d(\delta T)}{dt} = -(\mathcal{L}+1)G_c\delta T + \delta Q, \tag{3.14}$$

where the loop gain

$$\mathcal{L} \equiv \frac{P_{Joule}\alpha_I}{T_c G_c}. \tag{3.15}$$

Both the changing Joule dissipation and the cooling power of the legs act to restore the temperature of the TES to equilibrium. Superconducting thermistors are thus easily biased into stable equilibrium in their transitions. For SPIDER, $\mathcal{L} \gg 1$ so for transient response the removal of Joule power dominates over cooling through the legs. Electrothermal feedback improves linearity and makes the bolometers much faster than the natural thermal time constant (C/g). This increase in speed relative to NTD bolometers enables time multiplexed readout.

3.5 Readout

SPIDER's TES bolometers are coupled to a cryogenic time domain multiplexed three-stage Superconducting Quantum Interference Device (SQUID) amplifier system developed and fabricated by the National Institute of Standards and Technology (NIST). This technology is described in detail elsewhere [28, 35, 64], so I will only provide a summary here.

The signal from each TES is wired to a Nyquist (NYQ) chip. A Nyquist inductor on the chip (2 μH), in series with the TES resistance and the input inductor of the SQUID system, serves as a low-pass L/R filter for SQUID and detector noise. The unavoidable sampling rate limitations inherent in time domain multiplexing cause high-frequency noise to be aliased in to the science band. Increasing the inductance of the Nyquist filter reduces the aliasing of high-frequency noise but slows the multiplexer settling time and makes the TES circuit more susceptible to instability (electrothermal oscillation). The low thermal conductance (G) of SPIDER's bolometer legs reduces thermal time constants and makes the devices less prone to instability than sister experiments designed for ground operation

(BICEP2, Keck).

Each NYQ chip provides Nyquist inductors and shunt resistors for 32 independent detector channels. Wire bonds bridge the signals from the NYQ chips to SQUID multiplexer (MUX) chips. The filtered signal from each detector channel is inductively coupled to a first stage SQUID ammeter (SQ1) on the MUX chip. There are 33 SQ1s on each MUX chip; 32 couple to detectors, and one (the "dark SQUID") is used to monitor drifts and magnetic pickup in the SQUID amplifier system. The outputs of the 33 SQ1s are added in a summing coil that is coupled to a second stage SQUID (SQ2), also located on the MUX chip. The SQ1s are biased sequentially in rapid succession, so the SQ2 couples to a single channel at a time (time multiplexing). The SQ2 output is routed to a SQUID series array (SSA), where it is amplified by 100 SQUIDs in series.

Each set of 33 channels is called a mux column. Two adjacent physical columns of pixels on a tile share each mux column, so there are four mux columns for each 148 GHz detector tile (128 TES). All of the channels in a mux column share a single common TES V_{bias}, but each column may be biased independently. There are four detector tiles in each focal plane unit (FPU), coupling to sixteen MUX and NYQ chips. Mux columns are numbered 0 to 15. There are two SSAs per FPU, each serving eight mux columns. The 33 channels in each column are called mux rows (numbered 0 to 32). Row 0 is the dark SQUID. The two polarizations (A and B) of each spatial pixel are read out on consecutive rows (by physically adjacent SQ1s). The lines which bias the SQ1s (known as "row selects") activate the same row simultaneously for all of the columns. Because the SQ1s for all mux columns within a mux row share a common bias, they are prescreened at 4 K to ensure adequate critical current uniformity within an FPU.

The MUX and NYQ chips are cooled to 300 mK. In the original RevX design, the SSA was also at 300 mK. Large resonances in the SSA introduced significant noise in the readout. The SSA is now set off from the 4 K stage and SSA resonances are no longer a significant concern.

The entire TES and SQUID system for each FPU is controlled and readout by a single ambient-temperature Multi-Channel Electronics (MCE) crate developed by the University of British Columbia (UBC) [10, 9, 121]. A crystal clock (Sync Box) synchronizes the MCEs for the six Spider telescope inserts. The fundamental clock rate is 50 MHz. Each MCE has an Address Card, which switches the SQ1 biases on and off, shifting between rows after

a number of clock cycles given by *row_len*. We generally choose a value of *row_len* in the range 80–100 (exact value selected to optimize noise performance), so each of the 33 rows is biased on for ∼1.5–2 µs with a revisit rate of ∼15–20 kHz. Because the system must settle after each switch, only the sum of the data from the last $num\_samples = 10$ clock ticks is acquired. The data is currently filtered and down sampled with $data\_rate = 38$ cycles per data packet, so data packets are written to disk at ∼400–500 Hz. This *data_rate* was selected for an Alice Springs flight, and will probably be increased to about 120 due to the slower scanning speed planned for the McMurdo flight. Two Readout Cards in each MCE handle the readout and feedback of the SSAs. Bias Cards provide the low noise DC biases to the SQUID system and to the TES'. The MCE Clock Card controls all of the other cards, assembles the data frames, and communicates with the outside world. Each MCE is connected via an optical fiber to a computer that acquires the data and that can be used to dynamically reconfigure the readout system.

Chapter 4

Receiver Performance

In the preceeding chapters I have introduced SPIDER's science goals, design principles, detector technology and hardware. In this chapter I discuss the measured performance of engineering grade SPIDER detectors and receivers. Most of this work has been performed at Caltech. The SPIDER, BICEP2, and KECK instruments utilize nearly identical optical designs, detectors, and readout technologies. Synergy between these instrument collaborations has greatly accelerated progress toward shared technology goals. Early detector development efforts centered around test beds capable of characterizing just one or two devices at a time. I joined this effort in June 2007, performing optical characterization of individual devices in a windowed cryogenic test bed. Notes about my measurements can be found in the *White Dewar Logbook* [118]. SPIDER's modular design enables individual testing of its six flight receivers in the SPIDER test cryostat. In February 2009 the Caltech SPIDER team began characterization of full focal planes of detectors coupled through flightlike optics. Details regarding our measurements and results can be found in in the *Spider Analysis Logbook* [114]. In this chapter I examine, one by one, important characteristics that will dictate the flight performance of SPIDER's receivers. I conclude the chapter with a summary of the currently achieved performance of 148 GHz receivers and my recommendations for future work (Table 4.4, §4.10).

4.1 Beam Profiles

The CMB B-mode signal is much smaller than both the temperature anisotropy and the E-mode signal. Beam mismatch and imperfect beam characterization can lead to a mixing of temperature and polarization signals, producing a false B-mode signal. Accurate beam

characterization and tight control of systematic beam effects is required to make high-fidelity polarization maps. We can geometrically decompose the difference between the beams of the two orthogonally polarized detectors for any pixel. The leading terms are the mismatch in beam width, center, and ellipticity. These and other useful figures of merit characterizing systematic errors are defined by Takahashi et al. [116].

Far-field Measurements

SPIDER's small apertures enable preflight far field characterization of the lens-coupled beams ($D^2/\lambda = 30$ m at 148 GHz). The University of Toronto has recently completed construction of a telescope mount capable of scanning the SPIDER test cryostat in azimuth and elevation. Prior to its availability, we performed some preliminary beam characterization using a chopped blackbody source (10.8 cm aperture) on a simple linear stage with a 1.4 m throw distance. The SPIDER test cryostat was oriented nearly horizontally to view the source down a hallway at an aperture-to-aperture distance of 29.4 m. With the source centered on the beam, the linear stage could be manually rotated to measure the beam pattern along slices at different boresight angles. We sampled only two pixels because the experiment setup and alignment for each pixel is very time intensive and because cryogenic limitations on the orientation of the cryostat do not allow access to the full focal plane.

Scanning across a beam, the amplitude of the chopped signal was much larger than the change in the DC offset, indicating that the two-fin blade effectively chopped the source. The position of the source was not encoded, but measurements made using forward- and backward-going scans were indistinguishable, suggesting that the stage maintained a consistent scan rate ($\sim$0.5 cm/s) during each scan. The signal was very clear above the noise. We recovered the beam pattern by demodulating the data using a narrow (0.7 Hz wide) filter around the modulation frequency ($\sim$18 Hz). Jeff Filippini has led the analysis of SPIDER beam maps.

Beam slices taken at a single declination angle are plotted for four detectors in Figure 4.1. The measured beam slices can be well approximated by Gaussian fits, with a slight decrement visible in log scale plots near the edges of the beam (>30 arcmin from the beam center). The blackbody source was circular in shape, with an apparent diameter of 12.6 arcmin from the cryostat. This is comparable to the beam size, and augments the apparent beam width by about 3%. Deconvolving the beam and source, a beam slice fit by

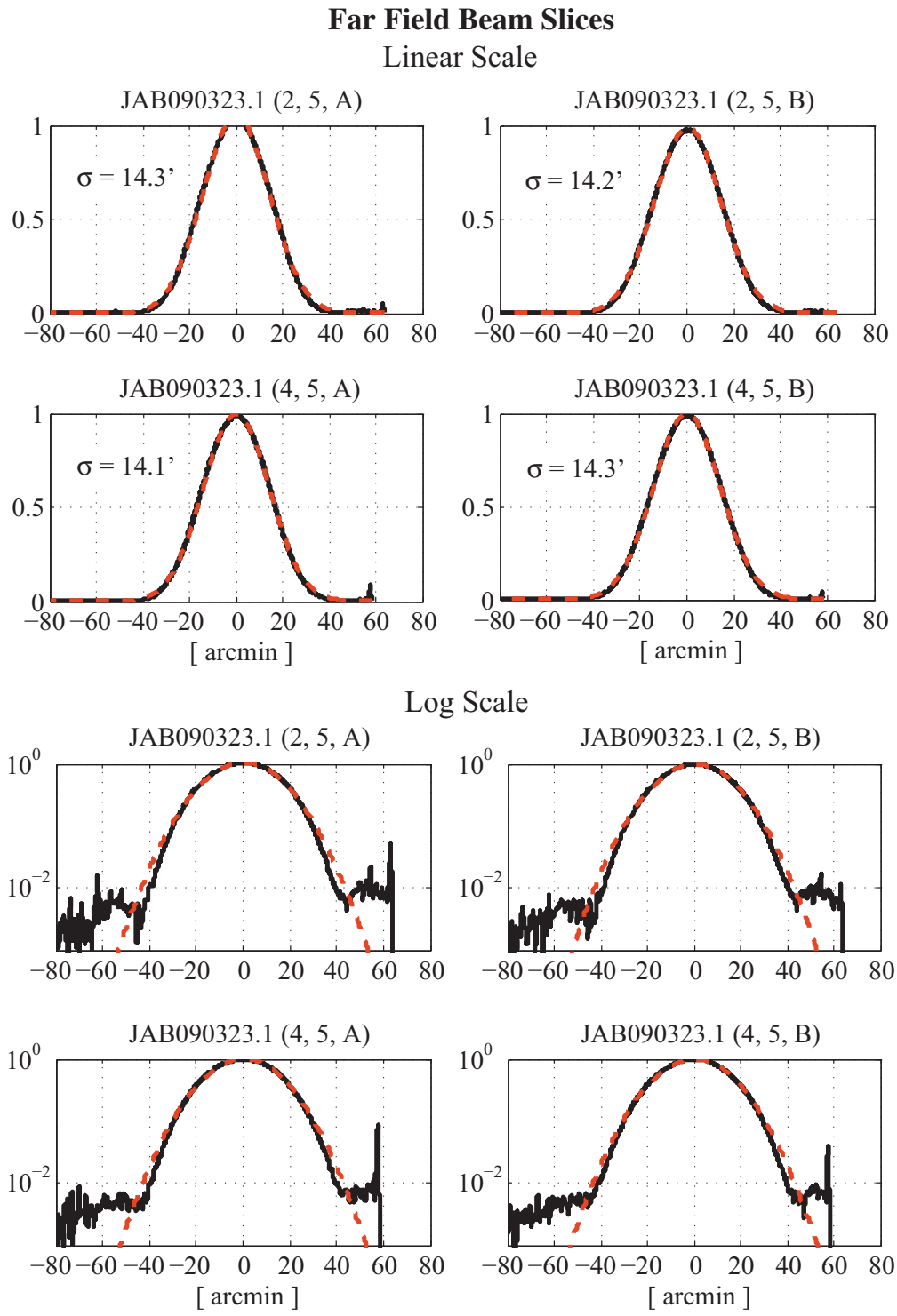

Figure 4.1: Far field beam slices (black) for two pixels showing detectors of both polarizations (A and B) in linear and log scales along with Gaussian fits (red dashed). Plots credit: J. Filippini.

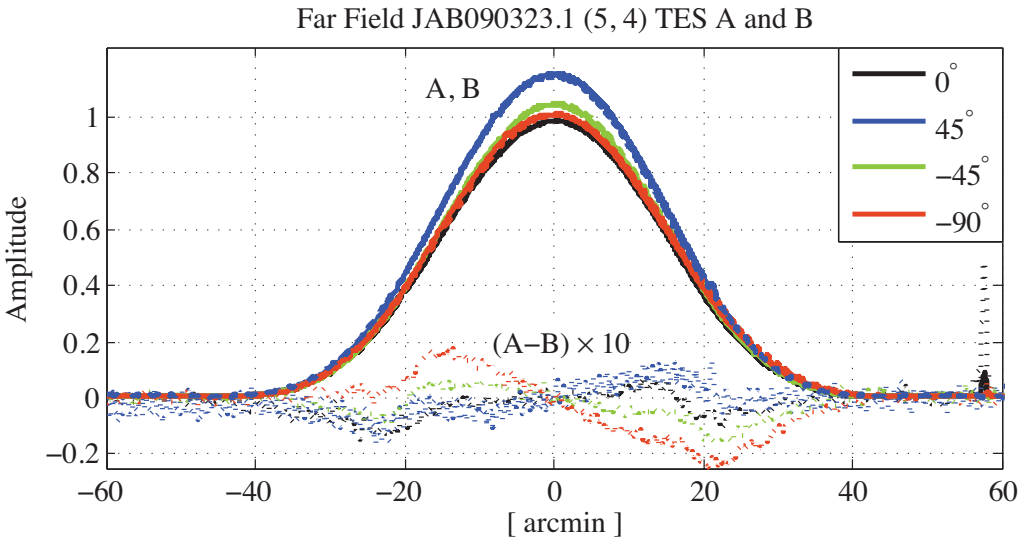

Figure 4.2: Difference between the beams of the A and B polarization detectors for a single pixel. Linear scans were taken at four stage angles. The profiles have been normalized to peak at unity for the 0°-oriented scan. An A/B pointing offset is clearly visible. The cross section of the offset changes sign and amplitude along different scan directions. Figure credit: J. Filippini.

a Gaussian with $\sigma = 14.2$' would result from a true beam width of $\sigma = 14.6$' (34' FWHM).

Each physical pixel on the focal plane is monitored by two detectors ("A" and "B") coupled to orthogonal antennas. Differencing the normalized beams of the two polarized detectors of each pixel, we find an offset in their beam centers (Figure 4.2). For the tested pixel, the offset between the fit beam centers of the A and B detectors varies from 0.05'–0.35' between scans along four different axes (differing by 45°). The measured offset of 0.35' is 2.4% of σ (the beam size), or, alternately, 1% of the beam full width half maximum (FWHM).

BICEP2, our sister experiment on the ground, has characterized far field beam properties over their entire focal plane [2]. They measure differential pointing $|\mathbf{r}_A - \mathbf{r}_B|/\sigma = 10\%$ (mean) $\pm 4\%$ (measured standard deviation across focal plane) and differential beam width $|\sigma_A - \sigma_B|/\sigma = 0.3\% \pm 0.2\%$. For beam ellipticity they find $e = (\sigma_{maj} - \sigma_{min})/\sigma = 3\% \pm 3\%$ and, for differential ellipticity, $|e_A - e_B|/2 = 1.2\% \pm 9\%$. The large variation in measured differential ellipticity is believed to be due to beam distortions in some pixels caused by "beam steering," which is most easily studied in the near field.

The relative importance of different systematic beam effects depends on scan strategy,

and thus varies from instrument to instrument. We have used SPIDER's simulation pipeline to characterize the level of the false B-mode signal generated by each of the leading-order beam effects. The observed levels of differential beam width and differential ellipticity generate false B-modes at a level that is negligible relative to SPIDER's $r = 0.03$ noise floor. The simulations suggest that the level of differential pointing measured in BICEP2 (10%) would produce a false B-mode signal at multipole $l = 100$ at the level of 20% of a $r = 0.03$ signal, assuming that the pointing offset does not rotate with the half-wave plate [95].

Our far-field measurement of a single SPIDER pixel suggests that differential pointing might be a factor of a few smaller in SPIDER than in BICEP2. In coming months large-scale beam mapping of entire SPIDER focal planes will confirm or deny this finding. The cause of differential pointing is not well understood. Differential pointing at the level of the antenna is not sufficient to produce differential pointing in the far field of the telescope, but may seed effects generated by a lens or filter. Some preliminary evidence points toward a dielectric filter in BICEP2 (not used in SPIDER). The A/B beam offset in BICEP2 is generally oriented along the axis parallel to the wire bond edge. Roger O'Brient has isolated the dominant cause of this effect at the antenna level. A coupling between the interleaved A and B summing trees rotates the phase of the signals. Simulation and testing have shown that this coupling is most strongly associated with the tree branches that run parallel to the wire bond edge of the tile. Roger has recently redesigned the feed network for the 148 GHz antenna to introduce more space between the most strongly coupled lines. Near field maps of tiles made using this new design exhibit a 2–3× reduction in A/B beam offset, which may translate in to the far field.

Near-field Measurements

Only far field beam properties impact the quality of science data, but near field mapping is a useful tool for diagnosing beam effects. We map beams in the near field of the telescope using a chopped hot blackbody source scanned across the field of view by a computer-controlled two-stage linear actuator. The assembly is clamped to the top of the SPIDER test cryostat, with the source 5" above the the window aperture. Typically, the mapper scans a 15" square grid, translating in steps of 1/4" and then pausing for 5 s. The first second of data at each location is discarded to permit microphonic dissipation. The chopper is operated at 10–15 Hz, taking care to avoid any observed RF pickup frequencies. In our

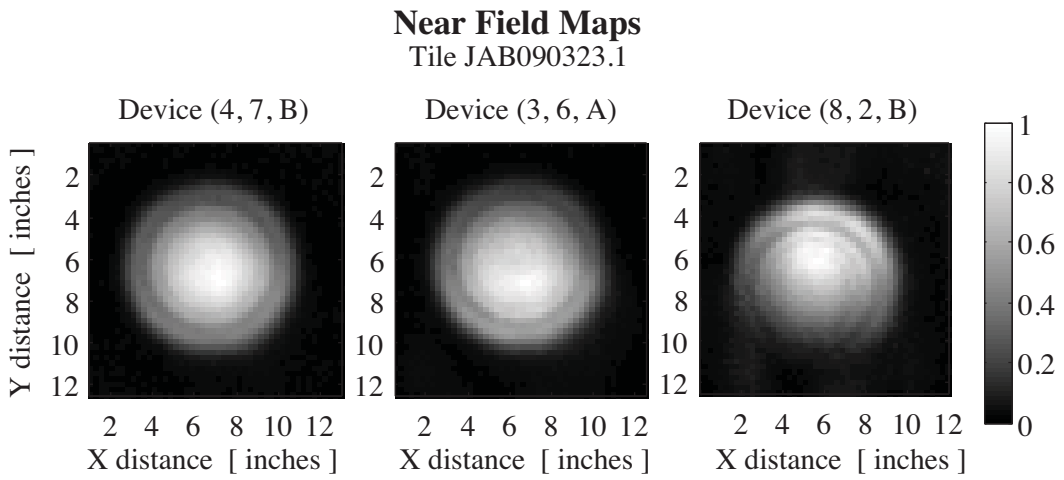

Figure 4.3: Near field maps for three example devices from tile JAB090323.1 in Run 2.1. *Left*: Device with symmetric beam exhibiting very little beam steer. *Center*: Moderate beam steer (not unusual). *Right*: Significant beam steer (an edge pixel, the worst on this tile). Edge devices on bad tiles exhibit even more severe beam steer (not shown). Maps credit: J. Filippini.

measurements, we have found that the change in thermal loading on the detectors as the hot source enclosure scans across the aperture produces an (unchopped) DC variation nearly 10× as large as the chopped signal amplitude. The signal to noise of the chopped signal is good, however.

Near field beam maps for three example devices are plotted in Figure 4.3. We find that beams of the antennas are steered away from the primary axis. The steered beams illuminate the aperture asymmetrically. Asymmetrical truncation of the beam introduces ellipticity and complicated higher-order effects in the far field beams [2]. For most pixels, far field beam mismatch is not dominated by this effect.

Beam steer is generally most significant for pixels on the edge of a tile. The steering is frequently oriented toward the center of the tile. We postulate that a spatial gradient in the index of the interlayer dielectric (ILD) is causing the summing network to add signals out of phase with each other. Power is transmitted through the niobium microstrip summing tree in a quasi-TEM mode [48, 102]. The resulting time-varying fields in the SiO_2 ILD both dissipate power and shift in phase as they propagate through the tree. The phase shift (per unit distance) depends on the index of the dielectric. Signals from all of the antenna slot elements are combined such that they are added in phase assuming that the index of the

dielectric is spatially constant across the device. If the index of the dielectric is not constant, the signals from the slots are not in phase when they are added because the microstrips from different antenna slots pass through distinct physical regions of the device.

Zemax physical optics simulations of a uniform phase gradient across an array exhibit strong qualitative agreement with observed near field maps. Agreement with this model requires a phase gradient of tens of degrees across the antenna of devices exhibiting moderate beam steer (Figure 4.3). Significant beam steer may be produced by phase gradients of a couple hundred degrees. A phase gradient of 180° across a pixel could be produced by an index variation of ∼0.1 (5%) [2].

We use specially designed test devices to measure variations in the index of the ILD [75]. A shared single polarization slot antenna is coupled by niobium microstrips to two TES' through a 3 dB power divider. The microstrips coupling the antenna power to the two TES' are identically 3 μm wide. One of them is interrupted by a section 8 μm wide and 4 mm long. This section acts as a resonant cavity. The ratio of the signals at the two TES exhibits prominent fringes in the frequency domain. The fringe spacing is directly proportional to the phase velocity in the wide microstrip section. Average beam steer amplitude varies significantly between tiles. Measurements of several test tiles show a strong correlation between the strength of the observed beam steer effect and the measured degree of index variation for the tile. The current practice is to discard tiles which exhibit exceptionally large beam steer. No direct solutions are presently being pursued to reduce index variation in fabricated tiles.

Antenna Beams Decoupled from Optics

The slot antenna array is square (Figure 3.3, *right*). It is about 7.2 mm on a side for 148 GHz devices, and scales linearly with wavelength so that beam width is the same for all bands. In the far field of the antenna ($D^2/\lambda \approx 2.5$ cm), the beam should be approximately a square *sinc* function (the Fourier transform of a uniformly illuminated square). Near the beam center, it can be well approximated by a Gaussian.

I have characterized antenna beams independently of the SPIDER optical system in a test dewar known as the "White Dewar." A single pixel can be optically coupled to the lab environment through a window in this helium-cooled Janis dewar. The pixel is varnished (at the corners) on to a silicon support substrate. The simple gold-plated copper mounting

box bolts to a stage cooled to ∼300 mK by a ^{3}He-^{3}He-^{4}He fridge and temperature controlled using a PID loop. The pixel views the window through the silicon mounting substrate with a $\lambda/4$ fused silica AR coating. An Eccosorb[1] LS-26/SS-3 absorber covers the backplane of the mounting box. There are no lenses in the system. An AR-coated 0.5 mm thick fluorogold filter is mounted on the inner 4 K shield (niobium). AR-coated teflon filters (14 mm and 19 mm thick) are mounted on the outer 4 K shield (aluminum) and the nitrogen-cooled 77 K shield. A Zotefoam[2] window seals the 300 K vacuum vessel. This window is the limiting aperture (60° field of view, with a misalignment of ∼5°).

The beams are mapped using a chopped source raster scanned over a blackened planar surface by two linear stages. A commercial SQUID system reads out the TES bolometers, which are wired in the usual voltage-biased configuration. The measured beams are in agreement with the beam model. The main beam is symmetrical, with a width $\sigma = 6.5°$ (15° FWHM), and beam width is well matched between A and B polarizations on a pixel (Figure 4.4). The four primary sidelobes appear at −13 dB about 24° from the beam center, as predicted by the model (Figure 4.5). In SPIDER, these sidelobes are terminated on the 1.8 K aperture stop.

Roger O'Brient has recently designed a new summing tree that sums the elements of the antenna array with a Gaussian taper. This should reduce the amplitude of the sidelobes and couple more power in to the main beam. Results from preliminary testing in the "Short Keck" dewar show a significant conversion of sidelobe response into main beam response (Figure 4.6). Short Keck is a new test bed that enables simultaneous beam mapping of detectors on entire FPU in the far field of the antennas, with no lenses and an aperture large enough to view the primary sidelobes.

[1] http://www.eccosorb.com/
[2] http://www.zotefoams.com/

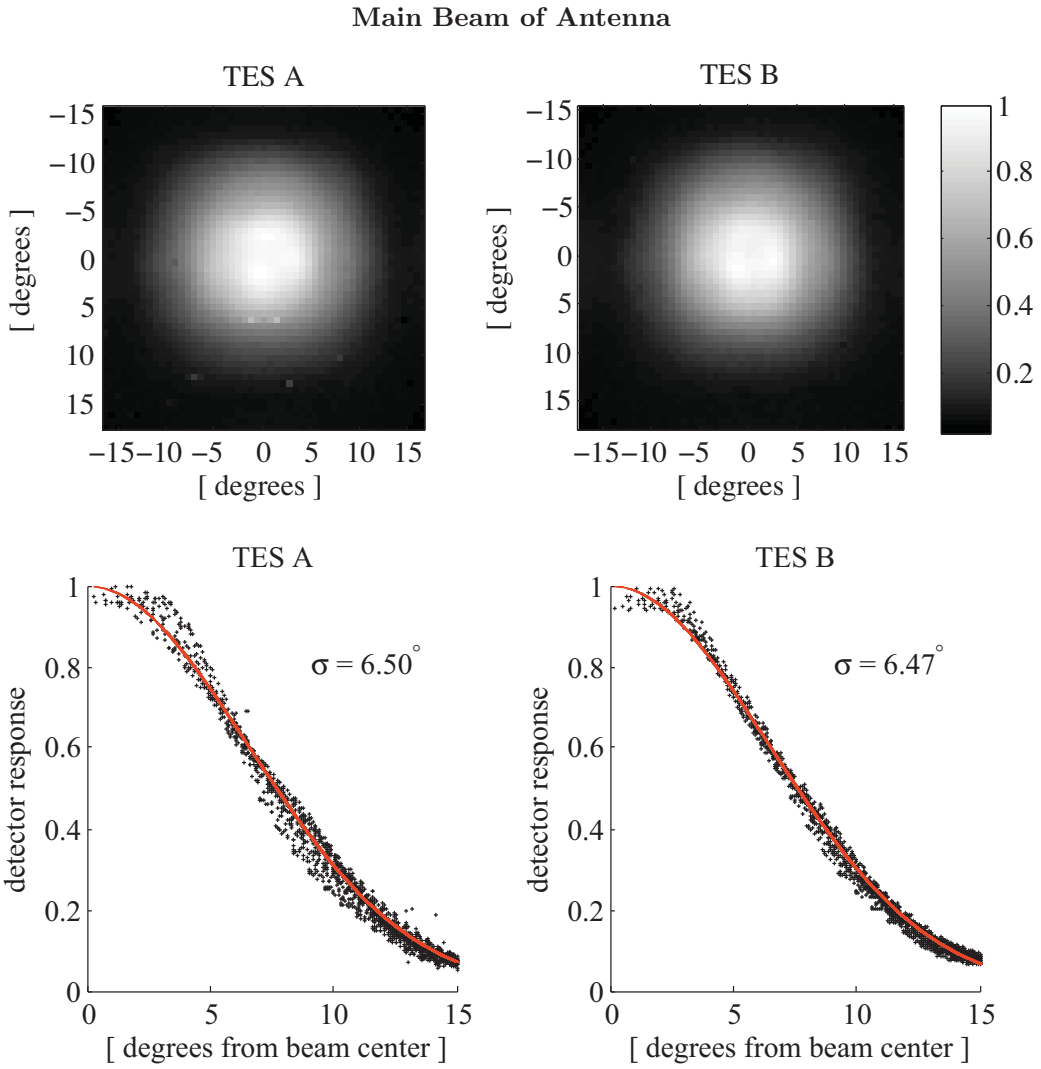

Figure 4.4: *Top*: Antenna far field beam patterns of both polarizations (A and B) for a single 145 GHz test pixel. This is the measured response in the far field of the antenna, with filters but no lenses in the optical path. The designation of this test pixel is JAB080312.2 (2, 4). *Bottom*: Azimuthally collapsed profiles of the beams, shown with Gaussian fits.

Primary Side Lobes of Antenna

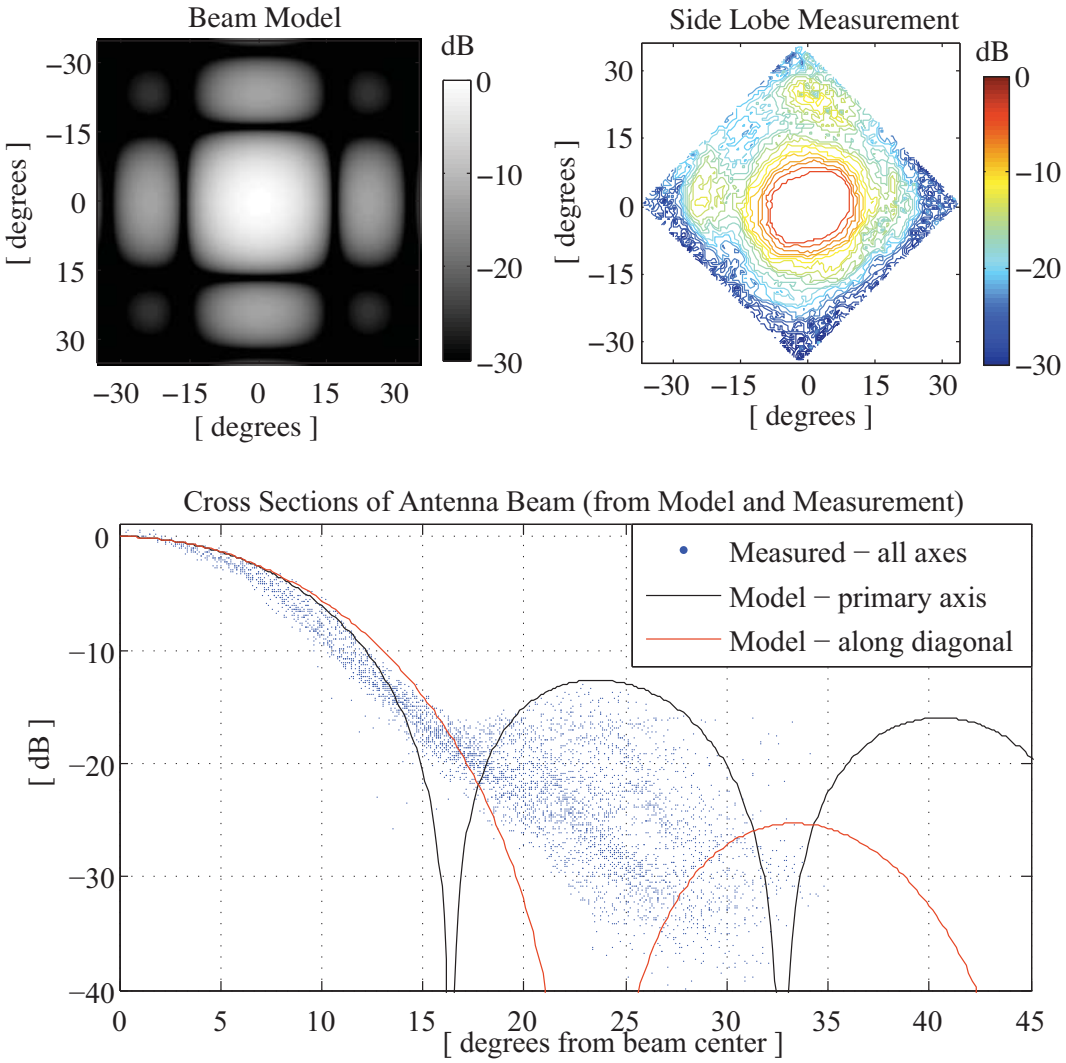

Figure 4.5: *Top left*: Model of the far field beam pattern of an antenna (before coupling through the telescope), shown in log scale to emphasize side lobes. In SPIDER all antenna side lobes are terminated within the telescope on the cold black Lyot stop and sleeve. *Top right*: Measured beam pattern for a 99 GHz test device, made with the White Dewar using an electrically chopped amplified noise source. Two of the sidelobes may have been stopped by the dewar aperture. The beam saturated around 4.5 dB, so the beam center has been cropped down to 6 dB. A second map (not shown) was made of the beam center (at lower source power). *Bottom*: The two measured beam maps were combined to form a single azimuthally collapsed profile (blue dots). The sidelobes peak at 13 dB around 24°, as predicted by the model. Cross sections of the model along the x-axis and along the x–y diagonal are shown as black and red lines.

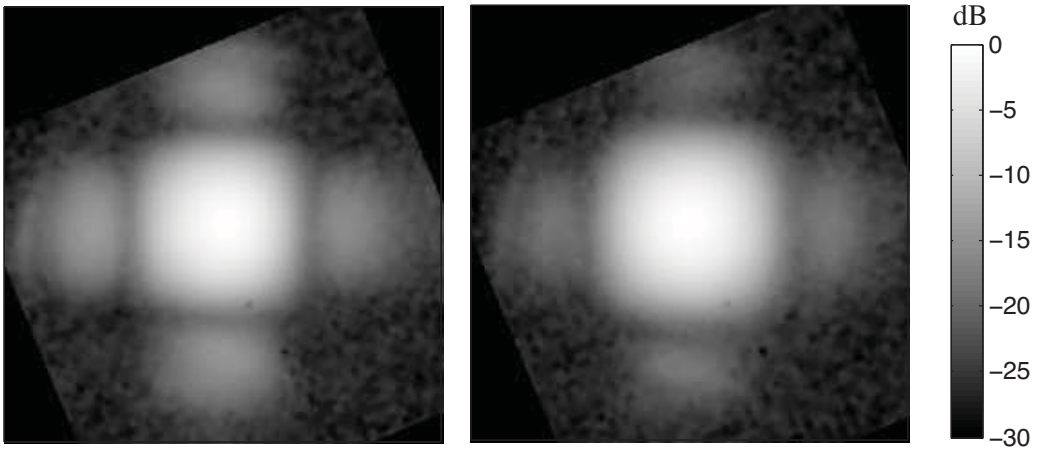

Figure 4.6: Beam maps of the antenna far field taken recently in the Short Keck cryostat. Log scale. *Left*: Antenna elements summed with uniform amplitude. *Right*: New design due to Roger O'Brient. Antenna elements summed with a Gaussian taper. The total efficiency is preserved. The side lobes are reduced and the main beam enhanced. Maps credit: KECK collaboration.

4.2 Frequency Band Definition

SPIDER's frequency bands are set by the design of the antennas and the on-chip LC filters (§3.2). Band edges must be defined sharply and appropriately to minimize response to temporally variable atmospheric line emission that can increase loading and contaminate sky maps.

Measured Bands and Band Edges

We have measured the spectra of devices in a test focal plane using a Fourier Transform Spectrometer (FTS) clamped over the window of the SPIDER test cryostat. The FTS is a Michelson interferometer built by the Princeton group, with some modifications by the Caltech group. The field of view is filled by an unmodulated liquid nitrogen source and the off-source beam is directed on to an Eccosorb absorber at ambient lab temperature. In our testing, the moving mirror was scanned across 300 mm at 2 mm/s. The results of forward and backward scans were indistinguishable above the noise. Scans were taken with the FTS centered on the window and oriented at three different axial clockings, each separated by 45°. At each clocking, scans were made at five different FTS pointing angles (adjusted by a single goniometer). More than ten devices achieved significant S/N in each scan. In this

way, adequate measurements of nearly all active devices on the focal plane were made in just a few hours. Most devices were illuminated by multiple different scans. The shape of the measured spectra showed no appreciable dependence on the orientation or pointing angle of the FTS.

A fourth degree polynomial was subtracted from each device interferogram and then a Hanning window applied. A S/N-weighted average interferogram was calculated for each tile. The FFT was taken without folding the interferogram over onto itself. The magnitude of the result was divided by ν^2 to deconvolve the device spectrum and the blackbody source spectrum ($B_\nu \propto \nu^2$ because $h\nu \ll kT$). This factor of ν^2 is responsible for the slope in the noise floor of the semilog plots.

Four notably different tiles were installed when we took spectral measurements in Run 2.1 of the SPIDER test cryostat. One was a test tile designed to measure the variation of the ILD index (see §4.1). Another was designed for a 99 GHz band center. The basic functionality of this tile was confirmed, but the spectra were affected by severe fringing because the optics of the telescope were optimized for the 148 GHz band. A third tile (designation JAB090323.1) was an older wafer, designed for a band center of 145 GHz. The target band center has been shifted up because a band centered at 145 GHz shows significant response at the 115 GHz galactic carbon monoxide line and at the 118 GHz atmospheric oxygen line. The final tile (designation JAB100104.1) was fabricated with the current design, targeting a band center of 148 GHz. The weighted average spectra of these two tiles are plotted in Figure 4.7.

The bandwidth of the 148 GHz tile

$$\Delta\nu = \frac{(\int F(\nu)d\nu)^2}{\int F^2(\nu)d\nu} \tag{4.1}$$

is 41 GHz, so $\Delta\nu/\nu_0 = 28\%$.

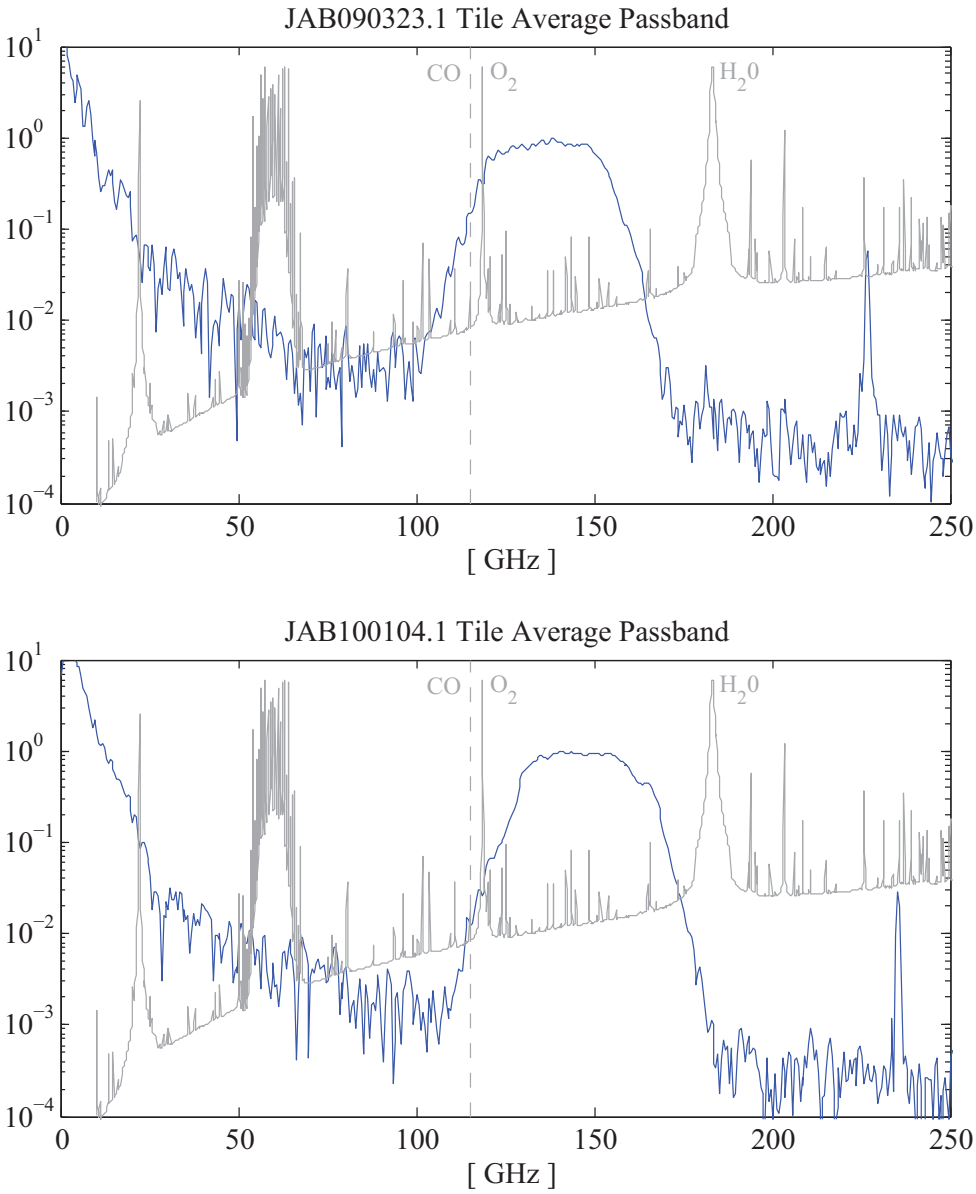

Figure 4.7: *Top*: The average passband for devices from tile JAB090323.1. This passband was judged to be too low, and tiles are now made to target a higher passband. *Bottom*: The average passband for devices from tile JAB100104.1. This newer tile was fabricated using the same filter design and ILD thickness which we use in the fabrication of 148 GHz science flight tiles. Both passband averages have been normalized to one at peak response. Plotted in grey is the atmospheric emission in pW/GHz (solid line) and the location of the J=1-0 CO transition (dashed).

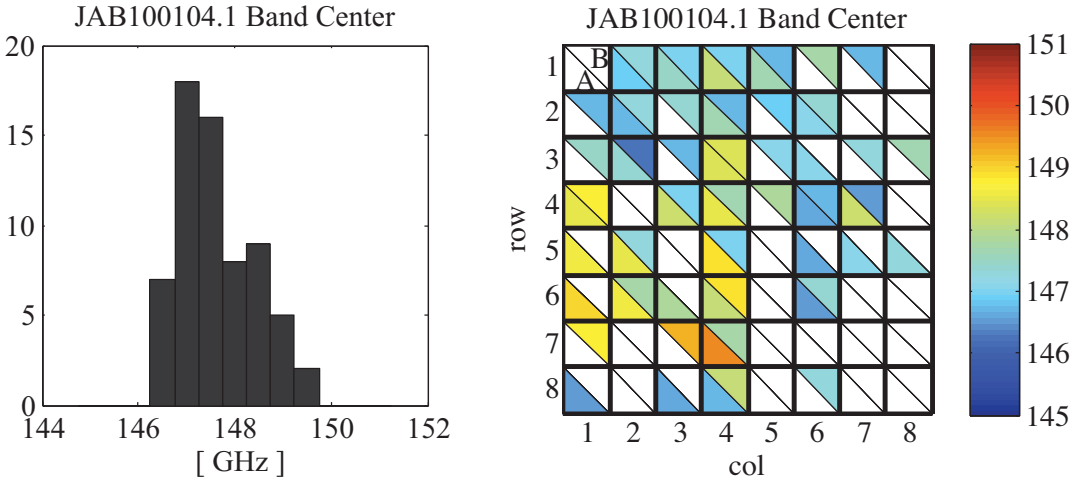

Figure 4.8: Measured band centers for devices on tile JAB100401.1. *Left*: Histogram of band centers. Due to noise in the spectral measurements this represents an upper limit on the actual dispersion in band centers. *Right*: Band centers mapped by the physical row and column of each device on the tile. There is no obvious spatial pattern.

Uniformity

Uniformity in the location of band edges is important, especially to control differential response to atmospheric and galactic CO emission lines. To date we have performed spectroscopy on just one full tile of SPIDER devices made with flightlike filters, so we do not have a good measurement of the tile-to-tile variation in band center. However, I performed spectroscopy in the White Dewar (single pixel test bed described in §4.1) on individual devices from several different 99 and 145 GHz tiles. The band centers from those measurements are tabulated in Appendix B.11. The variation in measured band centers is at the level of a couple gigahz both within a tile and between tiles. In Figure 4.8 I histogram band centers for devices on a single 148 GHz tile measured in the SPIDER test cryostat. The standard deviation is about 1 GHz. The spectra and spectral differences for A/B polarization pairs from three pixels are shown in Figure 4.9. In-band spectral differences are small and show no apparent bias, so they should subtract effectively for common mode broadband sources.

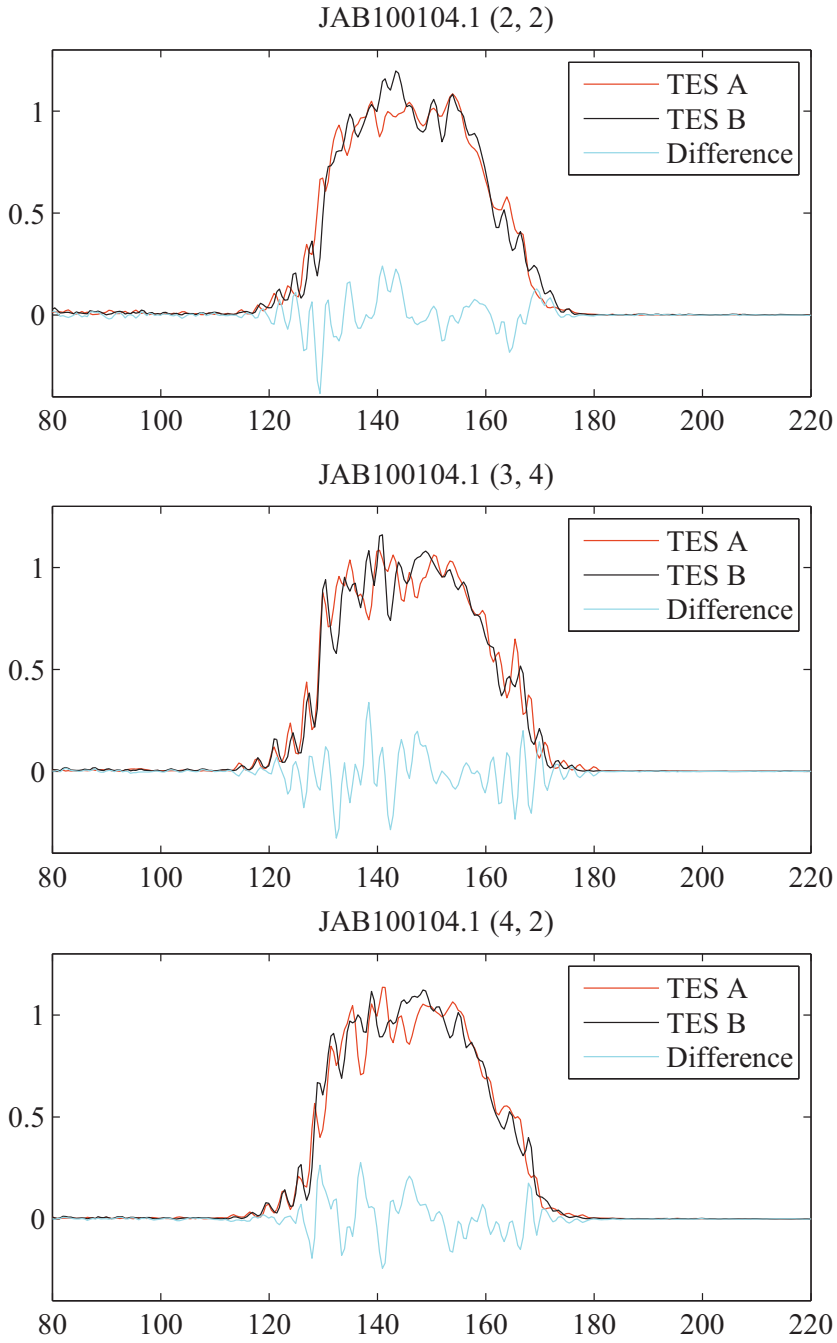

Figure 4.9: Spectra from both devices of both polarizations (A and B) for three representative pixels on test tile JAB100104.1. The relative normalization of the spectra are chosen such that the integral of the difference spectrum vanishes. The absolute normalization is arbitrarily chosen such that the mean value in the center of the band is close to unity.

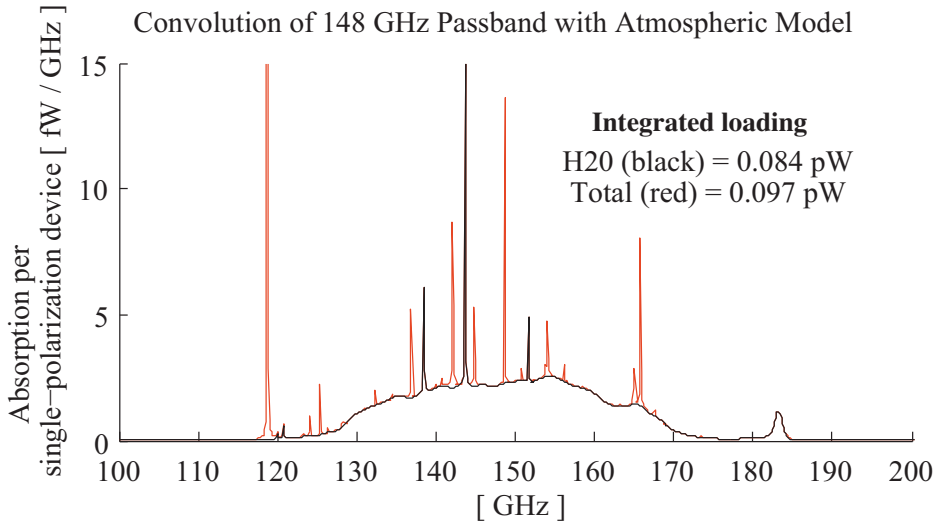

Figure 4.10: Convolution of the atmospheric model shown in Figure 2.1 with the measured passband of JAB100104.1 using the measured optical efficiency ($\eta_0 = 33\%$).

Atmospheric Lines and Interstellar CO Lines

Atmospheric emission includes both broadband water emission and narrow water and oxygen line emission (Figure 2.1). In Figure 4.10 I convolve our atmospheric model with the average measured spectrum from the 148 GHz tile (normalized by the measured optical response $dP/dT_{RJ} = 0.16$). The total predicted atmospheric loading is 0.10 pW per single-polarization device. This is comparable to the CMB loading, but a factor of a few smaller than the internal loading. The photon noise contributed by atmospheric loading is quite small compared to the measured dark noise level.

Atmospheric turbulence generates fluctuations in atmospheric emission, especially in water. A large fraction (∼85%) of the atmospheric emission absorbed by the 148 GHz band is broadband water emission, so the response to these fluctuations will be mostly common mode across the focal plane. Variations in spectral response do not average out as well for narrow emission lines. In band spectral differences between devices at the level of 10% (Figure 4.9) could result in differential coupling to atmospheric lines at a level of ∼1 fW (∼1% in gain). Variations in band center at the level of 1 GHz (Figure 4.8) would result in differential coupling of ∼2 fW to the 118 GHz oxygen line and ∼0.5 fW to the 181 GHz water line. There is little to be gained by moving the band or shrinking it. Further, the effect of in-band variation is comparable to the effect of band center variation, so improvements

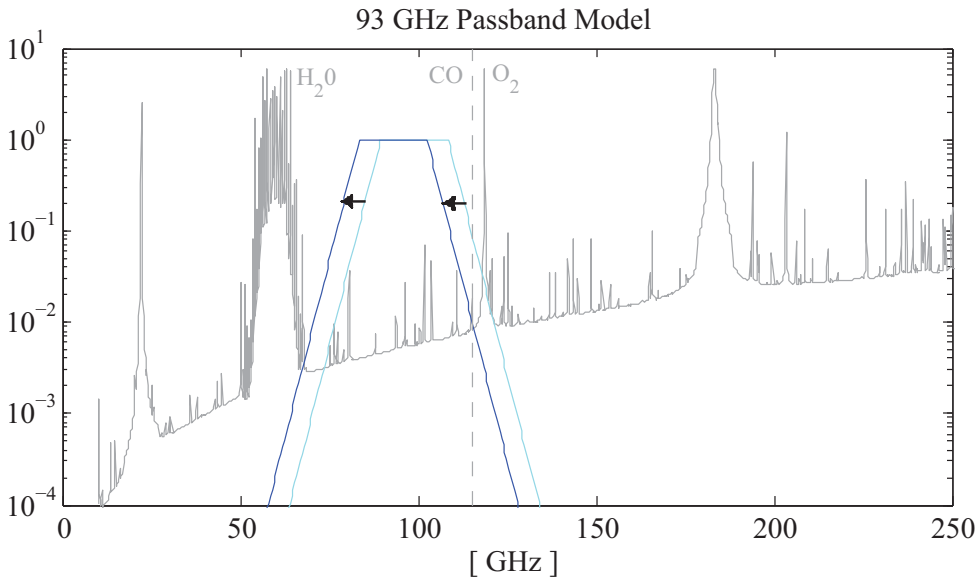

Figure 4.11: Early tiles were made with a filter that produced band centers around 99 GHz. The cyan spectrum here is a model based on measurements of individual 99 GHz devices. The blue model is a 6% lower band (the target for future tiles). Plotted in grey is the atmospheric emission in pW/GHz (solid line) and the location of the J=1→0 CO transition (dashed).

in band center uniformity would not have a dramatic impact on differential atmospheric response.

We have not yet performed spectroscopy on any devices with a band center of 93 GHz (the intended science design). Early devices exhibited a band center of 99 GHz. A few such device spectra were measured in the White Dewar. Spectroscopy was performed on an entire 99 GHz tile in the SPIDER test cryostat, but the measured spectra exhibited severe fringing because the telescope optics were optimized for the 148 GHz band. I have combined existing data on 99 GHz devices to form a passband model (Figure 4.11). The 99 GHz model exhibits unacceptably high exposure to the CO line at 115 GHz. Future tiles will be made with an LC filter designed for a band center of 93 GHz. In Figure 4.12 I convolve our atmospheric model with the 93 GHz band model normalized to $\eta_0 = 33\%$. The total predicted atmospheric loading is <0.03 pW per single-polarization device. Like the 148 GHz band, most ($\sim$85%) of the atmospheric loading is due to broadband water emission. In band spectral differences between devices at the level of 10% would result in differential coupling to atmospheric lines at a level of $\lesssim$0.4 fW ($\sim$1% in gain). Variations in

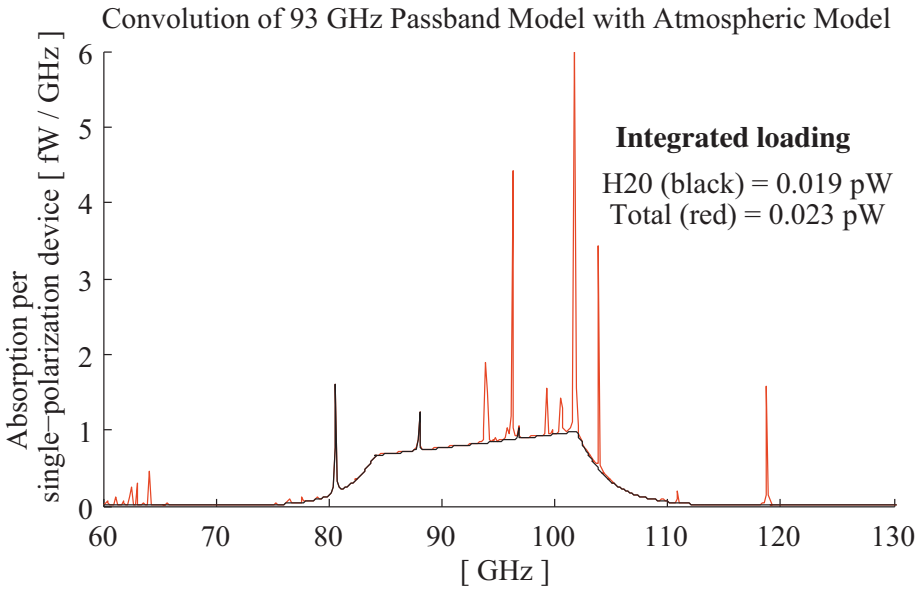

Figure 4.12: Convolution of the atmospheric model shown in Figure 2.1 with the 93 GHz band model (Figure 4.11) assuming an optical efficiency $\eta_0 = 33\%$.

band center at the level of 1 GHz would introduce differences in atmospheric coupling at a level of $\lesssim$0.8 fW, primarily in the 118 GHz oxygen line and the broadband water emission.

Above Band Reponse

Before the SPIDER test cryostat was commissioned, I optically characterized individual 145 GHz test pixels in a windowed dewar with no lenses. To measure above band response, I coupled the main beams of the detectors to a chopped blackbody source and then inserted a high-pass thick grill filter (TGF) with a cutoff around 185 GHz in to the optical path. The measured leakage was small ($\lesssim$0.5%).

When we mated detectors to our full telescope optics we discovered much higher leakage ($\sim$2%). This pickup was the result of radiation coupling directly to the TES island. Direct island coupling is not as strongly directional as the antenna beam, so it increased in a relative sense with the addition of the lenses. To reduce this response, we decreased the size of the cutout in the niobium ground plane around the TES island and added niobium to the silicon nitride support legs. We also added a low-pass metal mesh filter (7 cm^{-1} cutoff for 148 GHz focal planes) on the detector side of the eyepiece lens with a light-tight seal to the shielding enclosure. The above-band response of 148 GHz detectors coupled through

the optics is now no longer visible above our measurement noise (∼0.1%). We have not yet performed a comparable measurement for 93 GHz detectors, but the TES island geometry is the same for detectors at all frequencies.

4.3 Polarization Efficiency

Cross-polarization response (ϵ) is the magnitude of the detector response to an an input optical signal polarized in the cross-polarization direction relative to the response to a signal polarized purely in the co-polarization direction. Polarization efficiency (γ) is given by $(1-\epsilon)/(1+\epsilon)$. Cross-polarization response is measured because the amplitudes of the polarization power spectra are proportional to γ^2 [116].

Coupling a 145 GHz device in the White Dewar to a chopped thermal source, I set a 1% upper limit on polarization leakage by manually rotating a polarizing wire grid in the beam and comparing minimum and maximum coupling amplitudes to a chopped thermal source. Using the SPIDER test cryostat, Jeff Filippini coupled a 148 GHz receiver to a chopped thermal source through a small aperture filled by a polarizing wire grid. The amplitude of the coupling was measured at 11 grid orientations in steps of 11.25° from 0° to 112.5°. The results for one representative pixel are plotted in Figure 4.13. They set an upper limit of 2% on the cross-polarization response. This measurement was made with the cold half-wave plate installed.

SPIDER and BICEP2 use very similar detectors and optics. The BICEP2 collaboration has observed a linearly polarized source in the far field at telescope orientations parallel to and perpendicular to the polarization sensitivity of the detectors. They report measuring polarization leakage at or below 5×10^{-3} [2]. Polarization pairs for each pixel are coupled to physically adjacent first stage SQUID readout channels. Known cross talk between neighboring SQ1s on MUX06a chips (MUX version used by BICEP2) was measured by NIST to be at the level of 3×10^{-3} [35]. This cross talk may explain much of the observed polarization leakage in BICEP2.

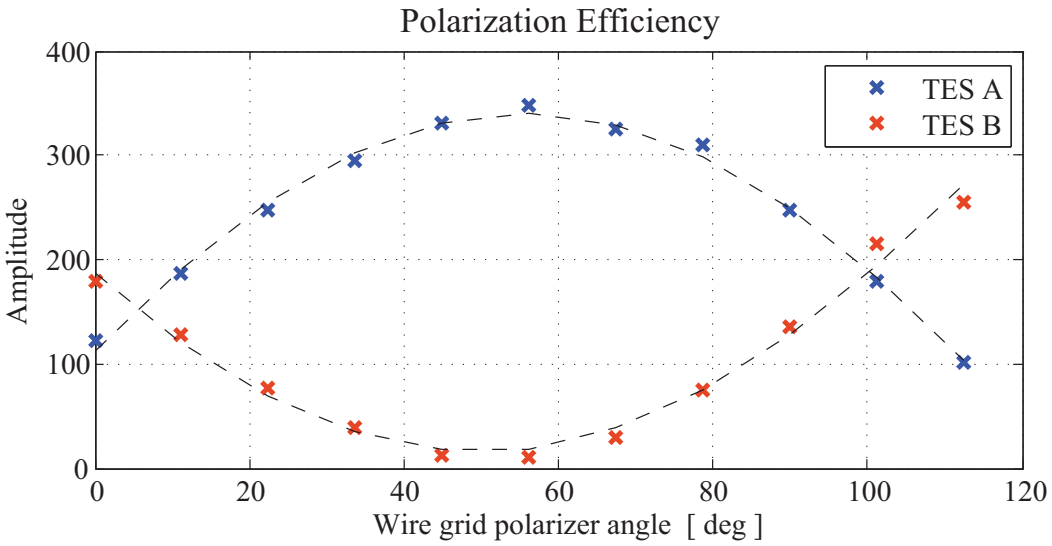

Figure 4.13: Measured device response to a thermal source polarized by a wire grid. A sinusoidal fit suggests cross-polarization response at the level of $\lesssim$2%. This measurement was made in engineering Run 2.1, and results are shown for a representative pixel (2,2) on tile JAB100104.1. Figure credit: J. Filippini.

4.4 Efficiency of Optical Response

SPIDER's sensitivity is directly related to the efficiency of its response to sky signal. In Appendix A.1 I define metrics for optical efficiency and describe the basic methods of measurement and calculation.

Measured End-to-End Response of Receiver

To measure the optical response of a receiver, we simulate variations in sky temperature by optically coupling a temperature-controlled cold black body to the telescope. The "cold load" cryostat may be bolted to the front of the primary test cryostat (Figure 4.14) or to the flight cryostat. The unit cannot be mounted and demounted while the main cryostat is cold because it shares a vacuum space with its mate. Inside, millimeter-black surfaces manufactured by Thomas Keating Ltd.[3] are tiled over a large (⌀15") beam filling copper plate. Several Lakeshore diodes are embedded within the tiles, and a resistive heater is mounted on the back side. The cold load is cooled by its own (23 L) helium tank, independent from its mating cryostat. A carbon fiber truss provides a weak thermal link between the black

[3] http://www.terahertz.co.uk/

Figure 4.14: *Left*: The cold load cryostat, about to be bolted to the front of the primary test cryostat. Infrared filters are seen here in both the test cryostat and the cold load cryostat. *Right*: Behind the filters, the cold load cryostat contains a temperature controlled beam filling black body comprised of black Thomas Keating tiles. Small pyramids on the surface increase the number of light scatterings.

body and the bath, allowing temperature control between about 5 and 20 K. We generally take load curves at about five temperatures spanning this range. Due to observed thermal transients, the system is allowed to equilibrate for ∼30 min at each cold load temperature. The resulting fits exhibit good linearity. The cold load helium tank may be emptied to allow operation well above 20 K if larger temperature variations are required.

This test configuration differs optically from the flight configuration by its exclusion of the vacuum window, but this should have a small effect on the measured optical reponse because the target loss for the thin flight window is much less than 1%. The filters which shield the cold black body will have a small effect in the opposite direction. One infrared shader is mounted on the cold load vapor-cooled shield. Two more infrared shaders and a hot press filter mount on the 4 K stage.

Measurements of the end-to-end optical response of 148 GHz band engineering grade SPIDER receivers are tabulated in Appendix B.7. We typically measure $dP/dT_{RJ} \simeq 0.15$–0.18 pW/K$_{RJ}$, corresponding to $\eta_0 \simeq 30\%$–35%. "Dark TES" (not coupled to antennas) are used to measure the level of direct optical coupling to the TES island itself. There are four dark TES on each tile (the two corner pixels along the wirebond edge). Measurements of the optical response of dark TES are tabulated in Appendix B.8. These devices typically respond at $dP/dT_{RJ} \simeq 0.002$–0.004 pW/K$_{RJ}$, or about 2% of the antenna response.

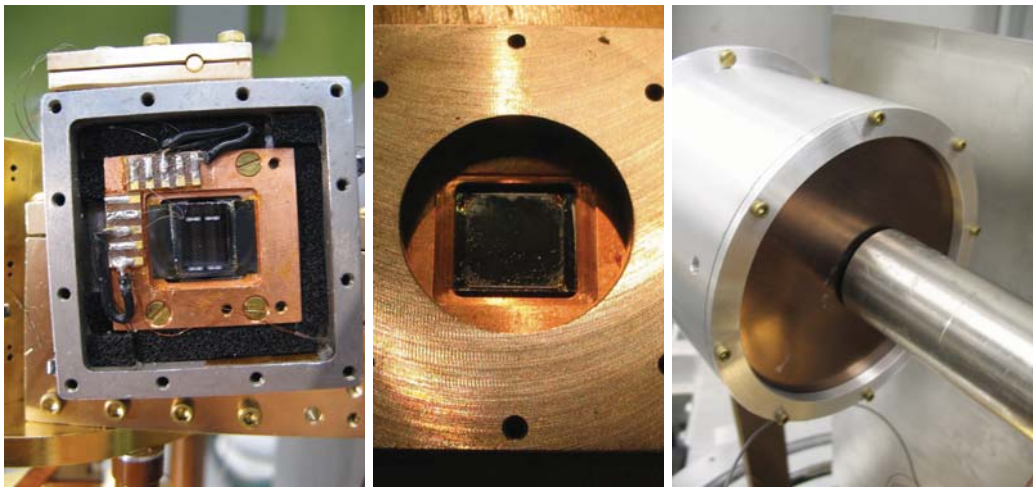

Figure 4.15: *Left*: A device mounted using GE varnish to a silicon support substrate, which is varnished to a copper mounting block inside of a niobium box (shown with niobium cover off). The backplane on the inside of the niobium cover is simply an absorber (Eccosorb LS-26/SS-3), not a quarter-wave reflective backshort. In this image the black-insulated wires are the shunt resistors (bronze wires with $\sim$3 mΩ resistance). The gold-plated copper clamp on top of the box is the mount for the Cernox thermometer. *Center*: An appropriate antireflection coating is varnished on the opposite side of the silicon substrate. *Right*: The test device is optically coupled through a niobium light pipe to a black body through a 9 cm^{-1} Ade filter and a fluorogold filter. The black body can be controlled to temperatures between 4.5 and 14.5 K.

Measured Response of Antenna-coupled Bolometers

Before we had the capability of instrumenting focal planes in the SPIDER test cryostat, I measured the properties of individual test devices in the White Dewar. Devices were optically coupled to a cold black body inside the dewar, as shown and described in Figure 4.15. The temperature of the black body was modulated between 4.5 and 14.5 K while the substrate temperature of the test device was held constant using a heater, a Cernox thermometer, and a PID control loop. PID temperature stability at the level of tenths of millikelvin was routinely achieved. The Cernox thermometer is mounted on metal, not directly on the silicon substrate. However, the relative change in temperature between an NTD thermometer mounted directly on the silicon device and the Cernox thermometer was measured to be only 0.6 mK per 10 K of black body temperature change. This is a small (1% level) correction to the efficiency measurement.

The TES electrical circuit implemented was the same as that described in §3.4. Readout was performed using a single stage commercial SQUID system (not multiplexed). I measured

the gain of each SQUID cold by ramping a known amount of current through it. Shunt resistances (∼3 mΩ) were measured by putting these resistors in parallel with TES sensors with a normal resistance (∼50 mΩ) which had been characterized precisely using a 4-wire resistance bridge measurement. These measurements of SQUID gain and shunt resistance are reliable to an accuracy of a couple percent.

The measured optical response data from 99 and 145 GHz test pixels are tabulated in Appendices B.5 and B.6. The example shown in Figure A.1 is a device measured in this manner; its designation is JAB080529 (3, 2, B).

Loss Mechanisms

Let us evaluate some of the factors that impact end to end optical efficiency. My best estimates for the transmission of various elements of the optical system are listed in Table 4.1.

Loss Mechanism	Estimated Efficiency
Sidelobes terminated by stop	75%
Antenna summing tree (ILD loss)	81%
AR-coated silicon with backshort	90%
Reflections off of 3 hot-pressed filters	90%
Absorption in lenses	91%
Half-wave plate	98%
Absorption by nylon filter	99%
Reflections off AR-coated lenses and nylon filter	$> 99\%$
Vacuum window and IR shaders	$> 99\%$
Product	**43%**

Table 4.1: Model of loss mechanisms for the 148 GHz band.

Side Lobes

Physical optics modeling performed by Marc Runyan using Zemax suggests that, in the time reversed sense, ∼76% of the optical beam power of our antennas passes through the optical stop. Most of this power lost is in the primary sidelobes. The power is terminated cold and not coupled to the sky. For devices exhibiting moderate beam steer (see Figure 4.3), modeled transmission is 73%–75%. A new summing tree has been designed that sums the elements of the antenna array with a Gaussian taper in amplitude. This should couple more power in to the main beam for future tiles (see Figure 4.6).

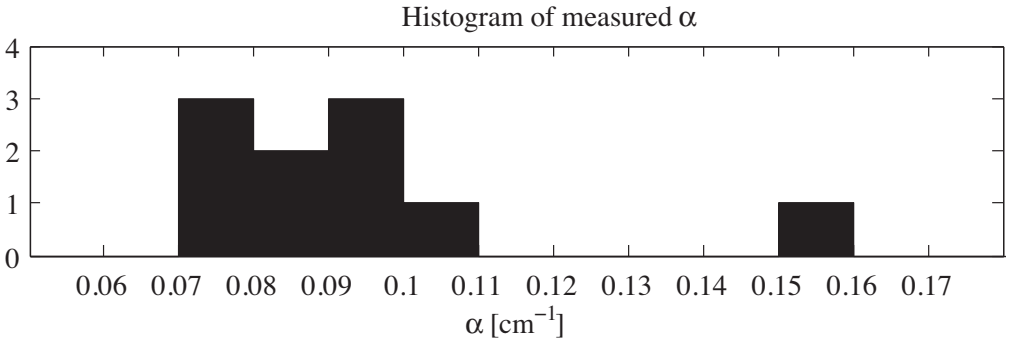

Figure 4.16: A histogram of measured values of α from a 148 GHz test tile (T100122.2). All of the devices with measured $\alpha > 0.09$ where edge pixels. The high-α outlier was a corner pixel.

Summing Tree

Power is transmitted through the superconducting Nb microstrip summing tree in a quasi-TEM mode [48, 102]. The transmission coefficient of the microstrip has both an attenuation component (real) and a phase shift component (imaginary),

$$\gamma = \alpha + i\beta. \tag{4.2}$$

The time-varying fields in the SiO_2 interlayer dielectric (ILD) substrate dissipate power as heat. This should be the dominant microstrip loss mechanism for superconducting microstrips. We have measured the attenuation per unit length (α) in the 148 GHz band with our nominal microstrip geometry, which is ∼400 nm thick Nb microstrip on 290 nm thick SiO_2 ILD over a Nb groundplane (which terminates the field penetration). We measure α using a shared single polarization 148 GHz slot antenna array coupled by Nb microstrips to two TES' through a 3 dB power divider. The microstrips coupling the divided antenna power to the two TES' are identically 3.1 μm wide. One of them is 10.8 cm longer than the other, so

$$\alpha = -\frac{1}{10.8\text{ cm}} \ln\left(\frac{\eta_{\text{long}}}{\eta_{\text{short}}}\right). \tag{4.3}$$

A histogram of measured values of α from a 148 GHz test tile can be found in Figure 4.16. This histogram includes only devices with working readout of both TES'. There is a notable spread across the tile. There also appears to be variation from tile to tile. A measurement by the Keck collaboration found ∼0.11 cm^{-1} (different tile, also SiO_2 ILD).

The length of the actual science 148 GHz device summing tree is 2.1 cm (from antenna tap to TES), so I estimate that the summing tree transmission is approximately $e^{-(2.1\ cm)(0.1\ cm^{-1})} = 81\%$ on average. The summing tree cannot easily be shortened. Loss might be reduced through the use of a different ILD material. We tested devices with a silicon nitride ILD, but found that they exhibited an unacceptable level of A/B beam offset (both measured and simulated).

Absorption and Reflection

Neglecting reflections, the transmission power fraction of a dielectric is

$$T = e^{-2\pi n t \tan(\delta)/\lambda}. \tag{4.4}$$

For the 3/32" thick Nylon 6/6 filter, I use $n \sim 1.73$, $t \sim 2.4$ mm, $\tan(\delta) \sim 8 \times 10^{-4}$ at 93 GHz and 10^{-3} at 148 GHz to estimate the absorption of the Nylon to be ∼0.6% at 93 GHz and ∼1.3% at 148 GHz. For the two HDPE lenses, I use $n \sim 1.52$, $t \sim 67$ mm (through the centers of two lenses combined — so an upper limit), $\tan(\delta) \sim 2.4 \times 10^{-4}$ at 93 GHz and 2.8×10^{-4} at 148 GHz to estimate the combined absorption to be ∼5% at 93 GHz and ∼8% at 148 GHz.

Assuming the use of 0.001" thick teflon with $n \sim 1.44$ and $\tan(\delta) \sim 4 \times 10^{-4}$, I estimate the absorption of the thin flight vacuum window to be much less than 0.1%. The in-band loss of the infrared shaders should also be less than 0.1%.

The surfaces of the lenses and the nylon filter are all covered with quarter-wave coatings to reduce reflections. An ideal coating has an index of refraction $n_{AR} = \sqrt{n_s}$ and a thickness $t_{AR} = \lambda/4n_{AR}$ where n_s is the index of the substrate [51]. This will perfectly transmit light at the wavelength λ. We have chosen (Porex brand) Mupor coating materials for their indices, availability, and workability. For example, for the 148 GHz band the lenses are coated with 0.015" thick Porex PM23DR. The index of refraction of this material (∼1.2) is well matched to the index of the HDPE lenses. It also has very low loss in the frequencies of interest. However, the thickness of a coating can only be optimized for a single frequency and will not be perfect over the finite bandwidth. Further, the thickness tolerance of the manufactured Porex is a few mils. I calculate that the reflection from each surface will therefore be on the order of tenths of a percent.

There are three metal mesh low-pass filters in the optical path of each SPIDER insert. These hot-pressed LDPE filters are fabricated and antireflection coated by Peter Ade's lab at Cardiff University. One is mounted on the cold side of the 20 K shield (VCS1) filter stack, one at the entrance to the 4 K insert, and one in the spittoon. Their cutoff frequencies depend on the frequency band that they are used for. Measurements at room temperature show that each filter has a typical band-averaged transmission of 95%–98% [108].

The half-wave plate is a polarizer and has preferred axes, so its transmission depends both on frequency and on its orientation relative to the detector polarization. The sum of the power transmitted in the two polarizations also varies with the wave plate orientation relative to the detector axes. Using Sean Bryan's model for the wave plate parameters with measured thicknesses and cold indices of refraction [24, 25, 26], I find that for a 25% square band at 148 GHz the projected band-averaged transmitted power varies from 97.4% to 97.7% (neglecting loss).

AR-coated Silicon with Backshort

SPIDER's detectors are patterned on the antisky side of 500 μm thick silicon substrates. Quartz tiles of $\lambda/4n$ thickness are clamped against the sky side of the Si substrates to minimize reflections. A reflective niobium backplane a distance of $\lambda/4$ behind the detectors increases efficiency. Incident radiation excites multiple modes in this multi-interface structure. Peter Day has calculated (for the 148 GHz band) a band-averaged forward beam power of ∼90% for this system [33]. A good fraction of the loss is in surface waves which may be transmitted out of the silicon at the edge of the wafer.

4.5 Internal Optical Loading of Devices

"Internal loading" is all of the power deposited on a TES that is not optical power from the main beam coupled to the sky. This includes, for example, absorbed emission from the filters and telescope tube. Even stable internal loading is detrimental because it can contribute significant photon noise and also reduce the saturation power margin. In the current SPIDER optical configuration, measured internal loading is larger than the optical power from the CMB and the atmosphere, so this photon noise contribution is notable.

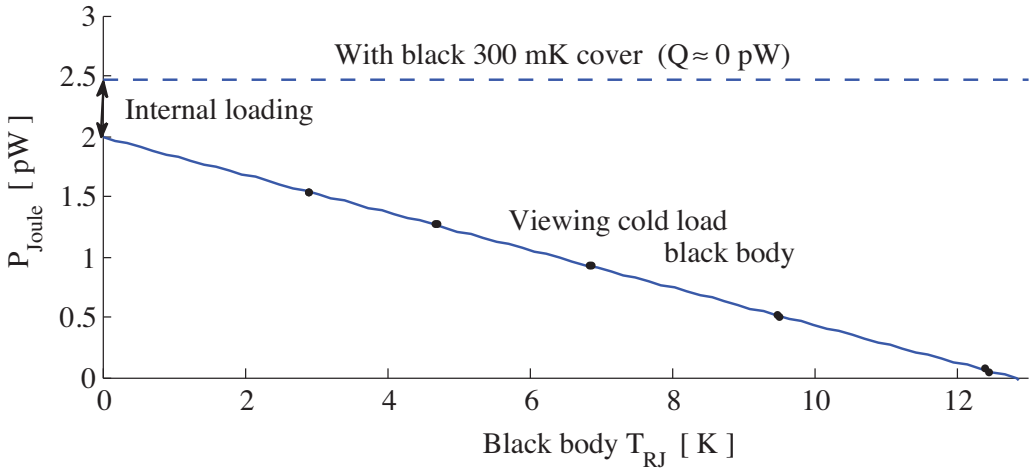

Figure 4.17: Optical response, $|dP_{Joule}/dT_{RJ}|$, is calculated by a simple linear fit. The internal loading is inferred to be the measured optical loading (Q) when the temperature of the cold load black body is extrapolated to zero. T_{sub} is kept constant throughout this measurement so that P_{legs} is constant. The red point represents a measurement of P_{Joule} on transition with a 300 mK blackened cover completely sealing the focal plane (so, $Q \simeq 0$ and $P_{Joule} \simeq P_{legs}$). The black data points here represent measurements of P_{Joule} on transition taken with the focal plane observing the blackbody cold load (at various temperatures) through the telescope tube. In this example we see that even with the effective sky temperature extrapolated to zero, the device experiences optical loading $Q = P_{legs} - P_{Joule} \approx 2.5$ pW $- 2$ pW $= 0.5$ pW.

Measured Internal Loading

The basic method that we use to measure internal loading is illustrated and described in Figure 4.17. It requires both a measurement of optical efficiency as described in §4.4 and a measurement of P_{Joule} saturation power made with the detector at the same substrate temperature but in a dark sub-Kelvin enclosure. In Appendix A.2 I describe two alternative methods for calculating internal loading. The first alternative requires more data but reduces both systematic and statistical errors in comparison with the basic method. The second alternative can be used to estimate loading when dark ($Q = 0$) data is not available.

Thus far we have only measured internal loading in the SPIDER test cryostat. The SPIDER flight cryostat has a higher Vapor-Cooled Shield 1 (VCS1) temperature than the test cryostat (∼30 K, not ∼10 K), but our VCS1 coupling measurements suggest that this will have a very small effect on loading. Assuming the use of 0.001" thick teflon with $n \sim 1.44$ and $\tan(\delta) \sim 4 \times 10^{-4}$, the loading due to the thin flight vacuum window should

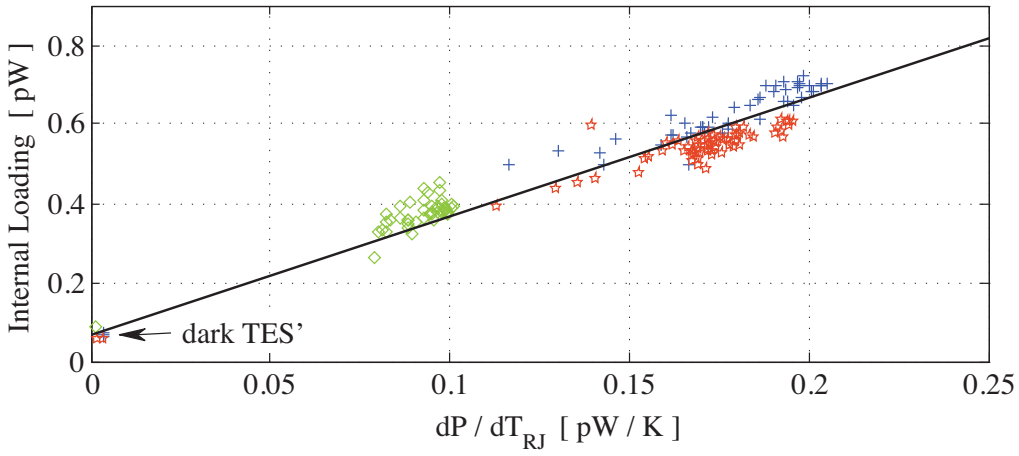

Figure 4.18: Measured internal loading (in units of power) is strongly correlated with measured response to sky loading. Devices with lower response to sky signal also exhibit lower response to internal loading sources. Variation in internal loading must therefore be dominated by the antennas themselves, not by island pickup (responsible for the DC offset) or by differential throughput at the Lyot stop (which would produce a negative correlation between internal loading and dP/dT_{RJ}). This figure plots measurements of three engineering tiles (individually colored) during test Run 3.0. Internal loading has improved since this measurement was made, but the strong correlation with sky response remains.

be less than 0.01 pW.

Measurements of the internal loading of 148 GHz band engineering grade SPIDER receivers are tabulated in Appendix B.9. I find that internal loading (measured in units of power) correlates strongly with optical efficiency (see Figure 4.18). With the current optical configuration we typically see ∼0.4 pW of internal loading in this band for characteristic devices (devices with sky response at the level of $dP/dT_{RJ} \simeq 0.15$ pW/K$_{RJ}$). "Dark TES" (not coupled to antennas) are used to measure the level of direct optical coupling to the TES island itself. Measurements of the internal loading of dark TES are tabulated in Appendix B.10. These devices typically see 0.01 pW of internal loading.

Sources of Internal Loading

Physical optics modeling performed by Marc Runyan using Zemax suggests that, in the time-reversed sense, ∼25% of the optical beam power of our antennas falls outside of the optical stop. Most of this power is in the primary sidelobes. In early optical designs this beam power was terminated on 4.2 K surfaces. Starting in May 2010 (Run 3), a 1.8 K blackened sleeve was added on the interior of the telescope tube (Figure 2.7). This reduced

Component	Contribution
Measured Antenna-coupled Internal Loading (Appendix B.9)	0.41 pW
Measured Island-coupled Internal Loading (Appendix B.10)	0.01 pW
Vacuum Window Emission	<0.01 pW
Atmospheric Loading (Figure 4.10)	0.10 pW
CMB Loading (2.725 K black body)	0.10 pW
Sum	**0.62 pW**

Table 4.2: Projected loading on a single-polarization 148 GHz device, using the measured spectrum and efficiency of tile JAB100104.1 as a model, and internal loading measurements from test Run 5. Despite reductions, internal loading is still the dominant contribution to loading and photon noise.

the expected loading from ∼0.1 to ∼0.01 pW for 148 GHz devices with average efficiency. Measurements have confirmed this improvement (see Appendix B.9).

The only emissive elements in the optical path are the lenses, the nylon filter, the half-wave plate and the window. The half-wave plate is anchored to the 4 K stage cooled by the main liquid helium cryostat. Matt Schenker found that, as expected, heating the half-wave plate by 20 K did not measurably increase the loading on the detectors (upper limit 0.005 pW). Matt also found that increasing the temperature of the first vapor-cooled radiation shield (VCS1) from 11 to 31 K increased the loading by less than 0.05 pW (generally closer to 0.01 pW). Three of the infrared shaders and one of the high-pass metal mesh Ade filters are coupled to this stage. The loading contributions of the nylon filter and lenses have not been measured. The nylon filter is located on the cold end of the filter stack mounted to the 4 K helium stage, but the temperature at the center of the filter is not known. Assuming a temperature of 5 K and an emissivity of ∼1%, we anticipate a loading contribution of less than 0.01 pW for the filter. For the lenses, we anticipate a loading contribution of ∼0.03 pW assuming a temperature of 5 K and a combined emissivity of ∼9%.

The source of the (large) remainder of the measured internal loading is not well understood. A hot-pressed filter mounted on the 4 K stage of the cold load cryostat may reflect some fraction of the beam power on to hot surfaces, contributing artificially to our measurement of internal loading. For example, a 1% coupling to a 80 K surface would generate ∼0.12 pW in loading. Any stray light from VCS2 or from the vacuum vessel which penetrates in to the telescope tube and couples to the detectors could also contribute significant loading.

4.6 Bolometer Properties

Bolometer design characteristics such as transition temperature and leg thermal conductance directly affect noise levels, as well as the power margin that protects the devices from saturating. In addition, strong uniformity of all device parameters is crucial so that the many TES' that share each electrical bias line may operate simultaneously.

Transition Temperature, Resistance, and Leg Conductance

Transition temperatures (T_c) and normal resistances (R_n) for the Ti and Al TES' in tested SPIDER engineering test tiles are tabulated in Appendix B.1 and B.2. We recently reduced the target Ti R_n in a bid to reduce aliased noise, and now measure $R_n \sim 30$ mΩ with variation between tiles on the order of 10%. We have little control over the tile average Ti T_c, which in recent years has generally landed between 500 and 525 mK. The variation within a tile is at the 1% level. The measured (thin film) aluminum transition is between 1.3 and 1.4 K, which is higher than the transition temperature of bulk aluminum (1.2 K). The Al TES is used only for lab testing and is superconducting during science mode operation. Its normal state resistance is about 0.5 Ω.

The thermal conductance of the silicon nitride legs that isolate each bolometer can be parameterized by G_{450} (or G_c) and β. We measure these parameters, as well as T_c and R_n, using the method described in §3.4 and illustrated in Figure 3.12. We also measure thermal conductance over a broader range of temperatures using the Al transition, and fit that data using G_{1340} and β. The results are tabulated together in Appendix B.3. The thermal conductance of the legs has been intentionally reduced in recent months to reduce phonon noise. We now measure $G_{450} \approx 15$ pW/K and $G_c \approx 20$ pW/K. Variation between tiles is on the order of 10%. We find $\beta = 2.0$–2.2. Prior to 2010, we did not deposit a niobium film on the bolometer legs and β was typically closer to 2.6.

The Safety Factor (SF) quantifies the saturation power margin

$$\mathrm{SF} = \frac{P_{legs}}{Q} = \frac{G_c T_c}{\beta + 1}\left[1 - \left(\frac{T_{sub}}{T_c}\right)^{\beta+1}\right] Q^{-1} \tag{4.5}$$

Devices with $Q = 0.62$ pW (Table 4.2), $G_c = 20$ pW/K, $\beta = 2.1$, $T_c = 520$ mK and $T_{sub} = 300$ mK have a safety factor of 4.4. Phonon noise $\sim T_c\sqrt{G_c}$, so we can decrease de-

tector noise by reducing G_c or T_c, but doing so diminishes the safety factor. Assuming that we only require a safety factor 2 or 3, we have some margin available. However, lowering G any further would cause the Al TES to saturate when the focal plane is optically coupled to the lab environment for beam mapping and spectroscopy. Recent devices saturate the Al transition from $T_{sub} = 300$ mK with just 70–100 pW of applied power (Appendix B.3). Assuming an optical response of 0.16 pW/K, these devices have a safety factor of only 1.5–2.1 for viewing a 300 K load. They reach their saturation point at optical load temperatures between 440 and 625 K. Clearly, the need to open the telescope to the 300 K lab environment establishes a stricter requirement than that set by normal science-mode operation. Decreasing the Ti T_c would not impact the operation of the Al TES. Since 2007, tile-averaged T_c has varied from about 450 to 600 mK. The cause of this variation is not understood, so we do not know how to target a lower T_c.

Parameter Uniformity and Shared Bias Yield

The sensitivity and linearity of a device depends on where in its transition it is biased (at what value of $R_{frac} = R_{TES}/R_n$). TES devices must be biased in a stable part of their transition to operate effectively ($R_{frac} \gtrsim 0.4$). SPIDER's multiplexing system provides only a single shared TES bias line to each multiplexer column. Bias selection thus requires a compromise between the properties of the 32 TES devices within that column. However, each column of devices can be biased independently of the other columns.

Figure 4.19 (*left*) illustrates the impact of parameter variation on effective (shared bias) device yield and on the spread in the operating R_{frac} of devices sharing a common bias. The extent to which a desirable common bias voltage may be found depends on the uniformity of the parameters of the devices. The device parameters most relevant to this discussion are transition temperature (T_c), normal resistance (R_n), leg thermal conductance (G_{450} and β), and nominal optical loading (Q).

Solving for R_{frac} using the bolometer equations in §3.4 produces

$$R_{frac} = \frac{(R_{shunt})^2 (I_{bias})^2 (R_n)^{-1}}{\dfrac{(G_{450})(450\text{mK})}{\beta+1}\left(\left(\dfrac{T_c}{450\text{mK}}\right)^{\beta+1} - \left(\dfrac{T_{sub}}{450\text{mK}}\right)^{\beta+1}\right) - Q}. \tag{4.6}$$

To assess approximate uniformity requirements, I take the partial derivative of R_{frac} with

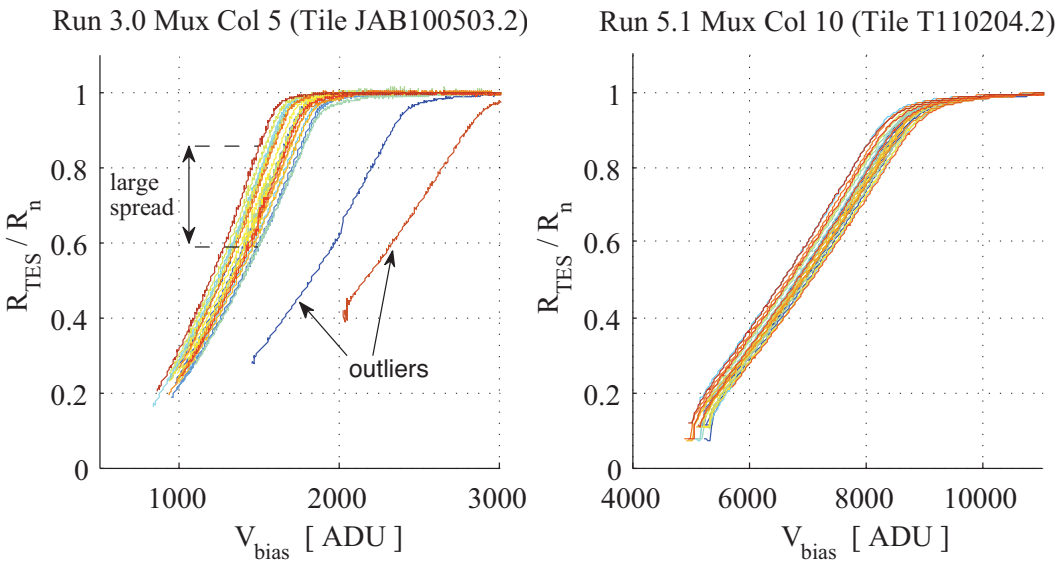

Figure 4.19: The 32 TES' on a multiplexer column share a common bias. *Left*: Variation in TES device parameters can produce a large spread in R_{TES}/R_n for any given bias choice. Outlier devices may not be stable or on transition at the TES bias voltage chosen for the multiplexer column. This example is not representative. *Right*: With our current fabrication process, we achieve a small spread with few outlying devices. This more representative example comes from test Run 5.1. I show all 21 working optically active devices from multiplexer column 10. The optical power incident on the devices $Q \approx 0.85$ pW. The noise properties of this set of devices are examined in Figure 4.22.

Parameter	σ/mean on a mux column	$\delta R_{frac}/R_{frac}$ per σ
R_n	9%	9%
G_{450}	5%	7%
T_c	1%	5%
Q	18%	5%
β	2%	0.2%

Table 4.3: Uniformity of fabricated device parameters within a multiplexor column. On the right, the contribution of each of these variations to the spread in R_{frac} for a given shared bias voltage, calculated independently for each parameter while holding other parameters constant.

respect to each fabrication-dependent device parameter. I present the resulting independent linear approximations here in dimensionless form.

$$\begin{aligned}
\frac{\delta R_{frac}}{R_{frac}} &= 2\left(\frac{\delta R_{shunt}}{R_{shunt}}\right) \\
\frac{\delta R_{frac}}{R_{frac}} &= -\left(\frac{\delta R_n}{R_n}\right) \\
\frac{\delta R_{frac}}{R_{frac}} = -\frac{1}{\mathrm{SF}-1}\left(\frac{\delta Q}{Q}\right) &\approx -0.29\left(\frac{\delta Q}{Q}\right) \\
\frac{\delta R_{frac}}{R_{frac}} = -\frac{\mathrm{SF}}{\mathrm{SF}-1}\left(\frac{\delta G_{450}}{G_{450}}\right) &\approx 1.3\left(\frac{\delta G_{450}}{G_{450}}\right) \\
\frac{\delta R_{frac}}{R_{frac}} = -\frac{(G_{450})(450\mathrm{mK})}{Q}\frac{1}{\mathrm{SF}-1}\left(\frac{T_c}{450\mathrm{mK}}\right)^{\beta+1}\left(\frac{\delta T_c}{T_c}\right) &\approx -5.0\left(\frac{\delta T_c}{T_c}\right) \\
\frac{\delta R_{frac}}{R_{frac}} = \frac{\mathrm{SF}}{\mathrm{SF}-1}\left\{\left(\ln\left(\frac{T_c}{450\mathrm{mK}}\right)-\frac{1}{\beta+1}\right)\left(\frac{T_c}{450\mathrm{mK}}\right)^{\beta+1}-\right. & \\
\left.\left(\ln\left(\frac{T_{sub}}{450\mathrm{mK}}\right)-\frac{1}{\beta+1}\right)\left(\frac{T_{sub}}{450\mathrm{mK}}\right)^{\beta+1}\right\}\left(\frac{\delta\beta}{\beta}\right) &\approx -0.09\left(\frac{\delta\beta}{\beta}\right)
\end{aligned}$$

I have assumed the nominal values $Q = 0.62$ pW, $G_{450} = 15$ pW/K, $\beta = 2.1$, $T_c = 520$ mK, and $T_{sub} = 300$ mK. For these values the safety factor (SF) is 4.4. We see, for example, that fractional uniformity requirements for T_c are much stricter than those for Q or β. Measurements of standard deviations within a multiplexer column of various device parameters are tabulated in Appendices B.4 and B.7. With the currently achieved uniformity, the independent $\delta R_{frac}/R_{frac}$ for each of these parameters is less than 10% (see Table 4.3).

Our effective device yield is not limited by uniformity considerations (Figure 4.19, *right*).

The bias sharing requirement has a relatively small effect on focal plane sensitivity (Figure 4.22, *bottom left and right*). This has not always been the case. Prior to 2007, Ti was sputtered using a smaller gun. Then, Ti thickness varied by approximately 30% from the center to the edge of the wafer with comparable ($\sim$30%) variation in R_n, and $\sim$2% variation in T_c. This was resolved by upgrading to a larger (6") sputtering gun (§3.3).

4.7 Noise Performance

Assuming good control of systematic effects, noise and optical efficiency will determine SPIDER's sensitivity and mapping speed.

Measuring Noise

To measure noise performance, we record data in the filtered readout mode in which we expect to take science data (*data_mode*=10). Optical loading is held constant and the focal plane rests at its base temperature. We characterize noise as a function of TES bias. A load curve is taken to determine the R_{TES} at each V_{bias}. The detectors are then biased and the tile heaters pulsed to put the TES' in to the normal state. We wait ($\gtrsim$30 min) for the focal plane to thermally equilibrate at its base temperature. Because the housekeeping readout for the SPIDER test cryostat carries RF noise into the cryostat, we unplug both of the housekeeping cables (serving the telescope insert and the cryostat) while taking data. Only the heater power to the fridge heat switch is connected. A script takes 1–2 min of data, reduces V_{bias}, pauses for 30 s to allow the system to settle, and then takes the next noise trace. This is repeated until all devices are superconducting. The bias steps are generally chosen to be small enough that more than ten noise traces are taken across the transition of each device.

Each time trace data is first converted from the native readout units to units of equivalent current at the TES. I subtract a 1st-order polynomial to reduce the effects of temperature drift, break the trace in to eight segments with a boxcar window function, and take the discrete Fourier transform of each segment. The squared magnitude of the result is called a periodogram. The eight periodograms are averaged. The averaged periodogram is a measure of noise variance per unit frequency. It is symmetric about $\nu = 0$, so without loss of information, the variance at negative frequencies is then folded over in to the positive

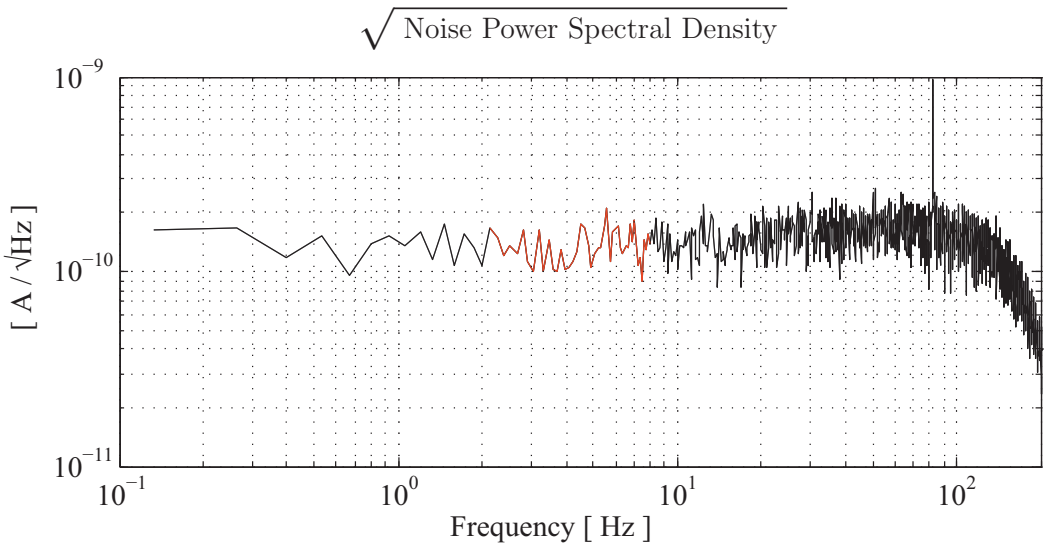

Figure 4.20: The square root of the noise power spectral density (PSD) for a noise trace taken during Run 5.1. The PSD is the noise variance per unit frequency. This representative PSD is from device (5,2,A) on tile T110204.2 at $R_{TES}/R_n = 0.68$ ($V_{bias} = 66$ μA).

frequencies. Effectively, the PSD is enhanced by a factor of two so that it need only be integrated over positive frequencies. I take the square root of the resulting PSD to put the results in units of pA/$\sqrt{\text{Hz}}$. A representative example is shown in Figure 4.20.

The 1–10 Hz frequency decade is the primary science band, chosen to reduce exposure to 1/f noise at lower frequencies and excess TES noise at higher frequencies. SPIDER will scan the sky at $\sim 6^\circ$/s to put the angular scales of scientific interest ($1^\circ \lesssim \theta \lesssim 10^\circ$) into this frequency regime. In Figure 4.21 I plot the level of the science band noise (median of the $\sqrt{\text{PSD}}$, 2–8 Hz) for the example device over a range of V_{bias} values through its transition. I call this the Noise Equivalent Current (NEI).

This data was recorded in Run 5.1 in *data_mode*=10 using the flightlike low power MCE and the flightlike filtered VICOR power supply. The *data_rate*=38 and *row_len*=80, so data packets were written to disk at 498.4 Hz. This readout configuration is roughly representative of the planned flight configuration, though in flight we plan to use a larger *data_rate*. The focal plane was viewing the cold load at $T_{CL} = 5.7$ K, so $Q \approx 0.85$ pW, a bit more than the anticipated flight loading (0.62 pW, Table 4.2). The example device used in Figures 4.20 and 4.21 is on tile T110204.2 and was read out by mux column 10. The devices on col 10 exhibited an average $T_c = 512$ mK, $R_n = 32$ mΩ and $G_c = 17.4$ pW/K.

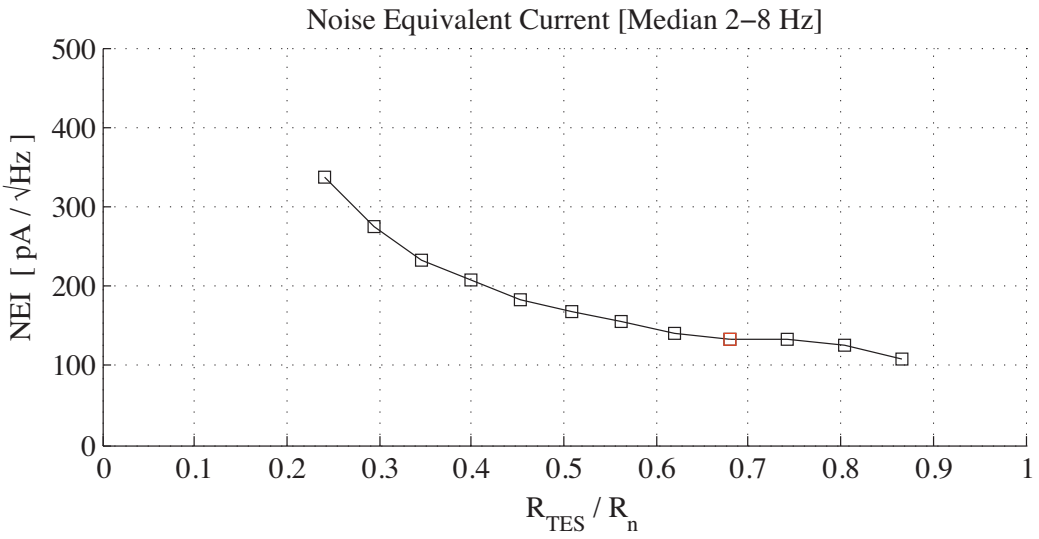

Figure 4.21: The median value of the measured $\sqrt{\text{PSD}}$ in the range 2–8 Hz for noise traces taken at various bias points. The data point from Figure 4.20 is highlighted. Low in the transition, the device becomes unstable and noise increases rapidly.

This is fairly representative of the current design.

In Figure 4.22 I plot the measured science band noise for all (21) working devices on col 10. The power-to-current responsivity is a complex function of the time constants of the system and is difficult to calculate. However, we can approximate the Noise Equivalent Power (NEP) as simply the NEI multiplied by V_{TES}. In the plots, the top end of the transition has been cut off as the NEP approximation begins to fail at high R_{TES}/R_n, introducing an artificial reduction in NEP. We divide NEP by the measured optical response (dP/dT_{RJ}) to convert to NET_{RJ}. For these devices, dP/dT_{RJ} = 0.15–0.16 pW/K_{RJ}. At 148 GHz, the conversion factor from NET_{RJ} to NET_{CMB} is ∼1.7. Converting from the $\sqrt{\text{PSD}}$ [$\mu\text{K}_{CMB}/\sqrt{\text{Hz}}$] to the more palpable sensitivity [$\mu\text{K}_{CMB}\sqrt{\text{s}}$] requires division by $\sqrt{2}$ to compensate for our earlier folding of negative frequencies on to positive frequencies. I plot NET against both R_{TES}/R_n and V_{bias}.

Because all of the TES' on a mux column share a common bias, TES biases cannot be individually optimized. In Figure 4.23 I use a rough metric to examine the resulting noise penalty. I conclude that with the present levels of detector uniformity the penalty is <10%.

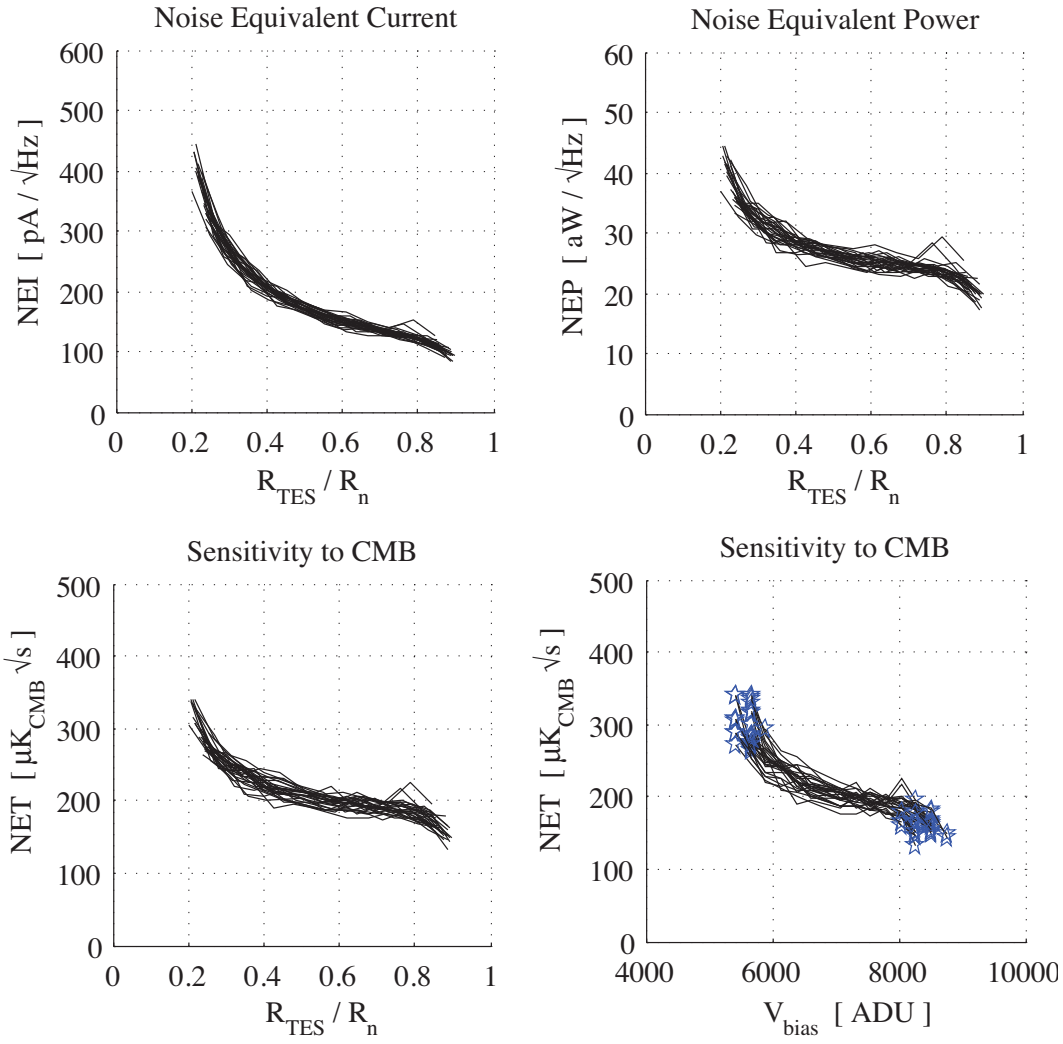

Figure 4.22: *Top left*: Noise Equivalent Current (NEI, [pA/$\sqrt{\text{Hz}}$]) at 2–8 Hz as a function of R_{TES}/R_n for all (21) working optically active devices from multiplexer column 10 in test Run 5.1. *Top right*: Noise Equivalent Power (NEP, [aW/$\sqrt{\text{Hz}}$]), approximated as NEI$\times V_{TES}$. *Bottom left*: Noise Equivalent Temperature (NET, in [μK$\sqrt{\text{s}}$]). *Bottom right*: All TES on a multiplexer column share a common voltage bias. The same NET data is plotted again here, this time by V_{bias}. The curves for each device are capped off (with blue stars) to only show data in the range $0.2 < R_{TES}/R_n < 0.9$.

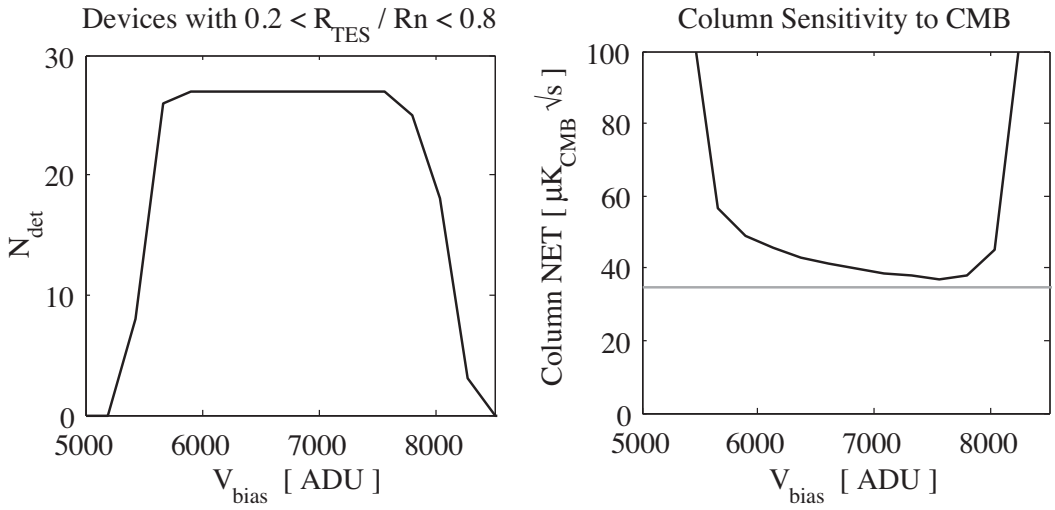

Figure 4.23: Rough estimator of the impact of device variation on noise performance, using the same data as Figure 4.22. *Left*: For each bias point, the number of devices in the sample mux column with $0.2 < R_{TES}/R_n < 0.8$. *Right, in black*: NET for the column plotted against V_{bias}, calculated as the quadrature sum of the NETs of all devices in the specified resistance range divided by the number of such devices. *Right, in grey*: The quadrature sum of the NETs of all devices at $R_{TES}/R_n \lesssim 0.8$ divided by the number of devices. The minimum of the black curve exceeds the level of the grey line by <10%.

Noise Components

Irwin and Hilton [64] provide an excellent review of the relevant TES noise components. We will now step through some of the primary constituents and evaluate the levels of their contribution.

The random arrival of discrete photons on a detector adds noise to the system.

$$\begin{aligned} \mathrm{NEP}^2_{photon} &= \mathrm{NEP}^2_{shot} + \mathrm{NEP}^2_{bose} \\ &= 2h\nu Q + 2Q^2(\Delta\nu)^{-1} \end{aligned} \tag{4.8}$$

In Figure 4.24 I compare the measured noise properties of 148 GHz devices that are nearly dark with those under an optical load $Q = 0.83$. Based on Equation (4.8), the expected $\mathrm{NEP}_{photon} = 14$ aW/$\sqrt{\mathrm{Hz}}$, dominated by shot noise. Summing this in quadrature with the observed dark noise (20 aW/$\sqrt{\mathrm{Hz}}$) produces 24 aW/$\sqrt{\mathrm{Hz}}$, in agreement with the measured noise of the optically loaded devices. The anticipated SPIDER flight loading for 148 GHz band devices is $Q = 0.62$ pW (see Table 4.2), so the expected $\mathrm{NEP}_{photon} = 12$ aW/$\sqrt{\mathrm{Hz}}$.

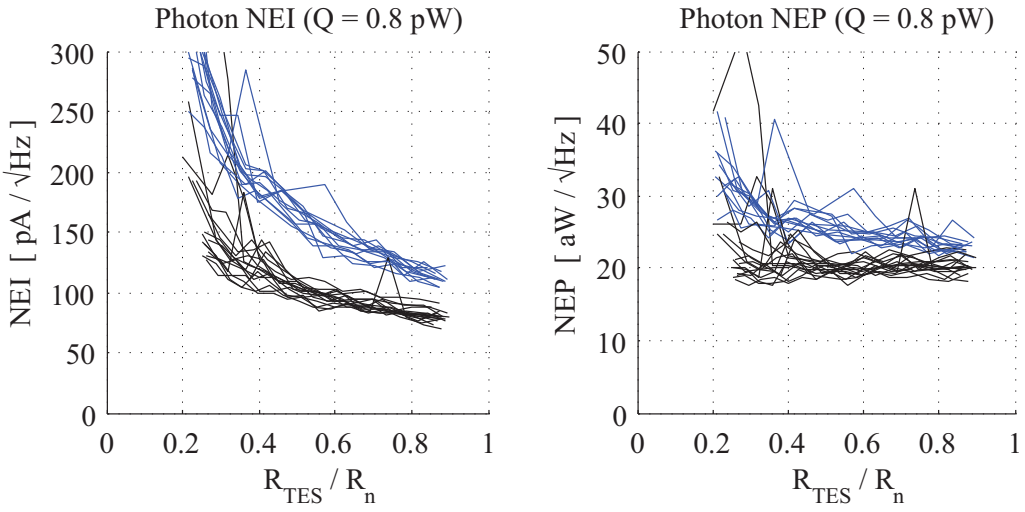

Figure 4.24: Tile T110204.3 was impacted by a severe etching problem which decoupled more than half of the bolometers from their antennas. This science band noise data comes from mux col 13 of Run 5.1, taken with the cold load at 5.7 K. For the working devices (blue), the average $Q = 0.83$ pW. For the "dark" devices (black), the average $Q = 0.04$ pW.

In power units, $\mathrm{NEP}_{photon} \propto \sqrt{\eta}$, but in temperature units $\mathrm{NET}_{photon} \propto 1/\sqrt{\eta}$.

The thermal link between the bolometer island and the substrate introduces phonon noise, given by

$$\mathrm{NEP}^2_{phonon} = 4k_B\gamma T_c^2 G_c \tag{4.9}$$

where k_b is the Boltzmann constant and γ is a correction factor of order unity that is due to the temperature gradient across the thermal link. Using the framework and assumptions of Mather [91], I find

$$\gamma = \frac{\beta+1}{2\beta+3}\frac{\left(1-(T_{sub}/T_c)^{2\beta+3}\right)}{(1-(T_{sub}/T_c)^{\beta+1})}. \tag{4.10}$$

For the (mux col 13) devices of Figure 4.24, $\beta \approx 2.1$, $G_c \approx 16.6$ pW/K, $T_c \approx 506$ mK and $T_{sub} = 294$ mK, so $\gamma = 0.52$ and $\mathrm{NEP}_{phonon} = 11$ aW/$\sqrt{\mathrm{Hz}}$.

Thermal agitation of electrons in the resistors produces Johnson noise [65], given by

$$\begin{aligned} \mathrm{NEP}^2_{Johnson} &= \mathrm{NEP}^2_{TES} + \mathrm{NEP}^2_{shunt} \\ &= 4k_B T_c R_{TES} I^2_{TES} \mathcal{L}^{-2} + 4k_B T_{shunt} R_{shunt} I^2_{TES} (\mathcal{L}-1)^2 \mathcal{L}^{-2}. \end{aligned} \tag{4.11}$$

For our example devices, $\mathrm{NEP}_{TES} = \mathcal{L}^{-1}(11$ aW/$\sqrt{\mathrm{Hz}})$. We believe that $\mathcal{L}$ is on order

100, so the TES Johnson noise is negligible. The shunt resistor (3 mΩ) is mounted at $T_{shunt} = 300$ mK, so $\mathrm{NEP}_{shunt} = (R_{TES}/R_n)^{-1/2}(1.7\ \mathrm{aW}/\sqrt{\mathrm{Hz}})$, which is subdominant to the phonon noise.

The measured dark NEP (here ∼20 aW/$\sqrt{\mathrm{Hz}}$) is significantly higher than the calculated phonon noise (11 aW/$\sqrt{\mathrm{Hz}}$). The difference (∼17 aW/$\sqrt{\mathrm{Hz}}$, added in quadrature) is not well understood. It is thought to be the result of aliased excess TES noise and amplifier noise. Understanding and reducing the unexplained noise is a top priority for SPIDER. Jeff Fillippini has led this effort. Summing the calculated phonon noise in quadrature with the measured photon noise gives 16 aW/$\sqrt{\mathrm{Hz}}$. Accomplishing sensitivity at this level would translate in to a ∼2.3× improvement in mapping speed compared to the currently measured ∼24 aW/$\sqrt{\mathrm{Hz}}$. This would become 13 aW/$\sqrt{\mathrm{Hz}}$ (a ∼3.4× mapping speed improvement) if, in addition, the internal loading were nulled (so Q=0.2 pW).

4.8 Temperature Stability

Temperature changes within a telescope can generate false signals in detector time streams.

Thermal fluctuations of a focal plane or of individual detector tiles change the amount of power that flows out through the silicon nitride bolometer legs. From §3.4, we know that $(dP_{legs}/dT_{sub}) = G\,(T_{sub}/T_0)^{\beta}$. For $G_{450} = 15$ pW/K, $\beta = 2.1$, and $T_{sub} = 300$ mK, a 148 GHz detector with dP/dT_{RJ}=0.16 pW/K would respond to a 1 nK change in focal plane temperature at approximately the same level as a 70 nK change in CMB temperature. Over a hundred gold wire bonds per tile provide a measured 245 μW/K thermal coupling between each tile and the detector plate. We do not currently have plans to implement PID temperature control for the detector plate. Temperature stability is achieved using stainless steel heat capacity blocks. The measured 3 dB point of the thermal transfer function between the fridge and detector plate is at 2 mHz.

Most response to FPU temperature fluctuations should be common mode. There are four dark TES channels and one NTD Ge thermistor on each detector tile. Dark TES channels are exactly the same as other channels except that the TES' are not coupled to antennas, so they may be used to isolate and regress focal plane temperature variations out of the science data. Bolometers will vary in the level of their response to fluctuations due to variations in G (at the ∼5% level). We plan to measure G for all science devices prior

to flight, so in principle this variation can be accounted for if it is necessary to subtract the effects of FPU thermal fluctuations from flight data.

Side lobes comprise about 25% of the total power of SPIDER's antennas. They are terminated on the cold dark interior of each telescope tube. Variations in the temperature of the terminating surface can produce correlated signal. Historically side lobe termination occurred on 4 K surfaces cooled by the main helium tank. Now side lobes are terminated on a 1.8 K black Lyot stop and sleeve cooled by the superfluid helium tank. This greatly reduces the optical power that they absorb. A 148 GHz detector with 0.16 pW/K_{RJ} sky coupling and 0.05 pW/K_{RJ} stop coupling would respond to a 1 μK change in stop temperature at approximately the same level as a 200 nK change in CMB temperature. The temperature of the stop will vary in flight due to changes in loading and changes in the superfluid helium bath temperature with altitude. We know very little about the stability of the system. Roger O'Brient has recently designed a Gaussian-tapered summing tree that should reduce the amount of antenna beam power in the side lobes, loosening the requirements on the temperature stability of the stop.

Drifts in the temperature of SQUID series array (SSA) modules or first and second stage SQUIDs can produce patterns which are visible across an entire focal plane (including dark SQUIDs). This was observed when the SSA modules were cooled to sub-Kelvin temperatures in the original RevX focal plane design. They did not perform well at these low temperatures. The SSA modules are now mounted off of the liquid helium cooled stage and self heat to >5 K with significantly reduced resonance effects and improved temperature stability. The amplitude of the coupling between the SSA temperature and the detector readout has not yet been quantified.

4.9 Magnetic Field Response

As discussed in §2.8, the SQUID and TES systems are both responsive to magnetic fields. Because SPIDER will travel around the Antarctic continent while spinning and tipping in elevation, the effects of Earth's magnetic field will be variable and difficult to model. Extensive magnetic shielding has therefore been incorporated into the SPIDER instrument. Much of the shielding design and testing is due to Marc Runyan, and is described in Runyan et al. [107].

We test the effectiveness of the shielding in the lab using Helmholtz coils. The coils are 79 cm in diameter and are centered around the focal plane. Testing is performed along three perpendicular sets of axes including the primary axis of the telescope. Along the axes perpendicular to the primary telescope axis the cryostat is too large to permit the spacing of the coils in the true Helmholtz configuration (one half diameter apart). The coils are driven in series by a current amplifier with a sinusoidal frequency generator. To calibrate our results we calculate the expected field strength between the coils in the absence of shielding. In recent testing (during Run 4.1) the applied fields were around 15 $B_{\rm Earth}$ peak to peak, modulated at 0.27 Hz. Increasing the fields beyond this point produces significant inductive heating in the cryostat. The detectors are biased in their transition to include the possible TES response in addition to the SQUID response. We integrate for ∼12 hr, often overnight. The housekeeping cables are removed to reduce RF pickup.

The signal is extracted directly from the PSD at the coil current modulation frequency. Measured response is translated in to units of $\mu K_{CMB}/B_{\rm Earth}$ assuming commonly achieved 148 GHz band optical response (∼0.1 pW/K_{CMB}). Only 1% of channels exhibited pickup in excess of 10 $\mu K_{CMB}/B_{\rm Earth}$ along any of the axes. For detections with a signal-to-noise ratio greater than 3, the median measured response was ∼2 $\mu K_{CMB}/B_{\rm Earth}$ along all three axes. Regression using dark SQUID response or pixel pair differencing may further damp the contamination of science data. Simulations predict that the measured response to magnetic fields would produce false B-mode signal at the level of less than 3% of the $r = 0.03$ B-mode signal across all multipoles [95]. Magnetic pickup will thus not affect SPIDER's ability to achieve its science goals.

4.10 Summary and Recommendations for Future Work

I summarize the measured performance of 148 GHz band engineering grade SPIDER detectors and receivers in Table 4.4.

To date, we have 1D far field beam slices for only a couple of pixels (with no 2D beam maps). In §4.1 I discussed the level of differential beam effects measured in SPIDER and in BICEP2. According to simulations, differential pointing produces the only significant systematic effect. In coming months, we will begin to map the far field beams of entire telescope inserts. Measuring the amplitude of the differential pointing and confirming that

Far Field Beams (§4.1)		
Beam size σ	14.6'	SPIDER
Beam ellipticity $e = (\sigma_{maj} - \sigma_{min})/\sigma$	$3\% \pm 3\%$	BICEP2 [2]
Differential pointing $\lvert\mathbf{r}_A - \mathbf{r}_B\rvert/\sigma$	$\begin{cases} 2.4\% \\ 10\% \pm 4\% \end{cases}$	$\begin{cases} \text{SPIDER, 1 pixel} \\ \text{BICEP2 [2]} \end{cases}$
Differential beam size $\lvert\sigma_A - \sigma_B\rvert/\sigma$	$\begin{cases} 0.6\% \\ 0.3\% \pm 0.2\% \end{cases}$	$\begin{cases} \text{SPIDER, 2 pixels} \\ \text{BICEP2 [2]} \end{cases}$
Differential ellipticity $\lvert e_A - e_B\rvert/2$	$1.2\% \pm 9\%$	BICEP2 [2]
Frequency Band (§4.2)		
Band center ν_0	148 GHz	SPIDER
Bandwidth $\Delta\nu = (\int F(\nu)d\nu)^2 / \int F^2(\nu)d\nu$	41 GHz	SPIDER
Variation in atmospheric gain	<5%	SPIDER
Above band response	<0.1%	SPIDER
Polarization Efficiency (§4.3)		
Cross-pol response (ϵ)	$\begin{cases} <2\% \\ \lesssim 5\times10^{-3} \end{cases}$	$\begin{cases} \text{SPIDER} \\ \text{BICEP2 [2]} \end{cases}$
Optical Response (§4.4)		
End-to-end per-polarization response	0.15–0.18 pW/K$_{RJ}$	SPIDER
Band average efficiency $\left(\int \eta(\nu)d\nu\right)/\Delta\nu$	∼30%	SPIDER
Direct island coupling	0.004 pW/K$_{RJ}$	SPIDER
Optical Loading (§4.5)		
Antenna-coupled internal loading	2.6 K$_{RJ}$ (0.4 pW)	SPIDER
Island-coupled internal loading	0.01 pW	SPIDER
Atmospheric loading	0.6 K$_{RJ}$ (0.1 pW)	Calculated
CMB loading (2.725 K)	0.6 K$_{RJ}$ (0.1 pW)	Calculated
Bolometer Properties (§4.6)		
Mean, Tile-Tile Var., On-Tile Var.		
Transition temperature T_c	520 mK, 2%, 1%	SPIDER
Leg thermal conductance G_c	20 pW/K, 15%, 5%	SPIDER
Normal resistance R_n	30 mΩ, 10%, 9%	SPIDER
Safety Factor P_{legs}/Q	4–5	SPIDER
Noise (§4.7)		
Device NEP$_{\text{phonon}}$	12 aW/$\sqrt{\text{Hz}}$	Calculated
Device total NEP$_{\text{dark}}$	18–20 aW/$\sqrt{\text{Hz}}$	SPIDER
Device NEP$_{\text{photon}}$ ($Q = 0.6$ pW)	12 aW/$\sqrt{\text{Hz}}$	SPIDER
Device total NET	∼180 μK$_{CMB}\sqrt{\text{s}}$	SPIDER
FPU NET (assuming 85% yield)	∼9 μK$_{CMB}\sqrt{\text{s}}$	Calculated
Shared-bias noise penalty	<10%	SPIDER
Temperature Stability (§4.8)		
Response to ΔT_{FPU}	∼70 nK$_{CMB}$/nK$_{\text{FPU}}$	Calculated
Response to ΔT_{stop}	∼200 nK$_{CMB}$/μK$_{\text{FPU}}$	Calculated
Magnetic Field Response (§4.9)		
X/Y axes	<10 μK$_{CMB}/B_\oplus$	SPIDER
Z axis	<10 μK$_{CMB}/B_\oplus$	SPIDER

Table 4.4: Summary of current measured receiver performance — 148 GHz band

it does not rotate with the half-wave plate should be high priorities. These will also be the first beam measurements made for the 93 GHz band.

In §4.2, I reviewed measurements of the 148 GHz passband and modeled the 93 GHz passband. The band centers are well placed to minimize optical loading and differential response to atmospheric emission. There is some room to increase the bandwidth of the 93 GHz band. The first step, though, will be to measure the spectral response of this band with the new filter design. The ∼280 GHz band will not be included in the first flight of SPIDER, so it has not yet been designed or tested. Designing the summing tree for the 280 GHz band will be a difficult challenge, as the scaling down of the antenna structure leaves very little room for the microstrip summing tree.

The measured polarization efficiency (§4.3) is high (>98%), so no development effort to reduce cross-polarization response is justified. Rather, to reduce systematic errors in signal reconstruction, future efforts should focus on precise characterization of the polarization angles and polarization efficiencies of the actual flight devices.

In §4.4 I developed a model of the loss mechanisms of the system that is nearly sufficient to explain the observed end-to-end optical efficiency of the 148 GHz band. The most significant loss is in the antenna sidelobes, which are terminated cold. Development of antennas with a Gaussian feed structure (now in early testing) should couple more power into the main beam. The second largest contribution to loss is attenuation along the microstrip summing tree. The tree cannot be shortened significantly, so this could only be reduced by finding and substituting a lower loss material for the interlayer dielectric, which would likely be a very substantial development project (not merited at this point).

The measured internal loading of the receiver in the 148 GHz band is currently twice as large as the projected CMB loading and atmospheric loading combined (§4.5). A reduction would therefore produce a significant improvement in the photon noise, which is currently comparable to the calculated phonon noise. Decreasing internal loading will become a particularly worthwhile focus if aliased noise is reduced to the point that the total dark noise is dominated by phonon noise. At this point, despite significant effort, we do not have a good model to account for the measured internal loading (in fact, it could result from some small stray coupling to a warm stage in the cold load cryostat). We do know that the majority of the observed loading scales linearly with the observed sky response, so it must couple to the bolometer through the antenna. Isolating the source of the loading would be

informative. If the coupling is with the VCS2 stage, for example, the internal loading may exhibit notable temporal variation during flight.

The uniformity of device fabrication has reached the point that variation between TES' that share a common bias line does not significantly reduce the number of devices which may be simultaneously biased in their transition (§4.6). Further, the measured noise penalty due to the bias sharing is small. Device fabrication yield (usually limited by shorts to ground) is generally good. Improvements and experience with the wire bonding process have reduced the number of bond failures. At this point the most significant fabrication and packaging issue is simply a shortage of personnel given the monumental combined fabrication and assembly requirements of SPIDER and KECK. Important steps are being taken to shift responsibilities such as MUX screening and wire bonding out of the JPL work queue. Fabrication and assembly of each receiver takes less than a month, and can occur in parallel with testing of assembled telescopes.

As designed, SPIDER's bolometers achieve a safety factor of 4–5 on the Ti transition under the estimated loading for the 148 GHz band (§4.6). Some of this safety factor could, in principle, be traded to reduce phonon noise. However, G cannot be reduced without saturating the Al transition during lab testing, β has been driven down by the niobium added to the legs to reduce direct optical coupling to the island, and we have little control over T_c. The Al TES might be replaced by a higher T_c metal to relieve the lab saturation constraint, though this would likely be a significant development project. Alternatively, and perhaps less invasively, small alterations might be made to the Ti deposition process to learn more about how we might reduce T_c. However, at this point the receiver is not phonon noise dominated, so the rewards for such efforts are not likely to justify the distraction that they would present. In the near term, time will be better spent optimizing (perhaps diminishing) G for the 93 GHz band after the upcoming measurements of efficiency and loading in this new band. The $\sim$280 GHz band (not yet designed) will have a larger bandwidth and sky response than the 148 GHz band, so it may require a larger G.

Reducing noise (§4.7) should be a top priority as SPIDER moves forward. In particular, there is a need for better understanding of excess noise, amplifier noise, and aliasing. Progress has been made in this regard (led by Jeff Filippini), but more work will be required to reduce the aliased noise to a level comparable to phonon noise. In addition, continued study of cross talk and correlated signal mechanisms is certainly merited.

In §4.8 I quantified the expected detector response (and differential response) to variations in focal plane temperature and cold sleeve temperature. Tests should be undertaken to probe the response to changes in SSA temperature. We do not yet know what level of temperature stability we might expect in flight for any of these three stages. Retaining the option of PID temperature control of the focal planes would be desirable. The effects of optical loading and the slow exhaustion of the fridge cycle could be quantified using currently available data from the test cryostat, but understanding scan synchronous effects will require integration with the gondola. The calculated requirements for the thermal stability of the cold sleeve are fairly strict, and no thermal filtering is currently designed into this system. I recommend measurements of the response of this stage to microphonic excitation and to changes in optical loading. I strongly recommend pursuing the use of the Gaussian-tapered antenna feed network.

The measured response to external magnetic field modulation has been modeled in flight simulations, and is now at an acceptable level (§4.9). No additional shielding is required. The only step that I will recommend is modeling to ensure that the expected response of six telescopes integrated into the flight cryostat together is comparable or better than the expected response of the individual telescope inserts as measured in the SPIDER test cryostat.

The coming months will be very active as six flight receivers must be built and characterized prior to flight. The simulation effort is quickly expanding to set quantitative limits on various systematic effects associated with the actual measured performance of the instrument. SPIDER's major subsystems will continue to be sequentially integrated and tested together. This chapter primarily addresses the performance of receivers using metrics relevant to independent testing in the SPIDER test cryostat. Increasingly, the SPIDER team will be brought together in the coming months to characterize integrated systems. A shared understanding within the collaboration of each subsystem will be required for effective integration. This chapter summarized the combined efforts of the Caltech receiver team, and was designed to document those efforts for the benefit of the larger SPIDER collaboration.

Appendix A

Definitions and Methods

A.1 Optical Efficiency

Optical efficiency ($\eta(\nu)$) is a unitless measure of the fraction of the power incident on a device that is detected by the bolometer.

The radiated power from a pure black body is given by

$$P_{BB} = \int \frac{2h\nu^3}{c^2} \frac{1}{e^{\frac{h\nu}{kT}} - 1} d\nu dA d\Omega. \tag{A.1}$$

SPIDER's detectors are polarized, so we drop the factor of two when quantifying efficiency. For a single-mode diffraction-limited receiver, $\int dA d\Omega = c^2/\nu^2$. We thus define the optical efficiency such that the power absorbed by a device when viewing a beam filling black body of temperature T is

$$Q = \int \eta(\nu) \frac{h\nu}{e^{h\nu/kT} - 1} d\nu. \tag{A.2}$$

To derive optical efficiency we measure P_{Joule} on transition at a variety of different blackbody load temperatures. The focal plane temperature T_{sub} is kept nearly constant. From Equation 3.1,

$$\Delta Q = -\Delta P_{Joule} + \Delta P_{legs} \simeq -\Delta P_{Joule}. \tag{A.3}$$

Variations of T_{sub} within a data set are generally on order 0.1 mK, measured by the Cernox thermometer mounted on the focal plane or by silicon NTDs mounted on the detector tiles (thermometers in good agreement). The correction term ΔP_{legs} is therefore very small. Assuming $G_{450} = 17$ pW/K, $T_{sub} = 300$ mK and $\Delta T_{sub} = 0.1$ mK, it is on the order $|\Delta P_{legs}| = 0.001$ pW. I include this small correction in my calculations, but will drop it for

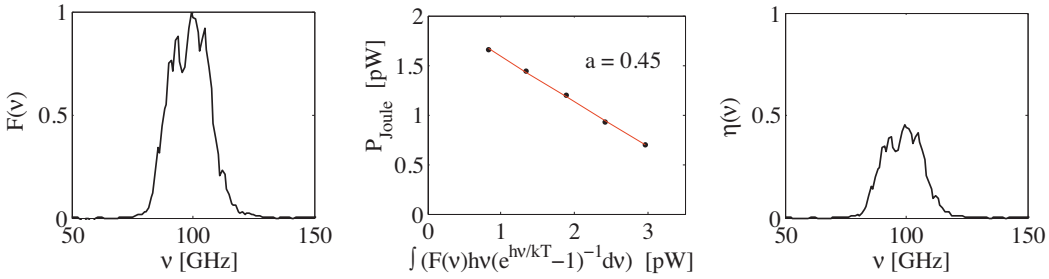

Figure A.1: (*Left*) $F(\nu)$ is measured by FTS, and arbitrarily normalized. (*Center*) A simple linear fit to the data taken at different load temperatures determines the normalization prefactor "a" according to Equation A.4. (*Right*) The calculated prefactor is used to normalize $F(\nu)$ to find $\eta(\nu)$.

the remainder of this section.

A complete measurement of optical efficiency requires passband measurements to define the spectral shape of $\eta(\nu)$. Fourier transform spectroscopy (§4.2) provides an unnormalized passband $F(\nu)$. Using Equations A.2 and A.3, we find

$$\eta(\nu) = aF(\nu) = -\frac{dP_{Joule}}{d\left(\int F(\nu)h\nu(e^{\frac{h\nu}{kT}}-1)^{-1}d\nu\right)}F(\nu). \tag{A.4}$$

The prefactor a is calculated by a simple linear fit to the data. As an example, in Figure A.1 I examine my measurements of the device designated by JAB080529 (3, 2, B).

In the event that spectroscopy is not available, I isolate the magnitude of the integrated optical response from the details of the spectral response by defining

$$\eta_0 \equiv \frac{\int \eta(\nu)d\nu}{0.25\nu_0}, \tag{A.5}$$

where ν_0 is the target band center. I choose this definition because the target bandwidth is 25%. Then

$$Q \simeq \eta_0 \int_{0.875\nu_0}^{1.125\nu_0} \frac{h\nu_0}{e^{h\nu_0/kT}-1}d\nu, \text{ and} \tag{A.6}$$

$$\eta_0 = -\frac{dP_{Joule}}{d\left(\int_{0.875\nu_0}^{1.125\nu_0} h\nu(e^{\frac{h\nu}{kT}}-1)^{-1}d\nu\right)}. \tag{A.7}$$

This is a good approximation assuming $h\nu/(e^{h\nu_0/kT}-1)$ does not vary significantly over

the passband, which is true unless there is significant response out of the primary band.

Sometimes we wish to express optical response with units of power over temperature. However, the absorbed power is not linearly related to the physical temperature. To work in these units we therefore instead convert the incident power in to a Rayleigh-Jeans "temperature," given by

$$T_{RJ} \equiv k^{-1}(0.25\nu_0)^{-1}\left(\int_{0.875\nu_0}^{1.125\nu_0} \frac{h\nu_0}{e^{h\nu_0/kT}-1}d\nu\right). \tag{A.8}$$

This is not an actual physical temperature. It corresponds to the temperature of the idealized Rayleigh-Jeans source ($h\nu \ll kT$) that would radiate the same amount of power in a 25% wide band around ν_0 as our actual blackbody source. Just as was done above, $|dP_{Joule}/dT_{RJ}|$ is calculated using a simple linear fit to the data (see, for example, Figure 4.17).

We often quote $|dP_{Joule}/dT_{RJ}|$ in tabulations of measured optical response. These values can be expressed in terms of η using

$$\eta_0 = (0.25\nu_0 k)^{-1}\left|\frac{dP_{Joule}}{dT_{RJ}}\right|, \text{ and} \tag{A.9}$$

$$\int \eta(\nu)d\nu = k^{-1}\left|\frac{dP_{Joule}}{dT_{RJ}}\right|. \tag{A.10}$$

A.2 Alternative Methods for Calculating Internal Loading

The More Robust Method

This technique uses all of the same data sets associated with the basic method and requires two additional data sets. Each additional data set consists of load curves taken at a variety of focal plane temperatures (∼10 different temperatures between the fridge base temperature and the device saturation temperature). One set is taken on a dark run ($Q \simeq 0$), and the other is taken on a cold load run at a constant (preferably low) cold load temperature. Each of these two data sets can be used to fit the parameters of thermal conductance (see Figure 3.12 for a reminder). The results should agree. For the cold load data, the constant

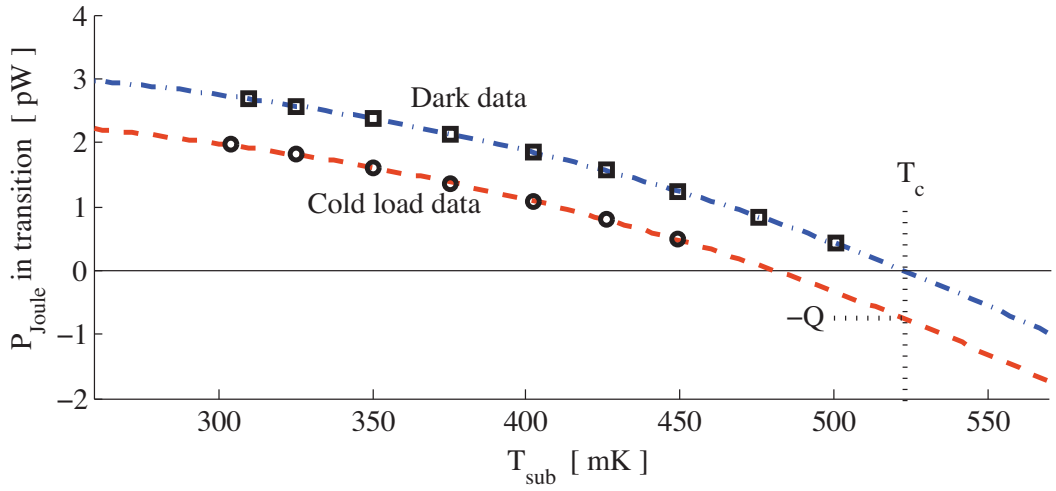

Figure A.2: The optical load Q absorbed by devices in the cold load configuration introduces a simple DC offset in P_{Joule} (independent of T_{sub}). The curve for the dark data intercepts the temperature axis at $T_{sub} = T_c$, so the projected P_{Joule} for the fit to the cold load data is $-Q$ at $T_{sub} = T_c$.

nonzero optical power introduces a simple DC offset in power ($-Q$).

$$\begin{aligned} P_{Joule} &= P_{legs} - Q \\ &= \frac{GT_0}{\beta+1}\left\{\left(\frac{T_c}{T_0}\right)^{\beta+1} - \left(\frac{T_{sub}}{T_0}\right)^{\beta+1}\right\} - Q \end{aligned} \tag{A.11}$$

We can extract Q from our thermal conductance fit for the cold load data (Figure A.2).

$$Q = -P_{Joule} \quad \text{for fit projection at } T_{sub} = T_c \tag{A.12}$$

A little algebra produces another equivalent expression for Q,

$$Q = \frac{GT_0}{\beta+1}\left[\left(\frac{T_c}{T_0}\right)^{\beta+1} - \left(\frac{T_i}{T_0}\right)^{\beta+1}\right], \tag{A.13}$$

where T_i is the temperature axis intercept for the curve fit to the cold load data.

The optical power Q is the sum of the loading from the cold load and the internal loading. We subtract the cold load contribution to calculate the internal loading,

$$Q_{int} = Q - \left(\frac{dP}{dT_{RJ}}\right) T_{\mathrm{ColdLoad},RJ}. \tag{A.14}$$

This alternative method reduces statistical errors by using ∼10× as much load curve data as the simple method. In addition, it greatly suppresses systematic errors due to small inaccuracies in electrical calibration factors (e.g., wiring resistances, SQUID gain) that may bias P_{Joule} in different ways from one run to the next. For example, a calibration uncertainty resulting in a 5% disagreement in powers between dark data and cold load data would result in an internal loading systematic error of $0.05{*}P_{Joule}$ (or about 0.15 pW) using the simple method. Using this alternative method the systematic error would simply scale the loading result, so the effect would be no more than 0.02 pW for optically coupled pixels and 0.002 pW for dark TES.

Without Dark Data

Generally, without dark data there is no way to break the degeneracy between internal loading and T_c. However, there are four dark TES (not coupled to antennas) on each tile. Dark TES exhibit very low internal loading (see Appendix B.10). Neglecting this small loading, we can calculate T_c for the dark TES using only cold load data. For dark TES, the correction due to optical response to the cold load is small (∼1 mK, see Appendix B.8), but we make it anyway.

$$T_c = \left[T_{i,dark}^{\beta+1} + \frac{T_0^{\beta}\,(\beta+1)}{G} \left| \frac{dP}{dT_{RJ}} \right|_{dark} T_{ColdLoad,RJ} \right]^{1/(\beta+1)} \tag{A.15}$$

The dark TES bolometers are fabricated in the same way as the optically coupled devices, so they should exhibit similar values of T_c. We can therefore, with some caution, take the average measured T_c for the dark devices and substitute it into Equation A.13 to calculate the loading Q for the optically active devices.

Appendix B

Measured Detector Parameters

In this Appendix I tabulate some of the measured device parameters of SPIDER engineering focal planes. "Run" is a sequential designation of cryogenic focal plane test programs. Each fabricated tile is afforded a designation delimiting the fabricator who produced it (JAB=Bonetti, T=Turner, K=Kenyon), the date of its completion (YYMMDD), and the order of completion on that day. Individual devices on a tile are designated by their physical location on the tile (column, row) as well as their polarization (A or B). See Figure B.1. When properties are catalogued for an entire tile, the median value is given.

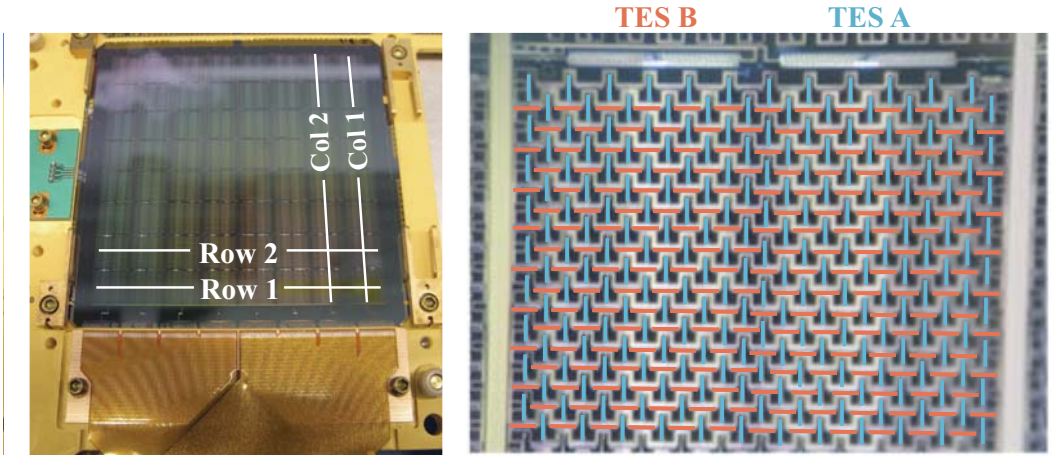

Figure B.1: *Left*: Convention for designating rows and columns on a tile. Row 1 is closest to the wire bond edge. Multiplexer coordinates are different from physical coordinates. Two physical columns are read out by each multiplexer column (4 mux columns per tile).
Right: TES B is connected to slots that are parallel to the wire bond edge of the tile, and responds to polarization perpendicular to the wire bond edge. TES A is connected to slots that are perpendicular to the wire bond edge, and responds to polarization parallel to the wire bond edge.

B.1 Aluminum TES T_c and R_n

Here I tabulate my measurements of the transition temperature (T_c) and normal state resistance (R_n) of the aluminum TES.

Run	Tile Designation	Median Al T_c [mK]	Median Al R_n [mΩ]
2.0	T100122.2	1330	556
2.0	JAB100104.1	1373	1111
2.0	JAB090323.1	1331	650

B.2 Titanium TES T_c and R_n

Here I tabulate the measured superconducting transition temperature (T_c) and normal state resistance (R_n) of the titanium TES. These values were calculated by me (Runs 1–4) and by Becky Tucker (Run 5). Starting in Run 5, the geometry of the Ti TES was intentionally redesigned to lower the normal resistance (to improve noise performance).

Run	Tile Designation	Median Ti T_c [mK]	Median Ti R_n [mΩ]
5.0	JAB110106.1	511	31
5.0	JAB110106.2	523	27
5.0	T110204.2	512	32
5.0	T110204.3	506	34
4.0	T100707.2	541	74
3.1	JAB100503.2	532	68
3.1	T10040505.7	521	46
3.1	JAB100316.1	508	88

Run	Tile Designation	Median Ti T_c [mK]	Median Ti R_n [mΩ]
2.0	T100122.2	N/A	74
2.0	JAB100104.1	N/A	68
2.0	JAB090323.1*	N/A	61
1.1	JAB090330.1	497	51
1.1	T090323.2	515	47
1.1	T090323.1	515	48
1.1	JAB090323.1*	501	55

* The discrepancy between Run 1 and 2 in measured resistance values for this tile is not understood, and may be the result of a calibration error in one of these early runs.

B.3 Leg Thermal Conductance

Here I tabulate the measured parameters quantifying the thermal conductance of the Si_3N_4 legs that isolate the bolometer islands (Equation 3.7). These values were calculated by me (Runs 1–4) and by Becky Tucker (Run 5) using the procedure described in §3.4. In Runs 2 and 3 some tiles were fabricated with an intentional mix of two different kinds of devices, designed to differ in G_{450} by a factor of two. Starting from Run 4, tiles have been intentionally fabricated with lower thermal conductance ($G_{450} \approx 16$ pW/K). At the beginning of 2010, we began to add a layer of niobium on the silicon nitride legs to reduce the direct coupling of radiation to the TES island. This had the effect of lowering β from about 2.5 to about 2.1. It is not our standard practice to measure the properties of the silicon nitride legs at Al transition temperatures (including G_{1340} and β), but we have measured them on several occasions. These parameters are not relevant to science operation, but do impact the saturation power (P_{sat}) of the aluminum transition, which affects our ability to make measurements with the window open to the room (300 K) and with the beams coupled to hot blackbody sources.

Run	Tile Designation	Median G_{450} [pW/K]	Median Ti G_c [pW/K]	Median β on Ti	Median G_{1340} [pW/K]	Median β on Al	Median Al P_{sat} [pW]
5.0	JAB110106.1	15	20	2.2	N/A		93
5.0	JAB110106.2	17	23	2.0	N/A		100
5.0	T110204.2	14	17	2.1	N/A		73
5.0	T110204.3	13	16	2.0	N/A		73
4.0	T100707.2	16	24	2.1	N/A		
3.1	JAB100503.2	30 | 16	43 | 23	2.2	N/A		
3.1	T10040505.7	28 | 14	38 | 19	2.1	N/A		
3.1	JAB100316.1	37 | 19	48 | 24	2.2	N/A		
2.0	T100122.2	35	N/A	2.0	484	2.5	181
2.0	JAB100104.1	32 | 16	N/A	2.3	505 | 251	2.5	208 | 103
2.0	JAB090323.1	26	N/A	2.5	443	2.6	164
1.1	JAB090330.1	24	31	2.6	N/A		
1.1	T090323.2	24	35	2.7	N/A		
1.1	T090323.1	19	28	2.5	N/A		
1.1	JAB090323.1	26	34	2.6	N/A		

B.4 TES Uniformity

SPIDER's readout is multiplexed. There is a single line biasing the 33 TES' in each multiplexer (mux) column. Uniformity is important so that a good bias can be chosen for each column such that all of the devices are in a stable and responsive part of their transition. Here I tabulate my measurements of the standard deviation of various device parameters. The quoted values are the yield-weighted averages of the standard deviations of the parameters within the four mux columns that read out the tile.

Run	Tile Designation	Ti T_c Average Mux Col σ/mean	Ti R_n Average Mux Col σ/mean	G_{450} Average Mux Col σ/mean	β Average Mux Col σ/mean
4.0	T100707.2	0.5%	10%	5%	2%
3.1	JAB100503.2	1.2%	8%	8%	2%
3.1	T10040505.7	1.4%	8%	6%	2%
3.1	JAB100316.1	0.8%	5%	4%	2%
2.0	T100122.2	N/A	8%	4%	5%
2.0	JAB100104.1	N/A	14%	2%	3%
1.1	JAB090330.1	0.9%	7%	13%	5%
1.1	T090323.2	0.8%	5%	6%	4%
1.1	T090323.1	0.6%	4%	6%	4%
1.1	JAB090323.1	1.3%	9%	4%	6%

Histograms and maps of T_c and R_n for a representative tile. The maps are in actual physical coordinates, with the two polarizations (A and B) shown in triangles.

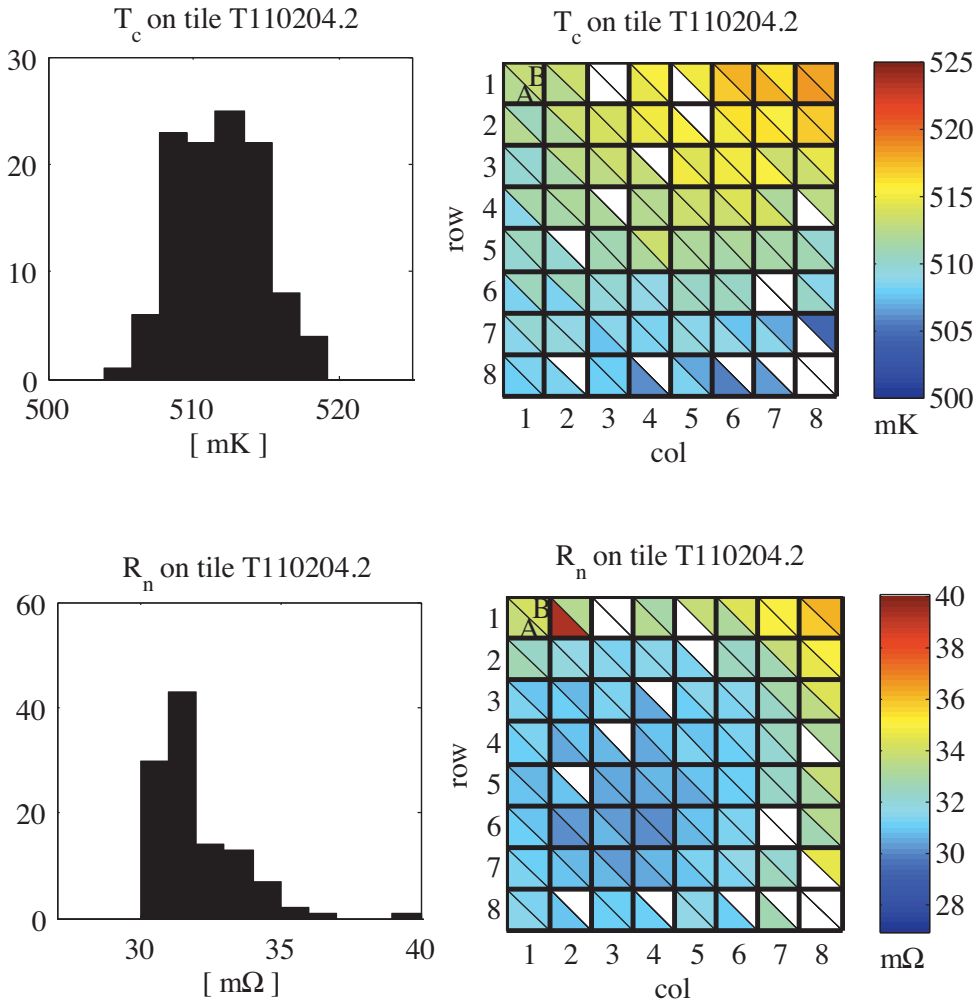

Histograms and maps of G_{450} and β for a representative tile. The maps are in actual physical coordinates, with the two polarizations (A and B) shown in triangles.

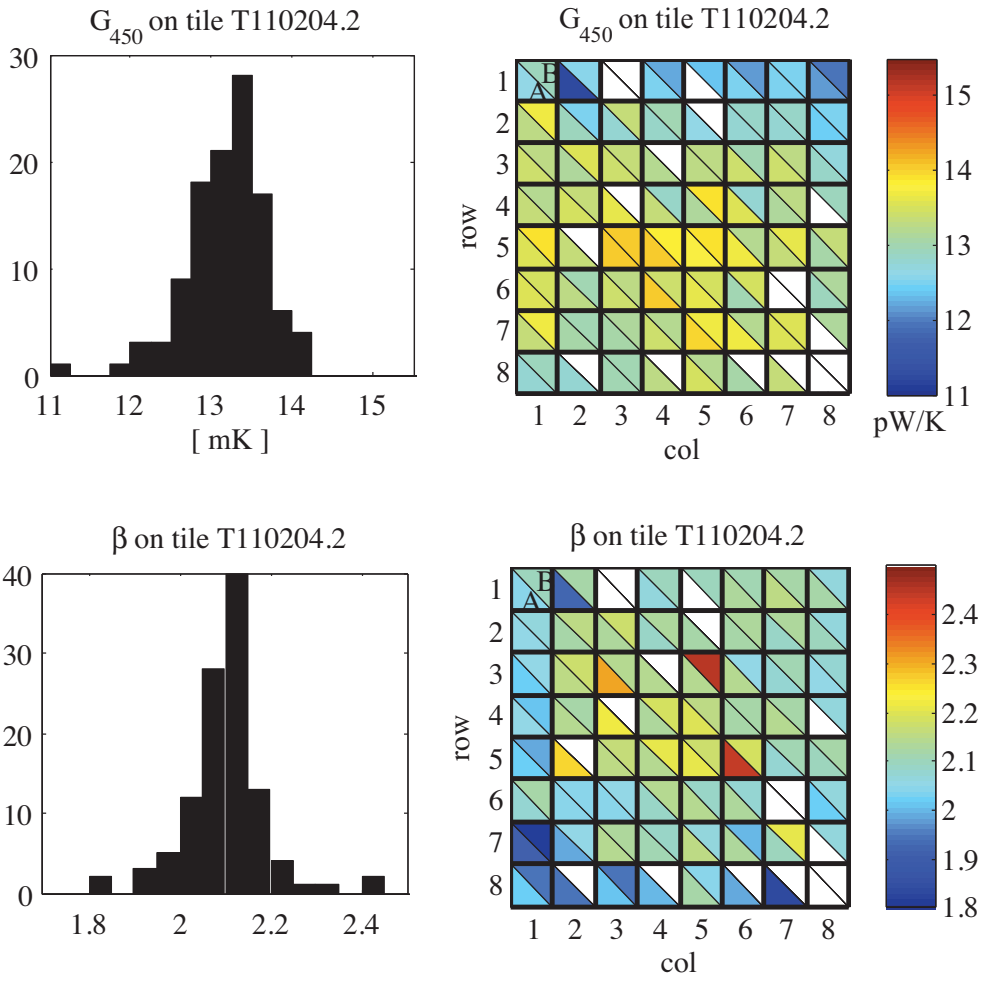

B.5 Optical Response of 145 GHz Devices (No Telescope)

Here I tabulate the optical response of individual 145 GHz devices from my measurements in the single-pixel optical test bed. This measurement coupled the antennas directly to a black body with no lenses and only minimal filtering.

Measured	Device Designation	η_0	dP/dT_{RJ} [pW/K$_{RJ}$]
07/31/09	JAB090310.1 (5, 2, A)	41%*	0.200*
07/26/08	JAB080312.2 (2, 2, A)	79%	0.385
07/26/08	” (2, 2, B)	74%	0.363
05/20/08	” (2, 6, A)	81%	0.396

* This device may had an 8 kΩ (warm) electrical short from antenna to ground plane.

B.6 Optical Response of 99 GHz Devices (No Telescope)

Here I tabulate the optical response of individual 99 GHz devices from my measurements in the single-pixel optical test bed. This measurement coupled the antennas directly to a black body with no lenses and only minimal filtering. There is notable (unexplained) variation in response between the different tiles. Devices from K080114.1 have <10% more bandwidth than the other wafers; not nearly enough to explain the difference in response.

Measured	Device Designation	η_0	dP/dT_{RJ} [pW/K$_{RJ}$]
07/31/09	JAB081205.1 (4, 2, B)	42%†	0.139†
04/14/09	” (4, 5, A)	38%	0.126
12/18/08	” (4, 2, A)	47%	0.153
10/06/08	JAB080529 (3, 2, B)	38%	0.124
08/21/08	K080114.1 (3, 2, A)	59%	0.193
08/21/08	” (3, 2, B)	58%	0.191
06/26/08	” (3, 3, A)	58%	0.191

† This device was measured differently from the others. Looking out of the cryostat window, aluminum TES load curves were taken viewing the 300 K room and then a 77 K LN_2 bath.

B.7 Optical Response of 148 GHz Tiles Through Telescope

Here I tabulate the median optical response of 148 GHz tiles coupled through telescope optics in the SPIDER test cryostat. These values were calculated by Jeff Fillippini (Runs 1, 5) and by me (Runs 2, 3) using the procedure described in §4.4.

Run	Tile Designation	η_0	Median dP/dT_{RJ} [pW/K$_{RJ}$]	Avg. Mux Column σ/mean
5.1	JAB110106.1*	2%	0.010	N/A
5.1	JAB110106.2*	2%	0.009	N/A
5.1	T110204.2*	30%	0.150	N/A
5.1	T110204.3*	1%	0.005	N/A
3.0	JAB100503.2†	19%	0.095	18%
3.0	T10040505.7	34%	0.172	16%
3.0	JAB100316.1	35%	0.180	20%
2.0	JAB100104.1	33%	0.162	22%
2.0	JAB090323.1‡	31%	0.156	10%
1.3	JAB090330.1	22%	0.111	N/A
1.3	T090323.2	23%	0.115	N/A
1.3	T090323.1	23%	0.113	N/A
1.3	JAB090323.1‡	24%	0.119	N/A

* Over etching with XeF_2 attacked the Nb microstrip ground plane on these tiles.

† SiO_2 ILD ICP-HD-PECVD (inductively coupled plasma, high density plasma enhanced chemical vapor deposition). This was an experimental ILD deposition process, and is no longer used.

‡ The discrepancy between Run 1 and 2 in measured optical response for this tile is not understood, and may be the result of either improved efficiency of the optical train or a calibration error in one of these early runs (see B.2).

B.8 Optical Response of Dark TES Through Telescope

Here I tabulate the optical response of dark TES (not coupled to antennas) in the SPIDER test cryostat. These values were calculated by Jeff Fillippini (Runs 1, 5) and by me (Runs 2, 3) using the procedure described in §4.4.

Run	Device Designation	dP/dT_{RJ} [pW/K$_{RJ}$]
5.1	T110204.2 (1, 1, A)	0.0027
5.1	T110204.2 (1, 1, B)	0.0036
5.1	T110204.2 (8, 1, A)	0.0037
5.1	T110204.2 (8, 1, B)	0.0037

Run	Device Designation	dP/dT_{RJ} [pW/K$_{RJ}$]
3.0	JAB100503.2 (1, 1, A)	0.0037
3.0	T10040505.7 (1, 1, B)	0.0018
3.0	” (8, 1, A)	0.0034
3.0	” (8, 1, B)	0.0036
3.0	JAB100316.1 (1, 1, B)	0.0034
3.0	” (8, 1, A)	0.0035
3.0	” (8, 1, B)	0.0034
2.0	JAB100104.1 (1, 1, B)	0.0021
2.0	” (8, 1, A)	0.0023
2.0	” (8, 1, B)	0.0021
2.0	JAB090323.1* (8, 1, A)	0.0035
2.0	” (8, 1, B)	0.0030
1.3	T090323.2 (1, 1, B)	0.0037
1.3	T090323.1 (1, 1, B)	0.0035
1.3	” (8, 1, B)	0.0028
1.3	JAB090323.1* (1, 1, B)	0.0037
1.3	” (8, 1, A)	0.0040
1.3	” (8, 1, B)	0.0042

B.9 Internal Loading of Telescope (148 GHz Tiles)

Here I tabulate the median internal loading of 148 GHz tiles from measurements in the SPIDER test bed described in §4.5. These values were calculated by Jeff Fillippini (Run 1) and by me (Runs 2–5). There are two main components of internal loading. One is associated with direct coupling of radiation to the TES and is experienced by all devices, including dark TES (see Appendix B.10). The other is associated with antenna pickup and is linearly correlated with the optical response dP/dT_{RJ}. A figure of merit quantifying the strength of this second (much larger) signal is catalogued in the last column of the table. This figure of merit decreased in Run 3 when the cold sleeve was added. It decreased again in Run 5, perhaps due to the removal of on optical fiber intended to port optical signals to the focal plane from an IR diode mounted on VCS2 (80 K).

Run	Tile Designation	Median Loading [pW]	Avg. Mux Column σ/mean	$\frac{IL-IL_{dark}}{dP/dT_{RJ}}$ [K_{RJ}]
5.1	T110204.2	0.41	4%	2.6
5.1	T110204.3	0.41	7%	2.6
3.1	JAB100503.2	0.38	8%	3.0
3.1	T10040505.7	0.56	6%	2.9
3.1	JAB100316.1	0.63	7%	3.1
2.0	JAB090323.1	0.73	N/A	3.8
1.3	JAB090330.1	0.52	N/A	4.3
1.3	T090323.2	0.51	N/A	4.1
1.3	T090323.1	0.49	N/A	4.0
1.3	JAB090323.1	0.50	N/A	3.8

B.10 Internal Loading Measured By Dark TES

Here I tabulate the internal loading of dark TES (not coupled to antennas) from measurements in the SPIDER test bed described in §4.5. These values were calculated by Jeff Fillippini (Run 1) and by me (Runs 2–5). This component of the loading is believed to be associated with direct coupling of radiation to the TES. It increased in Run 2 when we inadvertently failed to install the 12 cm^{-1} high pass filter in the optical train. Between Runs 2 and 3 the TES island geometry was changed to reduce this coupling, However, dark TES loading was elevated again in Run 3, perhaps by the optical fiber installed in that run to port optical signals to the focal plane from an IR diode mounted on VCS2 (80 K). In Run 5 this fiber had been removed and dark TES loading was found to be at the level of only ∼0.01 pW.

Run	Device Designation	Loading [pW]
5.1	T110204.2 (1, 1, A)	0.01
5.1	T110204.2 (1, 1, B)	0.03
5.1	T110204.2 (8, 1, A)	0.01
5.1	T110204.2 (8, 1, B)	0.01

Run	Device Designation	Loading [pW]
3.0	JAB100503.2 (1, 1, A)	0.09
3.0	T10040505.7 (1, 1, B)	0.06
3.0	” (8, 1, A)	0.06
3.0	JAB100316.1 (1, 1, B)	0.06
3.0	” (8, 1, A)	0.07
3.0	” (8, 1, B)	0.07
2.0	JAB090323.1[b] (8, 1, A)	0.13
2.0	” (8, 1, B)	0.13
1.3	T090323.1 (8, 1, B)	0.06
1.3	JAB090323.1[b] (1, 1, B)	0.04
1.3	” (8, 1, A)	0.02
1.3	” (8, 1, B)	0.05

B.11 Tile to Tile Band Center Uniformity

99 GHz Band Centers

Band centers of five individual devices measured in the single-pixel optical test bed using Fourier transform spectroscopy. One full 99 GHz tile was measured in the SPIDER test cryostat coupled through 148 GHz optimized optics. The dispersion between different tiles is a couple of GHz. Since these tiles were fabricated, the filter has been intentionally changed to lower the target band center by 6% from 99 to 93 GHz.

Measured	Device Designation	Band Center [GHz]
Run 2.1	JAB100107.1 *Tile Average*	99
12/18/08	JAB081205.1 (5, 3, B)	96
07/26/08	JAB080529 (3, 2, B)	99
01/28/08	K080114.1 (3, 1, A)	100
01/28/08	” (3, 1, B)	98
06/26/08	” (3, 2, B)	97

145 GHz Band Centers

Band centers of individual devices measured in the single-pixel optical test bed using Fourier transform spectroscopy. The dispersion between different tiles is a couple of GHz. Since these tiles were fabricated, the ILD thickness has been intentionally changed to raise the target band center by 2% from 145 to 148 GHz.

Measured	Device Designation	Band Center [GHz]
05/18/09	JAB090310.1 (8, 5, B)	144
04/15/08	JAB080312.2 (2, 4, A)	149
04/15/08	” (2, 4, B)	150
10/06/07	T070611.1 (?, ?, B)*	146
09/20/07	” (?, ?, A)*	147
09/20/07	” (?, ?, B)*	146

* These devices were not labelled by row and column at fabrication delivery

Bibliography

[1] P. A. R. Ade, G. Pisano, C. Tucker, and S. Weaver. A review of metal mesh filters. *Society of Photo-Optical Instrumentation Engineers (SPIE) Conference Series*, 6275, July 2006.

[2] R. W. Aikin, P. A. Ade, S. Benton, J. J. Bock, J. A. Bonetti, J. A. Brevik, C. D. Dowell, L. Duband, J. P. Filippini, S. R. Golwala, M. Halpern, V. V. Hristov, K. Irwin, J. P. Kaufman, B. G. Keating, J. M. Kovac, C.-L. Kuo, A. E. Lange, C. B. Netterfield, H. T. Nguyen, R. W. Ogburn, IV, A. Orlando, C. Pryke, S. Richter, J. E. Ruhl, M. C. Runyan, C. Sheehy, S. A. Stokes, R. Sudiwala, G. P. Teply, J. E. Tolan, A. D. Turner, P. Wilson, and C. L. Wong. Optical performance of the BICEP2 Telescope at the South Pole. *Society of Photo-Optical Instrumentation Engineers (SPIE) Conference Series*, 7741, July 2010.

[3] A. Albrecht and P. J. Steinhardt. Cosmology for grand unified theories with radiatively induced symmetry breaking. *Physical Review Letters*, 48(17):1220–1223, Apr 1982.

[4] R. A. Alpher, H. Bethe, and G. Gamow. The Origin of Chemical Elements. *Physical Review*, 73:803–804, April 1948.

[5] R. A. Alpher and R. Herman. Evolution of the Universe. *Nature*, 162:774–775, November 1948.

[6] M. A. Alvarez, V. Bromm, and P. R. Shapiro. The H II Region of the First Star. *Astrophysical Journal*, 639:621–632, March 2006.

[7] J. Bardeen, L. N. Cooper, and J. R. Schrieffer. Theory of superconductivity. *Physical Review*, 108(5):1175–1204, Dec 1957.

[8] R. Barkana and A. Loeb. In the beginning: the first sources of light and the reionization of the universe. *Physics Reports*, 349:125–238, July 2001.

[9] E. S. Battistelli, M. Amiri, B. Burger, M. J. Devlin, S. R. Dicker, W. B. Doriese, R. Dünner, R. P. Fisher, J. W. Fowler, M. Halpern, M. Hasselfield, G. C. Hilton, A. D. Hincks, K. D. Irwin, M. Kaul, J. Klein, S. Knotek, J. M. Lau, M. Limon, T. A. Marriage, M. D. Niemack, L. Page, C. D. Reintsema, S. T. Staggs, D. S. Swetz, E. R. Switzer, R. J. Thornton, and Y. Zhao. Automated SQUID tuning procedure for kilo-pixel arrays of TES bolometers on the Atacama Cosmology Telescope. *Society of Photo-Optical Instrumentation Engineers (SPIE) Conference Series*, 7020, August 2008.

[10] E. S. Battistelli, M. Amiri, B. Burger, M. Halpern, S. Knotek, M. Ellis, X. Gao, D. Kelly, M. Macintosh, K. Irwin, and C. Reintsema. Functional Description of Read-out Electronics for Time-Domain Multiplexed Bolometers for Millimeter and Sub-millimeter Astronomy. *Journal of Low Temperature Physics*, 151:908–914, May 2008.

[11] D. Baumann, M. G. Jackson, P. Adshead, A. Amblard, A. Ashoorioon, N. Bartolo, R. Bean, M. Beltrán, F. de Bernardis, S. Bird, X. Chen, D. J. H. Chung, L. Colombo, A. Cooray, P. Creminelli, S. Dodelson, J. Dunkley, C. Dvorkin, R. Easther, F. Finelli, R. Flauger, M. P. Hertzberg, K. Jones-Smith, S. Kachru, K. Kadota, J. Khoury, W. H. Kinney, E. Komatsu, L. M. Krauss, J. Lesgourgues, A. Liddle, M. Liguori, E. Lim, A. Linde, S. Matarrese, H. Mathur, L. McAllister, A. Melchiorri, A. Nicolis, L. Pagano, H. V. Peiris, M. Peloso, L. Pogosian, E. Pierpaoli, A. Riotto, U. Seljak, L. Senatore, S. Shandera, E. Silverstein, T. Smith, P. Vaudrevange, L. Verde, B. Wandelt, D. Wands, S. Watson, M. Wyman, A. Yadav, W. Valkenburg, and M. Zaldarriaga. Probing Inflation with CMB Polarization. *American Institute of Physics Conference Series*, 1141:10–120, June 2009.

[12] R. H. Becker, X. Fan, R. L. White, M. A. Strauss, V. K. Narayanan, R. H. Lupton, J. E. Gunn, J. Annis, N. A. Bahcall, J. Brinkmann, A. J. Connolly, I. Csabai, P. C. Czarapata, M. Doi, T. M. Heckman, G. S. Hennessy, Ž. Ivezić, G. R. Knapp, D. Q. Lamb, T. A. McKay, J. A. Munn, T. Nash, R. Nichol, J. R. Pier, G. T. Richards,

D. P. Schneider, C. Stoughton, A. S. Szalay, A. R. Thakar, and D. G. York. Evidence for Reionization at z∼6: Detection of a Gunn-Peterson Trough in a z=6.28 Quasar. *Astrophysical Journal*, 122:2850–2857, December 2001.

[13] A. Benoît, P. Ade, A. Amblard, R. Ansari, É. Aubourg, S. Bargot, J. G. Bartlett, J.-P. Bernard, R. S. Bhatia, A. Blanchard, J. J. Bock, A. Boscaleri, F. R. Bouchet, A. Bourrachot, P. Camus, F. Couchot, P. de Bernardis, J. Delabrouille, F.-X. Désert, O. Doré, M. Douspis, L. Dumoulin, X. Dupac, P. Filliatre, P. Fosalba, K. Ganga, F. Gannaway, B. Gautier, M. Giard, Y. Giraud-Héraud, R. Gispert, L. Guglielmi, J.-C. Hamilton, S. Hanany, S. Henrot-Versillé, J. Kaplan, G. Lagache, J.-M. Lamarre, A. E. Lange, J. F. Macías-Pérez, K. Madet, B. Maffei, C. Magneville, D. P. Marrone, S. Masi, F. Mayet, A. Murphy, F. Naraghi, F. Nati, G. Patanchon, G. Perrin, M. Piat, N. Ponthieu, S. Prunet, J.-L. Puget, C. Renault, C. Rosset, D. Santos, A. Starobinsky, I. Strukov, R. V. Sudiwala, R. Teyssier, M. Tristram, C. Tucker, J.-C. Vanel, D. Vibert, E. Wakui, and D. Yvon. First detection of polarization of the submillimetre diffuse galactic dust emission by Archeops. *Astronomy and Astrophysics*, 424:571–582, September 2004.

[14] J. Bernstein. *Miss Leavitt's Stars: The Untold Story of the Woman Who Discovered How to Measure the Universe*. W. W. Norton & Company, New York, 2005.

[15] B. Bertotti, L. Iess, and P. Tortora. A test of general relativity using radio links with the Cassini spacecraft. *Nature*, 425:374–376, September 2003.

[16] J. J. Bock, A. Aljabri, A. Amblard, D. Baumann, M. Betoule, T. Chui, L. Colombo, A. Cooray, D. Crumb, P. Day, C. Dickinson, D. Dowell, M. Dragovan, S. Golwala, K. Gorski, S. Hanany, W. Holmes, K. Irwin, B. Johnson, B. Keating, C.-L. Kuo, A. Lee, A. Lange, C. Lawrence, S. Meyer, N. Miller, H. Nguyen, E. Pierpaoli, N. Ponthieu, J.-L. Puget, J. Raab, P. Richards, C. Satter, M. Seiffert, M. Shimon, H. Tran, B. Williams, and J. Zmuidzinas. Study of the Experimental Probe of Inflationary Cosmology (EPIC)-Intemediate Mission for NASA's Einstein Inflation Probe. *ArXiv e-prints*, astro-ph/0906.1188, June 2009.

[17] J. J. Bock, J. Gundersen, A. T. Lee, P. L. Richards, and E. Wollack. Optical coupling. *Journal of Physics Conference Series*, 155(1):012005–+, March 2009.

[18] J. A. Bonetti, P. K. Day, M. Kenyon, C.-L. Kuo, A. Turner, H. G. Leduc, and J. J. Bock. Characterization of Antenna-Coupled TES Bolometers for the Spider Experiment. *IEEE Transactions on Applied Superconductivity*, 19:520–523, June 2009.

[19] J. A. Bonetti, A. D. Turner, M. Kenyon, A. Orlando, J. A. Brevik, A. Trangsrud, R. Sudiwala, H. G. Leduc, H. T. Nguyen, P. K. Day, J. J. Bock, S. R. Golwala, J. Sayers, J. M. Kovac, A. E. Lange, W. C. Jones, and C.-L. Kuo. Microfabrication and Device Parameter Testing of the Focal Plane Arrays for the Spider and BICEP2/Keck CMB Polarimeters. *American Institute of Physics Conference Series*, 1185:367–370, December 2009.

[20] L. A. Boyle, P. J. Steinhardt, and N. Turok. Inflationary Predictions for Scalar and Tensor Fluctuations Reconsidered. *Physical Review Letters*, 96(11):111301–+, March 2006.

[21] R. H. Brandenberger. Quantum field theory methods and inflationary universe models. *Reviews of Modern Physics*, 57:1–60, January 1985.

[22] J. A. Brevik, R. W. Aikin, M. Amiri, S. J. Benton, J. J. Bock, J. A. Bonetti, B. Burger, C. D. Dowell, L. Duband, J. P. Filippini, S. R. Golwala, M. Halpern, M. Hasselfield, G. Hilton, V. V. Hristov, K. Irwin, J. P. Kaufman, B. G. Keating, J. M. Kovac, C.-L. Kuo, A. E. Lange, E. M. Leitch, C. B. Netterfield, H. T. Nguyen, R. W. Ogburn, IV, A. Orlando, C. Pryke, C. Reintsema, S. Richter, J. E. Ruhl, M. Runyan, C. Sheehy, Z. Staniszewski, R. Sudiwala, J. E. Tolan, A. D. Turner, P. Wilson, and C. L. Wong. Initial performance of the BICEP2 antenna-coupled superconducting bolometers at the South Pole. *Society of Photo-Optical Instrumentation Engineers (SPIE) Conference Series*, 7741, July 2010.

[23] G. Brumfiel. Physics: The waiting game. *Nature*, 429:10–11, May 2004.

[24] S. Bryan. Email to A. Trangsrud with attachment, February 2010.

[25] S. A. Bryan, P. A. R. Ade, M. Amiri, S. Benton, R. Bihary, J. J. Bock, J. R. Bond, J. A. Bonetti, H. C. Chiang, C. R. Contaldi, B. P. Crill, D. O'Dea, O. Dore, M. Farhang, J. P. Filippini, L. Fissel, N. Gandilo, S. Golwala, J. E. Gudmundsson, M. Hasselfield, M. Halpern, K. R. Helson, G. Hilton, W. Holmes, V. V. Hristov, K. D. Irwin, W. C.

Jones, C.-L. Kuo, C. J. MacTavish, P. Mason, T. Morford, T. E. Montroy, C. B. Netterfield, A. S. Rahlin, C. D. Reintsema, D. Riley, J. E. Ruhl, M. C. Runyan, M. A. Schenker, J. Shariff, J. D. Soler, A. Transrud, R. Tucker, C. Tucker, and A. Turner. Modeling and characterization of the SPIDER half-wave plate. *Society of Photo-Optical Instrumentation Engineers (SPIE) Conference Series*, 7741, July 2010.

[26] S. A. Bryan, T. E. Montroy, and J. E. Ruhl. Modeling dielectric half-wave plates for CMB polarimetry using a Mueller matrix formalism. *ArXiv e-prints*, astro-ph/1006.3359, June 2010.

[27] H. C. Chiang, P. A. R. Ade, D. Barkats, J. O. Battle, E. M. Bierman, J. J. Bock, C. D. Dowell, L. Duband, E. F. Hivon, W. L. Holzapfel, V. V. Hristov, W. C. Jones, B. G. Keating, J. M. Kovac, C.-L. Kuo, A. E. Lange, E. M. Leitch, P. V. Mason, T. Matsumura, H. T. Nguyen, N. Ponthieu, C. Pryke, S. Richter, G. Rocha, C. Sheehy, Y. D. Takahashi, J. E. Tolan, and K. W. Yoon. Measurement of Cosmic Microwave Background Polarization Power Spectra from Two Years of BICEP Data. *Astrophysical Journal*, 711:1123–1140, March 2010.

[28] J. Clarke and A. I. Braginski. *The SQUID Handbook, Volume 1: Fundamentals and Technology of SQUIDs and SQUID Systems*. Wiley-VCH, Weinheim, Germany, 2004.

[29] P. Coles and F. Lucchin. *Cosmology: The Origin and Evolution of Cosmic Structure*. John Wiley & Sons, New York, 2002.

[30] J. J. Condon and S. M. Ransom. Molecular line spectra. http://www.cv.nrao.edu/course/astr534/MolecularSpectra.html, accessed 5/28/11.

[31] B. P. Crill, P. A. R. Ade, D. R. Artusa, R. S. Bhatia, J. J. Bock, A. Boscaleri, P. Cardoni, S. E. Church, K. Coble, P. de Bernardis, G. de Troia, P. Farese, K. M. Ganga, M. Giacometti, C. V. Haynes, E. Hivon, V. V. Hristov, A. Iacoangeli, W. C. Jones, A. E. Lange, L. Martinis, S. Masi, P. V. Mason, P. D. Mauskopf, L. Miglio, T. Montroy, C. B. Netterfield, C. G. Paine, E. Pascale, F. Piacentini, G. Polenta, F. Pongetti, G. Romeo, J. E. Ruhl, F. Scaramuzzi, D. Sforna, and A. D. Turner. BOOMERANG: A Balloon-borne Millimeter-Wave Telescope and Total Power Receiver for Mapping Anisotropy in the Cosmic Microwave Background. *Astrophysical Journal Supplement Series*, 148:527–541, October 2003.

[32] B. P. Crill, P. A. R. Ade, E. S. Battistelli, S. Benton, R. Bihary, J. J. Bock, J. R. Bond, J. Brevik, S. Bryan, C. R. Contaldi, O. Doré, M. Farhang, L. Fissel, S. R. Golwala, M. Halpern, G. Hilton, W. Holmes, V. V. Hristov, K. Irwin, W. C. Jones, C.-L. Kuo, A. E. Lange, C. Lawrie, C. J. MacTavish, T. G. Martin, P. Mason, T. E. Montroy, C. B. Netterfield, E. Pascale, D. Riley, J. E. Ruhl, M. C. Runyan, A. Trangsrud, C. Tucker, A. Turner, M. Viero, and D. Wiebe. SPIDER: a balloon-borne large-scale CMB polarimeter. *Society of Photo-Optical Instrumentation Engineers (SPIE) Conference Series*, 7010, August 2008.

[33] P. Day. Email to J. J. Bock with attachment, August 2009.

[34] P. de Bernardis, P. A. R. Ade, J. J. Bock, J. R. Bond, J. Borrill, A. Boscaleri, K. Coble, B. P. Crill, G. De Gasperis, P. C. Farese, P. G. Ferreira, K. Ganga, M. Giacometti, E. Hivon, V. V. Hristov, A. Iacoangeli, A. H. Jaffe, A. E. Lange, L. Martinis, S. Masi, P. V. Mason, P. D. Mauskopf, A. Melchiorri, L. Miglio, T. Montroy, C. B. Netterfield, E. Pascale, F. Piacentini, D. Pogosyan, S. Prunet, S. Rao, G. Romeo, J. E. Ruhl, F. Scaramuzzi, D. Sforna, and N. Vittorio. A flat Universe from high-resolution maps of the cosmic microwave background radiation. *Nature*, 404:955–959, April 2000.

[35] P. A. J. de Korte, J. Beyer, S. Deiker, G. C. Hilton, K. D. Irwin, M. Macintosh, S. W. Nam, C. D. Reintsema, L. R. Vale, and M. E. Huber. Time-division superconducting quantum interference device multiplexer for transition-edge sensors. *Review of Scientific Instruments*, 74:3807–3815, August 2003.

[36] R. de Putter, O. Zahn, and E. V. Linder. CMB lensing constraints on neutrinos and dark energy. *Physical Review D*, 79(6):065033–+, March 2009.

[37] R. H. Dicke, P. J. E. Peebles, P. G. Roll, and D. T. Wilkinson. Cosmic Black-Body Radiation. *Astrophysical Journal*, 142:414–419, July 1965.

[38] S. G. Djorgovski, S. Castro, D. Stern, and A. A. Mahabal. On the Threshold of the Reionization Epoch. *Astrophysical Journal Letters*, 560:L5–L8, October 2001.

[39] B. T. Draine and A. A. Fraisse. Polarized Far-Infrared and Submillimeter Emission from Interstellar Dust. *Astrophysical Journal*, 696:1–11, May 2009.

[40] J. Dunkley, A. Amblard, C. Baccigalupi, M. Betoule, D. Chuss, A. Cooray, J. Delabrouille, C. Dickinson, G. Dobler, J. Dotson, H. K. Eriksen, D. Finkbeiner, D. Fixsen, P. Fosalba, A. Fraisse, C. Hirata, A. Kogut, J. Kristiansen, C. Lawrence, A. M. Magalha˜Es, M. A. Miville-Deschenes, S. Meyer, A. Miller, S. K. Naess, L. Page, H. V. Peiris, N. Phillips, E. Pierpaoli, G. Rocha, J. E. Vaillancourt, and L. Verde. Prospects for polarized foreground removal. *American Institute of Physics Conference Series*, 1141:222–264, June 2009.

[41] F. W. Dyson, A. S. Eddington, and C. Davidson. A Determination of the Deflection of Light by the Sun's Gravitational Field, from Observations Made at the Total Eclipse of May 29, 1919. *Royal Society of London Philosophical Transactions Series A*, 220:291–333, 1920.

[42] J. P. Filippini, P. A. R. Ade, M. Amiri, S. J. Benton, R. Bihary, J. J. Bock, J. R. Bond, J. A. Bonetti, S. A. Bryan, B. Burger, H. C. Chiang, C. R. Contaldi, B. P. Crill, O. Doré, M. Farhang, L. M. Fissel, N. N. Gandilo, S. R. Golwala, J. E. Gudmundsson, M. Halpern, M. Hasselfield, G. Hilton, W. Holmes, V. V. Hristov, K. D. Irwin, W. C. Jones, C.-L. Kuo, C. J. MacTavish, P. V. Mason, T. E. Montroy, T. A. Morford, C. B. Netterfield, D. T. O'Dea, A. S. Rahlin, C. D. Reintsema, J. E. Ruhl, M. C. Runyan, M. A. Schenker, J. A. Shariff, J. D. Soler, A. Trangsrud, C. Tucker, R. S. Tucker, and A. D. Turner. SPIDER: a balloon-borne CMB polarimeter for large angular scales. *Society of Photo-Optical Instrumentation Engineers (SPIE) Conference Series*, 7741, July 2010.

[43] D. P. Finkbeiner, M. Davis, and D. J. Schlegel. Extrapolation of Galactic Dust Emission at 100 Microns to Cosmic Microwave Background Radiation Frequencies Using FIRAS. *Astrophysical Journal*, 524:867–886, October 1999.

[44] D. P. Finkbeiner and D. J. Schlegel. Interstellar Dust Emission as a CMB Foreground. *Astronomical Society of the Pacific Conference Series*, 181:101–+, 1999.

[45] A. A. Fraisse, P. A. R. Ade, M. Amiri, S. J. Benton, J. J. Bock, J. R. Bond, J. A. Bonetti, S. Bryan, B. Burger, H. C. Chiang, C. N. Clark, C. R. Contaldi, B. P. Crill, G. Davis, O. Doré, M. Farhang, J. P. Filippini, L. M. Fissel, N. N. Gandilo, S. Golwala, J. E. Gudmundsson, M. Hasselfield, G. Hilton, W. Holmes, V. V. Hristov,

K. Irwin, W. C. Jones, C.-L. Kuo, C. J. MacTavish, P. V. Mason, T. E. Montroy, T. A. Morford, C. B. Netterfield, D. T. O'Dea, A. S. Rahlin, C. Reintsema, J. E. Ruhl, M. C. Runyan, M. A. Schenker, J. A. Shariff, J. D. Soler, A. Trangsrud, C. Tucker, R. S. Tucker, A. D. Turner, and D. Wiebe. SPIDER: Probing the Early Universe with a Suborbital Polarimeter. *ArXiv e-prints*, astro-ph/1106.3087, June 2011.

[46] A. Friedman. Über die Krümmung des Raumes. *Zeitschrift fur Physik*, 10:377–386, December 1922.

[47] A. Friedman. On the Curvature of Space. *General Relativity and Gravitation*, 31:1991–+, December 1999.

[48] F. Gardiol. *Microstrip Circuits*. John Wiley & Sons, New York, 1994.

[49] B. Gold, N. Odegard, J. L. Weiland, R. S. Hill, A. Kogut, C. L. Bennett, G. Hinshaw, X. Chen, J. Dunkley, M. Halpern, N. Jarosik, E. Komatsu, D. Larson, M. Limon, S. S. Meyer, M. R. Nolta, L. Page, K. M. Smith, D. N. Spergel, G. S. Tucker, E. Wollack, and E. L. Wright. Seven-year Wilkinson Microwave Anisotropy Probe (WMAP) Observations: Galactic Foreground Emission. *Astrophysical Journal Supplement Series*, 192:15–+, February 2011.

[50] A. Goldin, J. J. Bock, A. E. Lange, H. Leduc, A. Vayonakis, and J. Zmuidzinas. Antennas for bolometric focal plane. *Nuclear Instruments and Methods in Physics Research A*, 520:390–392, March 2004.

[51] P. F. Goldsmith. *Quasioptical Systems: Gaussian Beam Quasioptical Propogation and Applications*. IEEE Press, 1998.

[52] J. E. Gudmundsson, P. A. R. Ade, M. Amiri, S. J. Benton, R. Bihary, J. J. Bock, J. R. Bond, J. A. Bonetti, S. A. Bryan, B. Burger, H. C. Chiang, C. R. Contaldi, B. P. Crill, O. Doré, M. Farhang, J. Filippini, L. M. Fissel, N. N. Gandilo, S. R. Golwala, M. Halpern, M. Hasselfield, G. Hilton, W. Holmes, V. V. Hristov, K. D. Irwin, W. C. Jones, C.-L. Kuo, C. J. MacTavish, P. V. Mason, T. E. Montroy, T. A. Morford, C. B. Netterfield, D. T. O'Dea, A. S. Rahlin, C. D. Reintsema, J. E. Ruhl, M. C. Runyan, M. A. Schenker, J. A. Shariff, J. D. Soler, A. Trangsrud, C. Tucker, R. S. Tucker,

and A. D. Turner. Thermal architecture for the SPIDER flight cryostat. *Society of Photo-Optical Instrumentation Engineers (SPIE) Conference Series*, 7741, July 2010.

[53] S. Gupta, P. Ade, J. J. Bock, M. Bowden, M. L. Brown, G. Cahill, P. G. Castro, S. Church, T. Culverhouse, R. B. Friedman, K. Ganga, W. K. Gear, J. Hinderks, J. Kovac, A. E. Lange, E. Leitch, S. J. Melhuish, Y. Memari, J. A. Murphy, A. Orlando, C. O'Sullivan, L. Piccirillo, C. Pryke, N. Rajguru, B. Rusholme, R. Schwarz, A. N. Taylor, K. L. Thompson, A. H. Turner, E. Y. S. Wu, M. Zemcov, and QUaD Collaboration. Parameter Estimation from Improved Measurements of the Cosmic Microwave Background from QUaD. *Astrophysical Journal*, 716:1040–1046, June 2010.

[54] A. H. Guth. Inflationary universe: A possible solution to the horizon and flatness problems. *Physical Review D*, 23:347–356, January 1981.

[55] A. H. Guth. *The Inflationary Universe*. Addison-Wesley, Boston, 1997.

[56] E. Haller, K. M. Itoh, J. W. Beeman, W. L. Hansen, and V. I. Ozhogin. Neutron Transmutation Doped Natural and Isotopically Engineered Germanium Thermistors. *The SPIE Symposium on Astronomical Telescopes and Instrumentation for the 21st Century*, 2198:630–637, March 1994.

[57] S. Hanany and P. Rosenkranz. Polarization of the atmosphere as a foreground for cosmic microwave background polarization experiments. *New Astronomy Reviews*, 47:1159–1165, December 2003.

[58] G. Hinshaw, J. L. Weiland, R. S. Hill, N. Odegard, D. Larson, C. L. Bennett, J. Dunkley, B. Gold, M. R. Greason, N. Jarosik, E. Komatsu, M. R. Nolta, L. Page, D. N. Spergel, E. Wollack, M. Halpern, A. Kogut, M. Limon, S. S. Meyer, G. S. Tucker, and E. L. Wright. Five-Year Wilkinson Microwave Anisotropy Probe Observations: Data Processing, Sky Maps, and Basic Results. *Astrophysical Journal Supplement Series*, 180:225–245, February 2009.

[59] F. Hoyle. *The Nature of the Universe*. Harper, New Yor], 1950.

[60] W. Hu and M. White. A CMB polarization primer. *New Astronomy*, 2:323–344, October 1997.

[61] E. Hubble. A Relation between Distance and Radial Velocity among Extra-Galactic Nebulae. *Proceedings of the National Academy of Science*, 15:168–173, March 1929.

[62] E. P. Hubble. NGC 6822, a remote stellar system. *Astrophysical Journal*, 62:409–433, December 1925.

[63] K. D. Irwin. An application of electrothermal feedback for high resolution cryogenic particle detection. *Applied Physics Letters*, 66:1998–2000, April 1995.

[64] K. D. Irwin and G. C. Hilton. Transition-edge sensors. In C. Enss, editor, *Cryogenic Particle Detection*, pages 63–150. Springer, 2005.

[65] J. B. Johnson. Thermal Agitation of Electricity in Conductors. *Physical Review*, 32:97–109, July 1928.

[66] W. C. Jones, R. S. Bhatia, J. J. Bock, and A. E. Lange. A Polarization Sensitive Bolometric Detector for Observations of the Cosmic Microwave Background. *ArXiv e-prints*, astro-ph/0209132, September 2002.

[67] M. Kamionkowski, A. Kosowsky, and A. Stebbins. A Probe of Primordial Gravity Waves and Vorticity. *Physical Review Letters*, 78:2058–2061, March 1997.

[68] M. Kamionkowski, A. Kosowsky, and A. Stebbins. Statistics of cosmic microwave background polarization. *Physical Review D*, 55:7368–7388, June 1997.

[69] M. Kaplinghat, M. Chu, Z. Haiman, G. P. Holder, L. Knox, and C. Skordis. Probing the Reionization History of the Universe using the Cosmic Microwave Background Polarization. *Astrophysical Journal*, 583:24–32, January 2003.

[70] B. Keating, P. Timbie, A. Polnarev, and J. Steinberger. Large Angular Scale Polarization of the Cosmic Microwave Background Radiation and the Feasibility of Its Detection. *Astrophysical Journal*, 495:580–+, March 1998.

[71] R. Keisler, C. L. Reichardt, K. A. Aird, B. A. Benson, L. E. Bleem, J. E. Carlstrom, C. L. Chang, H. M. Cho, T. M. Crawford, A. T. Crites, T. de Haan, M. A. Dobbs, J. Dudley, E. M. George, N. W. Halverson, G. P. Holder, W. L. Holzapfel, S. Hoover, Z. Hou, J. D. Hrubes, M. Joy, L. Knox, A. T. Lee, E. M. Leitch, M. Lueker, D. Luong-Van, J. J. McMahon, J. Mehl, S. S. Meyer, M. Millea, J. J. Mohr, T. E.

Montroy, T. Natoli, S. Padin, T. Plagge, C. Pryke, J. E. Ruhl, K. K. Schaffer, L. Shaw, E. Shirokoff, H. G. Spieler, Z. Staniszewski, A. A. Stark, K. Story, A. van Engelen, K. Vanderlinde, J. D. Vieira, R. Williamson, and O. Zahn. A Measurement of the Damping Tail of the Cosmic Microwave Background Power Spectrum with the South Pole Telescope. *ArXiv e-prints*, astro-ph/1105.3182, May 2011.

[72] W. H. Kinney. Constraining inflation with cosmic microwave background polarization. *Physical Review D*, 58(12):123506–+, December 1998.

[73] E. Komatsu, K. M. Smith, J. Dunkley, C. L. Bennett, B. Gold, G. Hinshaw, N. Jarosik, D. Larson, M. R. Nolta, L. Page, D. N. Spergel, M. Halpern, R. S. Hill, A. Kogut, M. Limon, S. S. Meyer, N. Odegard, G. S. Tucker, J. L. Weiland, E. Wollack, and E. L. Wright. Seven-year Wilkinson Microwave Anisotropy Probe (WMAP) Observations: Cosmological Interpretation. *Astrophysical Journal Supplement Series*, 192:18–+, February 2011.

[74] J. M. Kovac, E. M. Leitch, C. Pryke, J. E. Carlstrom, N. W. Halverson, and W. L. Holzapfel. Detection of polarization in the cosmic microwave background using DASI. *Nature*, 420:772–787, December 2002.

[75] C.-L. Kuo, J. J. Bock, J. A. Bonetti, J. Brevik, G. Chattopadhyay, P. K. Day, S. Golwala, M. Kenyon, A. E. Lange, H. G. LeDuc, H. Nguyen, R. W. Ogburn, A. Orlando, A. Trangsrud, A. Turner, G. Wang, and J. Zmuidzinas. Antenna-coupled TES bolometer arrays for CMB polarimetry. *Society of Photo-Optical Instrumentation Engineers (SPIE) Conference Series*, 7020, August 2008.

[76] C.-L. Kuo, J. J. Bock, G. Chattopadthyay, A. Goldin, S. Golwala, W. Holmes, K. Irwin, M. Kenyon, A. E. Lange, H. G. LeDuc, P. Rossinot, A. Vayonakis, G. Wang, M. Yun, and J. Zmuidzinas. Antenna-coupled TES bolometers for CMB polarimetry. *Society of Photo-Optical Instrumentation Engineers (SPIE) Conference Series*, 6275, July 2006.

[77] J.-M. Lamarre, J.-L. Puget, P. A. R. Ade, F. Bouchet, G. Guyot, A. E. Lange, F. Pajot, A. Arondel, K. Benabed, J.-L. Beney, A. Benoît, J.-P. Bernard, R. Bhatia, Y. Blanc, J. J. Bock, E. Bréelle, T. W. Bradshaw, P. Camus, A. Catalano, J. Charra,

M. Charra, S. E. Church, F. Couchot, A. Coulais, B. P. Crill, M. R. Crook, K. Dassas, P. de Bernardis, J. Delabrouille, P. de Marcillac, J.-M. Delouis, F.-X. Désert, C. Dumesnil, X. Dupac, G. Efstathiou, P. Eng, C. Evesque, J.-J. Fourmond, K. Ganga, M. Giard, R. Gispert, L. Guglielmi, J. Haissinski, S. Henrot-Versillé, E. Hivon, W. A. Holmes, W. C. Jones, T. C. Koch, H. Lagardère, P. Lami, J. Landé, B. Leriche, C. Leroy, Y. Longval, J. F. Macías-Pérez, T. Maciaszek, B. Maffei, B. Mansoux, C. Marty, S. Masi, C. Mercier, M.-A. Miville-Deschênes, A. Moneti, L. Montier, J. A. Murphy, J. Narbonne, M. Nexon, C. G. Paine, J. Pahn, O. Perdereau, F. Piacentini, M. Piat, S. Plaszczynski, E. Pointecouteau, R. Pons, N. Ponthieu, S. Prunet, D. Rambaud, G. Recouvreur, C. Renault, I. Ristorcelli, C. Rosset, D. Santos, G. Savini, G. Serra, P. Stassi, R. V. Sudiwala, J.-F. Sygnet, J. A. Tauber, J.-P. Torre, M. Tristram, L. Vibert, A. Woodcraft, V. Yurchenko, and D. Yvon. Planck pre-launch status: The HFI instrument, from specification to actual performance. *Astronomy and Astrophysics*, 520:A9+, September 2010.

[78] A. E. Lange, P. A. Ade, J. J. Bock, J. R. Bond, J. Borrill, A. Boscaleri, K. Coble, B. P. Crill, P. de Bernardis, P. Farese, P. Ferreira, K. Ganga, M. Giacometti, E. Hivon, V. V. Hristov, A. Iacoangeli, A. H. Jaffe, L. Martinis, S. Masi, P. D. Mauskopf, A. Melchiorri, T. Montroy, C. B. Netterfield, E. Pascale, F. Piacentini, D. Pogosyan, S. Prunet, S. Rao, G. Romeo, J. E. Ruhl, F. Scaramuzzi, and D. Sforna. Cosmological parameters from the first results of Boomerang. *Physical Review D*, 63(4):042001–+, February 2001.

[79] D. Larson, J. Dunkley, G. Hinshaw, E. Komatsu, M. R. Nolta, C. L. Bennett, B. Gold, M. Halpern, R. S. Hill, N. Jarosik, A. Kogut, M. Limon, S. S. Meyer, N. Odegard, L. Page, K. M. Smith, D. N. Spergel, G. S. Tucker, J. L. Weiland, E. Wollack, and E. L. Wright. Seven-year Wilkinson Microwave Anisotropy Probe (WMAP) Observations: Power Spectra and WMAP-derived Parameters. *Astrophysical Journal Supplement Series*, 192:16–+, February 2011.

[80] H. S. Leavitt. 1777 variables in the Magellanic Clouds. *Annals of Harvard College Observatory*, 60:87–108, 1908.

[81] G. Lemaître. Un Univers homogène de masse constante et de rayon croissant rendant compte de la vitesse radiale des nébuleuses extra-galactiques. *Annales de la Societe Scietifique de Bruxelles*, 47:49–59, 1927.

[82] G. Lemaître. Expansion of the universe, A homogeneous universe of constant mass and increasing radius accounting for the radial velocity of extra-galactic nebulæ. *Monthly Notices of the Royal Astronomical Society*, 91:483–490, March 1931.

[83] A. R. Liddle and D. H. Lyth. COBE, gravitational waves, inflation and extended inflation. *Physics Letters B*, 291:391–398, October 1992.

[84] A. R. Liddle and D. H. Lyth. *Cosmological Inflation and Large-Scale Structure*. Cambridge University Press, Cambridge, 2000.

[85] D. R. Lide. *CRC Handbook of Chemistry and Physics, 88th Edition*. CRC Press, Boca Raton, Florida, June 2007.

[86] A. D. Linde. A new inflationary universe scenario: A possible solution of the horizon, flatness, homogeneity, isotropy and primordial monopole problems. *Physics Letters B*, 108:389–393, February 1982.

[87] L. Linde. *Particle Physics and Inflationary Cosmology*. CRC Press, Boca Raton, Florida, 1990. Translated from the Russian by M. Damashek.

[88] C. J. MacTavish, P. A. R. Ade, E. S. Battistelli, S. Benton, R. Bihary, J. J. Bock, J. R. Bond, J. Brevik, S. Bryan, C. R. Contaldi, B. P. Crill, O. Doré, L. Fissel, S. R. Golwala, M. Halpern, G. Hilton, W. Holmes, V. V. Hristov, K. Irwin, W. C. Jones, C.-L. Kuo, A. E. Lange, C. Lawrie, T. G. Martin, P. Mason, T. E. Montroy, C. B. Netterfield, D. Riley, J. E. Ruhl, M. Runyan, A. Trangsrud, C. Tucker, A. Turner, M. Viero, and D. Wiebe. Spider Optimization: Probing the Systematics of a Large-Scale B-Mode Experiment. *Astrophysical Journal*, 689:655–665, December 2008.

[89] C. J. MacTavish, P. A. R. Ade, J. J. Bock, J. R. Bond, J. Borrill, A. Boscaleri, P. Cabella, C. R. Contaldi, B. P. Crill, P. de Bernardis, G. De Gasperis, A. de Oliveira-Costa, G. De Troia, G. di Stefano, E. Hivon, A. H. Jaffe, W. C. Jones, T. S. Kisner, A. E. Lange, A. M. Lewis, S. Masi, P. D. Mauskopf, A. Melchiorri, T. E. Montroy,

P. Natoli, C. B. Netterfield, E. Pascale, F. Piacentini, D. Pogosyan, G. Polenta, S. Prunet, S. Ricciardi, G. Romeo, J. E. Ruhl, P. Santini, M. Tegmark, M. Veneziani, and N. Vittorio. Cosmological Parameters from the 2003 Flight of BOOMERANG. *Astrophysical Journal*, 647:799–812, August 2006.

[90] S. Masi, P. A. R. Ade, J. J. Bock, J. R. Bond, J. Borrill, A. Boscaleri, P. Cabella, C. R. Contaldi, B. P. Crill, P. de Bernardis, G. de Gasperis, A. de Oliveira-Costa, G. de Troia, G. di Stefano, P. Ehlers, E. Hivon, V. Hristov, A. Iacoangeli, A. H. Jaffe, W. C. Jones, T. S. Kisner, A. E. Lange, C. J. MacTavish, C. Marini Bettolo, P. Mason, P. D. Mauskopf, T. E. Montroy, F. Nati, L. Nati, P. Natoli, C. B. Netterfield, E. Pascale, F. Piacentini, D. Pogosyan, G. Polenta, S. Prunet, S. Ricciardi, G. Romeo, J. E. Ruhl, P. Santini, M. Tegmark, E. Torbet, M. Veneziani, and N. Vittorio. Instrument, method, brightness, and polarization maps from the 2003 flight of BOOMERanG. *Astronomy and Astrophysics*, 458:687–716, November 2006.

[91] J. C. Mather. Bolometer noise: nonequilibrium thoery. *Applied Optics*, 21:1125–1129, March 1982.

[92] J. C. Mather, E. S. Cheng, R. E. Eplee, Jr., R. B. Isaacman, S. S. Meyer, R. A. Shafer, R. Weiss, E. L. Wright, C. L. Bennett, N. W. Boggess, E. Dwek, S. Gulkis, M. G. Hauser, M. Janssen, T. Kelsall, P. M. Lubin, S. H. Moseley, Jr., T. L. Murdock, R. F. Silverberg, G. F. Smoot, and D. T. Wilkinson. A preliminary measurement of the cosmic microwave background spectrum by the Cosmic Background Explorer (COBE) satellite. *Astrophysical Journal Letters*, 354:L37–L40, May 1990.

[93] J. J. McMahon, K. A. Aird, B. A. Benson, L. E. Bleem, J. Britton, J. E. Carlstrom, C. L. Chang, H. S. Cho, T. de Haan, T. M. Crawford, A. T. Crites, A. Datesman, M. A. Dobbs, W. Everett, N. W. Halverson, G. P. Holder, W. L. Holzapfel, D. Hrubes, K. D. Irwin, M. Joy, R. Keisler, T. M. Lanting, A. T. Lee, E. M. Leitch, A. Loehr, M. Lueker, J. Mehl, S. S. Meyer, J. J. Mohr, T. E. Montroy, M. D. Niemack, C. C. Ngeow, V. Novosad, S. Padin, T. Plagge, C. Pryke, C. Reichardt, J. E. Ruhl, K. K. Schaffer, L. Shaw, E. Shirokoff, H. G. Spieler, B. Stadler, A. A. Stark, Z. Staniszewski, K. Vanderlinde, J. D. Vieira, G. Wang, R. Williamson, V. Yefremenko, K. W. Yoon,

O. Zhan, and A. Zenteno. SPTpol: an instrument for CMB polarization. *American Institute of Physics Conference Series*, 1185:511–514, December 2009.

[94] A. Miller, J. Beach, S. Bradley, R. Caldwell, H. Chapman, M. J. Devlin, W. B. Dorwart, T. Herbig, D. Jones, G. Monnelly, C. B. Netterfield, M. Nolta, L. A. Page, J. Puchalla, T. Robertson, E. Torbet, H. T. Tran, and W. E. Vinje. The QMAP and MAT/TOCO Experiments for Measuring Anisotropy in the Cosmic Microwave Background. *Astrophysical Journal Supplement Series*, 140:115–141, June 2002.

[95] D. T. O'Dea, P. A. R. Ade, M. Amiri, S. J. Benton, J. J. Bock, J. R. Bond, J. A. Bonetti, S. Bryan, B. Burger, H. C. Chiang, C. N. Clark, C. R. Contaldi, B. P. Crill, G. Davis, O. Dore, M. Farhang, J. P. Filippini, L. M. Fissel, A. A. Fraisse, N. N. Gandilo, S. Golwala, J. E. Gudmundsson, M. Hasselfield, G. Hilton, W. Holmes, V. V. Hristov, K. Irwin, W. C. Jones, C.-L. Kuo, C. J. MacTavish, P. V. Mason, T. E. Montroy, T. A. Morford, C. B. Netterfield, A. S. Rahlin, C. Reintsema, J. E. Ruhl, M. C. Runyan, M. A. Schenker, J. A. Shariff, J. D. Soler, A. Trangsrud, C. Tucker, R. S. Tucker, A. D. Turner, and D. Wiebe. Spider Optimization II: Optical, Magnetic and Foreground Effects. *ArXiv e-prints*, astro-ph/1102.0559, February 2011.

[96] R. W. Ogburn, IV, P. A. R. Ade, R. W. Aikin, M. Amiri, S. J. Benton, J. J. Bock, J. A. Bonetti, J. A. Brevik, B. Burger, C. D. Dowell, L. Duband, J. P. Filippini, S. R. Golwala, M. Halpern, M. Hasselfield, G. Hilton, V. V. Hristov, K. Irwin, J. P. Kaufman, B. G. Keating, J. M. Kovac, C.-L. Kuo, A. E. Lange, E. M. Leitch, C. B. Netterfield, H. T. Nguyen, A. Orlando, C. L. Pryke, C. Reintsema, S. Richter, J. E. Ruhl, M. C. Runyan, C. D. Sheehy, Z. K. Staniszewski, S. A. Stokes, R. V. Sudiwala, G. P. Teply, J. E. Tolan, A. D. Turner, P. Wilson, and C. L. Wong. The BICEP2 CMB polarization experiment. *Society of Photo-Optical Instrumentation Engineers (SPIE) Conference Series*, 7741, July 2010.

[97] L. Page, G. Hinshaw, E. Komatsu, M. R. Nolta, D. N. Spergel, C. L. Bennett, C. Barnes, R. Bean, O. Doré, J. Dunkley, M. Halpern, R. S. Hill, N. Jarosik, A. Kogut, M. Limon, S. S. Meyer, N. Odegard, H. V. Peiris, G. S. Tucker, L. Verde, J. L. Weiland, E. Wollack, and E. L. Wright. Three-Year Wilkinson Microwave Anisotropy

Probe (WMAP) Observations: Polarization Analysis. *Astrophysical Journal Supplement Series*, 170:335–376, June 2007.

[98] J. R. Pardo, J. Cernicharo, and E. Serabyn. Atmospheric transmission at microwaves (ATM): an improved model for millimeter/submillimeter applications. *IEEE Transactions on Antennas and Propagation*, 49:1683–1694, December 2001.

[99] P. J. E. Peebles. Recombination of the Primeval Plasma. *Astrophysical Journal*, 153:1–+, July 1968.

[100] A. A. Penzias and R. W. Wilson. A Measurement of Excess Antenna Temperature at 4080 Mc/s. *Astrophysical Journal*, 142:419–421, July 1965.

[101] Planck HFI Core Team, P. A. R. Ade, N. Aghanim, R. Ansari, M. Arnaud, M. Ashdown, J. Aumont, A. J. Banday, M. Bartelmann, J. G. Bartlett, E. Battaner, K. Benabed, A. Benoît, J. P. Bernard, M. Bersanelli, J. J. Bock, J. R. Bond, J. Borrill, F. R. Bouchet, F. Boulanger, T. Bradshaw, M. Bucher, J. F. Cardoso, G. Castex, A. Catalano, A. Challinor, A. Chamballu, R. R. Chary, X. Chen, C. Chiang, S. Church, D. L. Clements, J. M. Colley, S. Colombi, F. Couchot, A. Coulais, C. Cressiot, B. P. Crill, M. Crook, P. de Bernardis, J. Delabrouille, J. M. Delouis, F. X. Désert, K. Dolag, H. Dole, O. Doré, M. Douspis, J. Dunkley, G. Efstathiou, C. Filliard, O. Forni, P. Fosalba, K. Ganga, M. Giard, D. Girard, Y. Giraud-Héraud, R. Gispert, K. M. Górski, S. Gratton, M. Griffin, G. Guyot, J. Haissinski, D. Harrison, G. Helou, S. Henrot-Versillé, C. Hernández-Monteagudo, S. R. Hildebrandt, R. Hills, E. Hivon, M. Hobson, W. A. Holmes, K. M. Huffenberger, A. H. Jaffe, W. C. Jones, J. Kaplan, R. Kneissl, L. Knox, M. Kunz, G. Lagache, J. M. Lamarre, A. E. Lange, A. Lasenby, A. Lavabre, C. R. Lawrence, M. Le Jeune, C. Leroy, J. Lesgourgues, A. Lewis, J. F. Macías-Pérez, C. J. MacTavish, B. Maffei, N. Mandolesi, R. Mann, F. Marleau, D. J. Marshall, S. Masi, T. Matsumura, I. McAuley, P. McGehee, J. B. Melin, C. Mercier, S. Mitra, M. S. Miville-Deschênes, A. Moneti, L. Montier, D. Mortlock, A. Murphy, F. Nati, C. B. Netterfield, H. U. Nørgaard-Nielsen, C. North, F. Noviello, D. Novikov, S. Osborne, F. Pajot, G. Patanchon, T. Peacocke, T. J. Pearson, O. Perdereau, L. Perotto, F. Piacentini, M. Piat, S. Plaszczynski, E. Pointecouteau, N. Ponthieu, G. Prézeau, S. Prunet, J. L. Puget, W. T. Reach, M. Remazeilles, C. Renault, A. Riazuelo, I. Ris-

torcelli, G. Rocha, C. Rosset, G. Roudier, M. Rowan-Robinson, B. Rusholme, R. Saha, D. Santos, G. Savini, B. M. Schaefer, P. Shellard, L. Spencer, J. L. Starck, V. Stolyarov, R. Stompor, R. Sudiwala, R. Sunyaev, D. Sutton, J. F. Sygnet, J. A. Tauber, C. Thum, J. P. Torre, F. Touze, M. Tristram, F. Van Leeuwen, L. Vibert, D. Vibert, B. D. Wandelt, S. D. M. White, H. Wiesemeyer, A. Woodcraft, V. Yurchenko, D. Yvon, and A. Zacchei. Planck Early Results: The High Frequency Instrument data processing. *ArXiv e-prints*, astro-ph/1101.2048, January 2011.

[102] D. M Pozar. *Microwave Engineering, 3rd ed.* John Wiley & Sons, New York, 2005.

[103] QUIET Collaboration, C. Bischoff, A. Brizius, I. Buder, Y. Chinone, K. Cleary, R. N. Dumoulin, A. Kusaka, R. Monsalve, S. K. Næss, L. B. Newburgh, R. Reeves, K. M. Smith, I. K. Wehus, J. A. Zuntz, J. T. L. Zwart, L. Bronfman, R. Bustos, S. E. Church, C. Dickinson, H. K. Eriksen, P. G. Ferreira, T. Gaier, J. O. Gundersen, M. Hasegawa, M. Hazumi, K. M. Huffenberger, M. E. Jones, P. Kangaslahti, D. J. Kapner, C. R. Lawrence, M. Limon, J. May, J. J. McMahon, A. D. Miller, H. Nguyen, G. W. Nixon, T. J. Pearson, L. Piccirillo, S. J. E. Radford, A. C. S. Readhead, J. L. Richards, D. Samtleben, M. Seiffert, M. C. Shepherd, S. T. Staggs, O. Tajima, K. L. Thompson, K. Vanderlinde, R. Williamson, and B. Winstein. First Season QUIET Observations: Measurements of CMB Polarization Power Spectra at 43 GHz in the Multipole Range $25 \leq l \leq 475$. *ArXiv e-prints*, astro-ph/1012.3191, December 2010.

[104] B. Rabii, C. D. Winant, J. S. Collins, A. T. Lee, P. L. Richards, M. E. Abroe, S. Hanany, B. R. Johnson, P. Ade, A. Balbi, J. J. Bock, J. Borrill, R. Stompor, A. Boscaleri, E. Pascale, P. de Bernardis, P. G. Ferreira, V. V. Hristov, A. E. Lange, A. H. Jaffe, C. B. Netterfield, G. F. Smoot, and J. H. P. Wu. MAXIMA: A balloon-borne cosmic microwave background anisotropy experiment. *Review of Scientific Instruments*, 77(7):071101–+, July 2006.

[105] P. L. Richards. Bolometric Detectors for Measurements of the Cosmic Microwave Background. *Journal of Superconductivity*, 17:545–550, October 2004.

[106] P. G. Roll and D. T. Wilkinson. Cosmic Background Radiation at 3.2 cm-Support for Cosmic Black-Body Radiation. *Physical Review Letters*, 16:405–407, March 1966.

[107] M. C. Runyan, P. A. R. Ade, M. Amiri, S. Benton, R. Bihary, J. J. Bock, J. R. Bond, J. A. Bonetti, S. A. Bryan, H. C. Chiang, C. R. Contaldi, B. P. Crill, O. Dore, D. O'Dea, M. Farhang, J. P. Filippini, L. Fissel, N. Gandilo, S. R. Golwala, J. E. Gudmundsson, M. Hasselfield, M. Halpern, G. Hilton, W. Holmes, V. V. Hristov, K. D. Irwin, W. C. Jones, C.-L. Kuo, C. J. MacTavish, P. V. Mason, T. A. Morford, T. E. Montroy, C. B. Netterfield, A. S. Rahlin, C. D. Reintsema, J. E. Ruhl, M. A. Schenker, J. Shariff, J. D. Soler, A. Trangsrud, R. S. Tucker, C. E. Tucker, and A. Turner. Design and performance of the SPIDER instrument. *Society of Photo-Optical Instrumentation Engineers (SPIE) Conference Series*, 7741, July 2010.

[108] M. C. Runyan and R. Aikin. Email to A. Trangsrud with attachment, November 2009.

[109] G. B. Rybicki and A. P. Lightman. *Radiative Processes in Astrophysics*. Wiley-VCH, Weinheim, Germany, 2004.

[110] C. D. Sheehy, P. A. R. Ade, R. W. Aikin, M. Amiri, S. Benton, C. Bischoff, J. J. Bock, J. A. Bonetti, J. A. Brevik, B. Burger, C. D. Dowell, L. Duband, J. P. Filippini, S. R. Golwala, M. Halpern, M. Hasselfield, G. Hilton, V. V. Hristov, K. Irwin, J. P. Kaufman, B. G. Keating, J. M. Kovac, C.-L. Kuo, A. E. Lange, E. M. Leitch, M. Lueker, C. B. Netterfield, H. T. Nguyen, R. W. Ogburn, IV, A. Orlando, C. L. Pryke, C. Reintsema, S. Richter, J. E. Ruhl, M. C. Runyan, Z. Staniszewski, S. Stokes, R. Sudiwala, G. Teply, K. L. Thompson, J. E. Tolan, A. D. Turner, P. Wilson, and C. L. Wong. The Keck Array: a pulse tube cooled CMB polarimeter. *Society of Photo-Optical Instrumentation Engineers (SPIE) Conference Series*, 7741, July 2010.

[111] V. M. Slipher. Spectrographic Observations of Nebulae. *Popular Astronomy*, 23:21–24, January 1915.

[112] K. M. Smith, W. Hu, and M. Kaplinghat. Cosmological information from lensed CMB power spectra. *Physical Review D*, 74(12):123002–+, December 2006.

[113] G. F. Smoot, C. L. Bennett, A. Kogut, E. L. Wright, J. Aymon, N. W. Boggess, E. S. Cheng, G. de Amici, S. Gulkis, M. G. Hauser, G. Hinshaw, P. D. Jackson, M. Janssen, E. Kaita, T. Kelsall, P. Keegstra, C. Lineweaver, K. Loewenstein, P. Lubin, J. Mather,

S. S. Meyer, S. H. Moseley, T. Murdock, L. Rokke, R. F. Silverberg, L. Tenorio, R. Weiss, and D. T. Wilkinson. Structure in the COBE differential microwave radiometer first-year maps. *Astrophysical Journal Letters*, 396:L1–L5, September 1992.

[114] Caltech SPIDER team. Test cryostat analysis logbook. http://spiderwiki.princeton.edu/spider/AnalysisLogbook/TestCryostat/.

[115] G. M. Stiehl, H. M. Cho, G. C. Hilton, K. D. Irwin, J. A. B. Mates, C. D. Reintsema, and B. L. Zink. Time-Division SQUID Multiplexers With Reduced Sensitivity to External Magnetic Fields. *IEEE Transactions on Applied Superconductivity*, 21:298–301, June 2011.

[116] Y. D. Takahashi, P. A. R. Ade, D. Barkats, J. O. Battle, E. M. Bierman, J. J. Bock, H. C. Chiang, C. D. Dowell, L. Duband, E. F. Hivon, W. L. Holzapfel, V. V. Hristov, W. C. Jones, B. G. Keating, J. M. Kovac, C.-L. Kuo, A. E. Lange, E. M. Leitch, P. V. Mason, T. Matsumura, H. T. Nguyen, N. Ponthieu, C. Pryke, S. Richter, G. Rocha, and K. W. Yoon. Characterization of the BICEP Telescope for High-precision Cosmic Microwave Background Polarimetry. *Astrophysical Journal*, 711:1141–1156, March 2010.

[117] N. E. Thomas, P. A. R. Ade, F. E. Angilè, S. J. Benton, E. L. Chapin, M. J. Devlin, L. M. Fissel, N. N. Gandilo, J. O. Gundersen, P. C. Hargrave, D. H. Hughes, J. Klein, A. L. Korotkov, T. G. Matthews, L. Moncelsi, T. Mroczkowski, C. B. Netterfield, G. Novak, L. Olmi, E. Pascale, G. Savini, D. Scott, J. A. Shariff, J. D. Soler, M. D. P. Truch, C. E. Tucker, G. S. Tucker, D. Ward-Thompson, and D. V. Wiebe. BLAST-pol: Balloon-borne Large Aperture Submillimeter Telescope for Polarimetery. *Bulletin of the American Astronomical Society*, 41:316.04–+, May 2010.

[118] A. Trangsrud. Single device optical cryostat analysis logbook. http://spiderwiki.princeton.edu/cgi-bin/moin.cgi/AnalysisLogBook/SingleDeviceOpticalCryostat/.

[119] M. Tucci, E. Martínez-González, P. Vielva, and J. Delabrouille. Limits on the detectability of the CMB B-mode polarization imposed by foregrounds. *Monthly Notices of the Royal Astronomical Society*, 360:935–949, July 2005.

[120] C. E. Tucker and P. A. R. Ade. Thermal filtering for large aperture cryogenic detector arrays. *Society of Photo-Optical Instrumentation Engineers (SPIE) Conference Series*, 6275, July 2006.

[121] UBC MCE group. Multi-channel electronics (mce). http://www.phas.ubc.ca/%7Emce/mcedocs/index.html.

[122] S. Weinberg. *Cosmology.* Oxford University Press, Oxford, 2008.

[123] D. P. Woody and P. L. Richards. Spectrum of the cosmic background radiation. *Physical Review Letters*, 42(14):925–929, Apr 1979.

[124] K. W. Yoon, P. A. R. Ade, D. Barkats, J. O. Battle, E. M. Bierman, J. J. Bock, J. A. Brevik, H. C. Chiang, A. Crites, C. D. Dowell, L. Duband, G. S. Griffin, E. F. Hivon, W. L. Holzapfel, V. V. Hristov, B. G. Keating, J. M. Kovac, C.-L. Kuo, A. E. Lange, E. M. Leitch, P. V. Mason, H. T. Nguyen, N. Ponthieu, Y. D. Takahashi, T. Renbarger, L. C. Weintraub, and D. Woolsey. The Robinson Gravitational Wave Background Telescope (BICEP): a bolometric large angular scale CMB polarimeter. *Society of Photo-Optical Instrumentation Engineers (SPIE) Conference Series*, 6275, July 2006.

[125] M. Zaldarriaga and Uroš Seljak. Gravitational lensing effect on cosmic microwave background polarization. *Physical Review D*, 58(2):023003, June 1998.